Dissertation zur Erlangung des Doktorgrades

der Fakultät für Chemie und Pharmazie

der Ludwig-Maximilians-Universität München

Incidents and Mechanisms of Ferroptosis

Shan Xin

aus

Xiangyang, Hubei, China

2020

Erklärung

Diese Dissertation wurde im Sinne von § 7 der Promotionsordnung vom 28. November 2011 von Prof. Dr. Klaus Förstemann betreut.

Eidesstattliche Versicherung

Diese Dissertation wurde eigenständig und ohne unerlaubte Hilfe erarbeitet.

München, am 21.07.2020

Shan Xin

Dissertation eingereicht am 03.08.2020

1. Gutachter:	Prof. Dr. Klaus Förstemann
2. Gutachter:	PD. Dr. Dietmar Martin

Mündliche Prüfung am 15.09.2020

Abstract

Cell death can be activated either from the biologically uncontrolled process necrosis or via regulated cell death (RCD) including apoptosis, necroptosis, pyroptosis, autophagy and ferroptosis among others. Ferroptosis is an iron-dependent form of cell death characterized by the accumulation of lipid peroxides to lethal level. To date, the mechanisms and signaling pathways of this newly characterized form of cell death remains still relatively unknown, whether and how ferroptosis is involved in pathological scenarios needs to be clarified. The Schick lab recently performed a study to identify genes involved in ferroptosis using an unbiased CRISPR activation screen (Kraft et al., 2019). This effort led to the discovery of a novel four-pass membrane protein, MS4A15, which protects against ferroptosis strongly and specifically. In this thesis, a systematic framework has been designed to discover and characterize the molecular mechanisms of MS4A15 in protecting cells from ferroptosis and to identify biomarkers of ferroptosis for human degenerative diseases.

Membrane-spanning 4-domains subfamily A member 15 (MS4A15) is localized to the ER and it was immunoprecipitated with calcium related proteins. In *Ms4a15*-overexpressing mouse immortalized fibroblasts (MF *Ms4a15* OE), IP_3R1 expression level was dramatically downregulated, suggesting that calcium homeostasis might be disrupted. In line with these results, the *MS4A15* Go-Term analysis and GSEA analysis showed a strong correlation between *MS4A15* and calcium signaling. Further experiments confirmed that MS4A15 functions independently in the ER to mediate ferroptosis resistance via reducing intracellular calcium content, downregulating IP_3R and impairing store operated calcium uptake. By contrast, MS4A15 induced ER calcium depletion does not cause ER stress. Taken together, these evidences provide a crucial link between ferroptosis and calcium flux.

Calcium is a potent signaling molecule ascribed to diverse cellular processes. MF parental control cells with persistent calcium depletion induced by thapsigargin generated less lipid ROS and obtained ferroptosis resistance. Interestingly, overexpression of SERCA, which transports calcium from the cytosol into the ER store, leads to sensitization of *Ms4a15* OE cells, emphasizing the importance of intracellular calcium in mediating ferroptosis resistance. Polyunsaturated fatty acids containing glycerophospholipids (PUFA-GPs) are essential elements as the substrates for lipid peroxidation, which have different unsaturation degrees and chain lengths. Lipidomics and metabolomics analysis revealed that, compared with the control cells, the *Ms4a15* OE show a significant decrease of molecular weight and desaturation of PUFA-GPs, as well as an accumulation of saturated fatty acids, monounsaturated fatty acids containing glycerophospholipids (MUFA-GPs) and plasmalogens. Notably, the MUFAs and plasmalogens increased in *Ms4a15* OE cells were strongly depleted after RSL3 treatment, indicating the protection role against lipid

peroxidation. These results leading us to conclude that sustained depletion of intracellular calcium suppressed ferroptosis through promoting fundamental lipid remodeling. Further analysis indicates that a branch of calcium genes from the KEGG pathway define a signature for driving ferroptosis sensitivity in cancer cells, which may solve the link between calcium homeostasis and ferroptosis sensitivity and provide a new strategy for cancer therapeutics.

Ferroptosis has been proposed to be involved in a large number of diseases; however the cumulative implication of ferroptosis in disease is based on cell culture experiments and in vivo evidence with mice. Due to a lack of discriminating ferroptosis cell death markers, direct demonstration of ferroptosis in human diseases is missing. To isolate potential ferroptosis biomarkers, cell surface biotinylation and protein mass spectrometry approaches were performed from cells undergoing ferroptosis. As a result, a list of secreted/membrane-bound proteins in early stage of ferroptosis was identified. The top five identified membrane proteins were further investigated and showed a significant increase in abundance upon ferroptosis stimulation using immunofluorescence detection of HT1080 cells. In addition, these biomarker candidates were found to be specific to ferroptosis induction with an elevated expression, as no change under other forms of cell deaths was observed. Furthermore, initial evaluation of corresponding antibodies on control human paraffin embedded tissue revealed FABP5 as a promising ferroptosis-specific biomarker for brain tumors.

In summary, these findings provide a novel mechanism of MS4A15 that persistent disruption of calcium homeostasis results in stimulation of fundamental lipid remodeling, which protect cells against ferroptotic cell death. Therefore, induction of ferroptosis by mediating calcium homeostasis may be helpful for overcoming cancer therapy resistance and improving prognosis. In addition, this work provides a new insight for early diagnosis of human degenerative diseases through identified potential ferroptosis-specific protein biomarkers.

Table of Contents

List of Figures

List of Tables

ABBREVIATIONS

αToc	α-tocopherol
AA	arachidonic acid
ACAT1	acetyl-CoA acetyltransferase 1
ADRB2	Adrenoceptor Beta 2
AIF	apoptosis-inducing factor
ALOX	arachidonate lipoxygenases
AMP	adenosine monophosphate
ART	Artesunate
ATG 5/7	Autophagy Related 5/7
ATP	adenosine triphosphate
BDKRB1/2	bradykinin B receptors
BSA	bovine serum albumin
BSO	buthionine sulfoxamine
CACNA	calcium voltage-gated channel subunits
CALML5	Calmodulin-like protein 5
CARS	cysteinyl tRNA synthetase
Cas9	CRISPR-associated protein-9
CCLE	Cancer Cell Line Encyclopedia
ccRcc	clear cell renal cell carcinoma
CD38	cyclic ADP-Ribose hydrolase
CHOP	TC/EBP homologous protein
CLSP	calmodulin-like skin protein
CoQ10	coenzyme Q10
COX	cyclooxygenase
CRAC	calcium release-activated channels
CRISPR	Clustered Regularly Interspaced Short Palindromic Repeats
CTRP	Cancer Therapeutics Response Portal
CTSV	Cathepsin V

DAG	diacylglycerol
DFO	deferoxamine
DHA	docosahexaenoic acid
DMEM	Dulbecco’s Modified Eagle Medium
DMSO	dimethyl sulfoxide
DMT1	divalent metal transporter 1
DPP4	dipeptidyl-peptidase-4
EDTA	ethylenediaminetetraacetic acid
EGFR	epidermal growth factor receptor
EPA	eicosapentaenoic acid
ERAD	endoplasmic reticulum-associated degradation
ERK	extracellular signal–regulated kinase
ERN1	endoplasmic reticulum to nucleus signaling 1
FABP5	Fatty acid-binding protein 5
FACS	fluorescence-activated cell sorting
FITC	fluorescein isothiocyanate
FPN	ferroportin
FTH1	ferritin heavy chain 1
FTL	ferritin light chain
Gln	glutamine
Glu	glutamate
GPCRs	G protein-coupled receptors
GPX4	glutathione peroxidase 4
GSEA	Gene Set Enrichment Analysis
GSH/GSSG	reduced and oxidized glutathione
HCC	hepatocellular carcinoma
HMG-CoA	3-hydroxy-3-methylglutaryl-Coenzyme A
HO-1	heme oxygenase-1
HSPB1	heat shock protein beta-1

IKE	imidazole ketone erastin
IP	immunoprecipitation
IP3	inositol 1,4,5-trisphosphate
IP3R	IP3 receptor
IRE1	inositol-requiring enzyme 1
IREB2	iron response element binding protein 2
JNK	c-Jun NH2-terminal kinase
LGALS 7	Galectin 7
L-OH	lipid alcohol
L-OOH	lipid hydroperoxide
LPA	Lysophosphatidic acid
LPCAT3	lysophosphatidylcholine acyltransferase 3
MAPK	mitogen-activated protein kinase
MF	mouse immortalized fibroblast
MS4A12	membrane-spanning 4-domains subfamily A member 12
MS4A15	membrane-spanning 4-domains subfamily A member 15
MUFA	monounsaturated fatty acid
NADH	nicotinamide adenine dinucleotide
NADPH	nicotinamide adenine dinucleotide phosphate
NFS1	cysteine desulfurase
NSCLC	non-small-cell lung cancer
oxytosis	oxidative glutamate toxicity
P2RX1	P2X G-protein-coupled receptor
PBS	phosphate buffered saline
PBS-T	PBS-Tween 20
PC	phosphatidylcholine
PCA	Principal component analysis
PC-OOH	phosphatidylcholine hydroperoxide
PDE1B	cGMP phosphohydrolyase

PE	phosphatidylethanolamine
PI	phosphatidylinositol
PKC	protein kinase C
PL	phospholipid
PLA	phospholipase A
PLC	phospholipase C
PLD	Phospholipase D
PPAR	peroxisome proliferator-activated receptor
PTAFR	platelet activating factor receptor
PTGS1	prostaglandin-endoperoxide synthase
PUFA	polyunsaturated fatty acid
RMS	rhabdomyosarcoma cell
RNAseq	RNA sequencing
ROS	reactive oxygen species
RSL3	ras-selective lethal small molecule 3
RTK	receptor tyrosine kinase
RT-PCR	Real-time PCR
RYR1	ryanodine receptor 1
S100A14	S100 Calcium Binding Protein A14
SAS	sulfasalazine
SDS	Sodium dodecyl sulfate
SDS-PAGE	SDS polyacrylamide gel electrophoresis
Sec	selenocysteine
SERCA	sarco/endoplasmic reticulum Ca^{2+}-ATPase
SFA	saturated fatty acids
sgRNA	single guide RNA
SOCE	store-operated calcium entry
SPN	sialophorin
ssGSEA	single sample Gene Set Enrichment Analysis

TCA	tricarboxylic acid
TE	Tris EDTA
TEMED	Tetramethylethylenediamine
TF	transferrin
TFRC	transferrin receptor
TNBC	triple-negative breast cancer
TNF	tumour necrosis factor
TUNEL	terminal deoxynucleotidyl transferase dUTP nick end labeling
UPR	unfolded protein response
VDAC	voltage-dependent anion channel
WASP	Wiskott-Aldrich syndrome protein
WB	Western Blot
XBP1	X-box-binding protein 1
ZIP 8/14	Zinc-Iron regulatory protein family 8/14

1. Introduction

Cell death is an inevitable process for multicellular organisms to maintain health and vitality. Dysregulation of cell death has been implicated in various physiological and pathological processes. Traditionally, cell death has been divided into programmed cell death, e.g. apoptosis and accidental cell death, e.g. necrosis modalities to explain diverse biological processes. With the deepening of research on cell death during the last decades, more distinct cell death phenotypes have been discovered, including a novel mode of non-apoptotic cell death, termed ferroptosis. Due to the emerging evidences in pathophysiological processes of many diseases, such as tumors, blood diseases, and kidney injury, this ferroptotic cell death has become an exciting topic recently. More importantly, current findings indicate that tumors cells, which escape from other types of cell death are likely to undergo ferroptosis, suggesting a new strategy for cancer therapy.

Ferroptosis is an iron-dependent form of non-apoptotic cell death which was first proposed by the lab of Dr. Brent R Stockwell in 2012 (Dixon et al., 2012), it occurs through an accumulation in cellular phospholipid peroxidation to lethal level. This form of cell death is in the context of a compromised phospholipid peroxide repair system and is genetically, biochemically, and morphologically distinct from diverse cell deaths, such as necrosis, apoptosis, and autophagy (Table 1).

How, when and where does ferroptosis occur? What is the relationship between ferroptosis and other types of regulated cell death? What are the mechanisms and downstream regulation pathways of ferroptosis? How can we promote ferroptosis to treat cancer, and resists ferroptosis to treat human diseases by regulating ferroptosis? These are the main questions that have been attracting me. In the dissertation project, the main goal is to study the molecular mechanisms ferroptosis and to discover the potential ferroptosis-specific biomarkers of human degenerative diseases. The following sections in chapter1 describe the historical perspectives of our understanding of ferroptosis.

In the subsequent chapters, the molecular mechanisms of the newly discovered membrane-spanning 4-domains subfamily A member 15 (MS4A15) in controlling ferroptosis and the relevance of ferroptosis to human diseases were investigated using technologies from systems biology and molecular biology.

Table 1 The main morphological, biochemical, regulatory pathways and core regulators of ferroptosis, apoptosis, necroptosis, and autophagy, summarized from (Galluzzi et al., 2012; Kroemer et al., 2005; Li et al., 2020; Xie et al., 2016).

Type	Morphological features	Biochemical features	Regulatory pathways	Core regulators
Ferroptosis	Cell membrane: rounding-up of the cell Cytoplasm: small mitochondria with condensed mitochondrial membrane densities, reduction or vanishing of mitochondria crista, outer mitochondrial membrane rupture Nucleus: lack of chromatin condensation	Iron and lipid ROS accumulation MAPK activation Inhibition of system X_c^- GSH depletion and increased NAPDH oxidation	X_c^-/GPX4, MVA, sulfur transfer pathway; P62-Keap1-NRF2 pathway; P53/SLC7A11, ATG5-ATG7-NCOA4 pathway; P53-SAT1-ALOX15 pathway; HSPB1-TRF1, FSP1-COQ10-NAD(P)H	**Positive** • VDAC2/3 • Ras • NOX • TFR1 • p53 • ACSL4 • CARS **Negative** • GPX4 • SLC7A11 • HSPB1 • NRF2 • FSP1
Apoptosis	Cell membrane: plasma membrane blebbing; rounding-up of the cell Cytoplasm: pseudopods retraction Nucleus: reduction of volume; fragmentation; chromatin condensation	Activation of caspases DNA fragmentation Δψm dissipation PS exposure	mitochondrion and endoplasmic reticulum pathway; Caspase, P53, Bcl-2 mediated signaling pathway	**Positive** • p53 • Bax • Bak • Caspase **Negative** • Bcl-2 • Bcl-XL
Necroptosis	Cell membrane: rupture of plasma membrane Cytoplasm: cytoplasmic swelling (oncosis); swelling of cytoplasmic organelles Nucleus: chromatin condensation	Drop in ATP levels Release of DAMPs (e.g., HMGB1) PARP1 hyperactivation	TNF-R1 and RIP1/RIP3-MLKL signaling pathways; PKC-MAPK-AP-1 related signaling pathway; ROS-related regulation pathway	**Positive** • RIP1 • RIP3 • MLKL
Autophagy	Cytoplasm: formation of double-membraned autophagic vacuoles Nucleus: lack of chromatin condensation	Increased lysosomal activity Substrate (e.g., p62) degradation	mTOR, Beclin-1, P53 signaling pathway	**Positive** • ATG5 • ATG7 • Beclin 1 • DRAM3 • TFEB

1.1 Mechanisms of Ferroptosis

The initiation and execution of ferroptosis is mainly regulated by metabolism changes in iron homeostasis and lipid peroxidation, the mechanisms and regulatory pathways of ferroptosis can be roughly categorized into four groups so far.

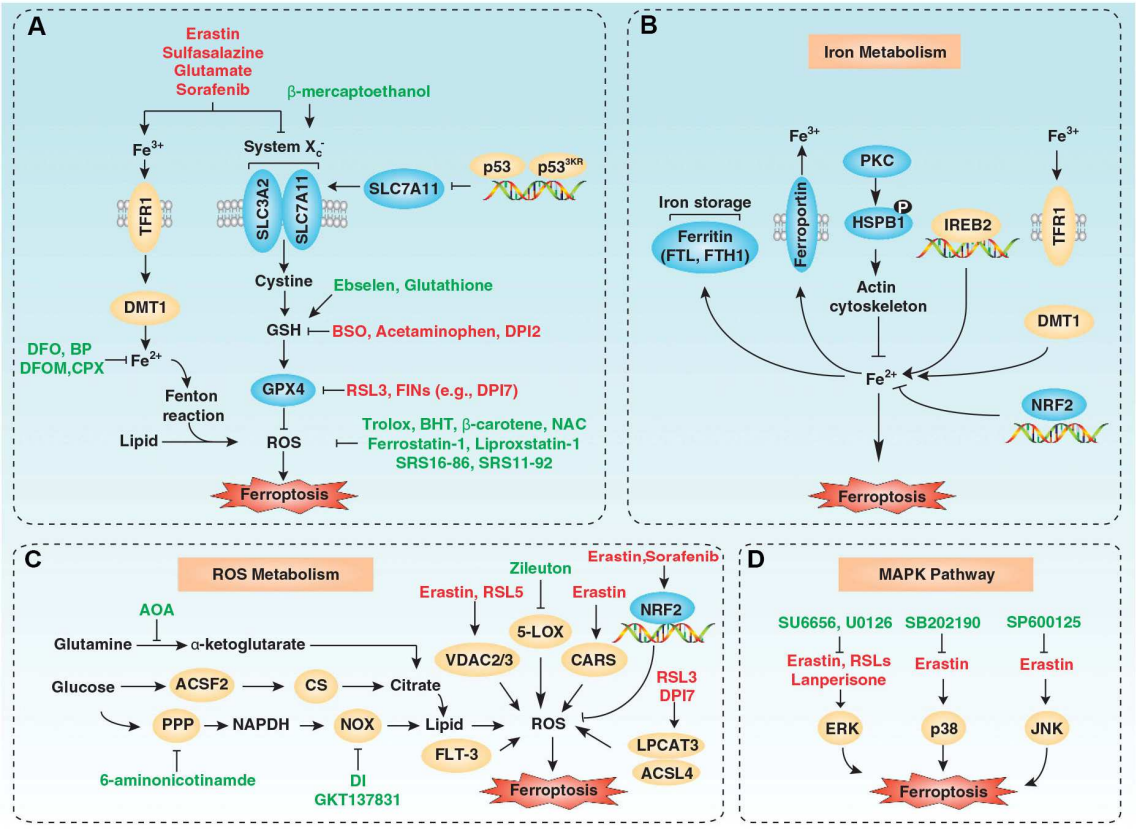

Figure 1.1 Molecular mechanisms and signaling pathways of ferroptosis. (A) Core regulators in GSH/GPX4 pathway. (B–D) Roles of iron metabolism (B), lipid peroxidation metabolism (C), and the MAPK pathway (D) in ferroptosis (Xie et al., 2016).

1.1.1 GPX4–GSH–cysteine Axis

The GPX4–GSH–cysteine axis of ferroptosis includes GPX4 activity, system X_c^-, transsulfuration pathway, Mevalonate pathway, glutamine pathway, and p53 regulatory axis, etc..

GPX4 Pathway. Glutathione peroxidase 4 (GPX4) is the key enzyme to protect from ferroptosis, which oxidizes glutathione (GSH) to convert lipid hydroperoxides (L-OOH) to lipid alcohols (L-OH) within biological membranes. Deprivation of GPX4 activity causes elevated intracellular lipid ROS to lethal level. RSL3 and ML162 are small molecules that trigger

ferroptosis by directly targeting GPX4 (Shimada et al., 2016; Yang et al., 2014a); therefore, cells treated with RSL3 or ML162 display increased lipid ROS and accumulated iron in the absence of GSH depletion. The lipophilic antioxidants such as vitamin E protect against ferroptosis through suppressing the formation and propagation of oxidized lipids on GPX4 deprivation.

System X_c^- Pathway. System X_c^- is a crucial antioxidant system, which is widely distributed in phospholipid bilayers. It is an amino acid anti-transporter composed of two subunits, SLC7A11 and SLC3A2. Through system X_c^-, cystine and glutamate can be exchanged in and out of the cell at a ratio of 1:1 (Dixon et al., 2012). Cysteine, the reduced form of cystine, is a precursor for the synthesis of GSH. The reduced GSH can be used as an enzyme co-substrate to reduce lipid peroxidation under the action of GPX4. Hence, inhibition of system X_c^- results in loss of cellular antioxidant capacity through inactivating GPX4 activity indirectly. A metabolite profiling assay revealed that erastin initiates ferroptosis by blocking system X_c^- and depletes GSH, as GSH was the most decreased cellular metabolite (Yang et al., 2014a).

GPX4 pathway and system X_c^- pathway explain how RSL3 and erastin share a common ferroptosis execution mechanism but have different triggering mechanisms (Figure 1.1 Molecular mechanisms and signaling pathways of ferroptosis.Figure 1.1A).

Mevalonate Pathway. GPX4 is a selenoprotein that contains selenocysteine (Sec) as one of the essential amino acids in the active site (Yang et al., 2014a). The selenocysteine tRNA [tRNA (Sec)] is the key component to insert selenocysteine into GPX4 (Kryukov et al., 2003). Therefore, the mevalonate (MVA) pathway can affect the occurrence of ferroptosis through regulating the maturation of tRNA (Sec) and the synthesis of GPX4.

The mevalonate pathway leads to the production of CoQ10 which is an endogenous inhibitor of ferroptosis by serving an antioxidant function in membranes (Shimada et al., 2016). The ferroptosis-inducing compound FIN56 depletes CoQ10 by modulating squalene synthase activity (SQS), which in part drives accumulation of lethal lipid peroxidation (Shimada et al., 2016). Statins, inducers of ferroptosis, are the rate-limiting enzymes of the mevalonate pathway, have been shown to interfere with the maturation of tRNA (Sec) and promote the depletion of CoQ10 (Warner et al., 2000).

The Transsulfuration Pathway. The Transsulfuration Pathway (TSS pathway) is an alternative source of cysteine, in which methionine is used as a sulfur donor and is converted into cysteine through homocysteine and cystathionine (McBean, 2012). When cell uptake mechanisms are normal, the importance of TSS pathway is cell-type dependent, however, when the uptake mechanism is inhibited, the TSS pathway is important for cell survival. Cysteinyl tRNA synthetase (CARS) were identified from a genome-wide RNAi screen as

robust genetic suppressors of erastin-induced ferroptosis (Hayano et al., 2016). Further studies demonstrated that some genes and metabolites in the TSS pathway were upregulated in CARS-depleted cells treated with erastin, suggesting that modulate the TSS pathway can regulate ferroptosis sensitivity (Hayano et al., 2016).

Mitochondrial VDACs. The mitochondrial voltage-dependent anion channels (VDACs) are transmembrane channels that transport ions and metabolites, blocking the VDACs leads to mitochondrial dysfunction and cell death (Skonieczna et al., 2017). Previous study found that VDACs is one of the direct molecular targets of erastin (Yagoda et al., 2007), providing a vital regulatory role in ferroptosis. Erastin targets VDACs causing the dysfunction of mitochondrial and accumulation of releases oxides, eventually leading to ferroptosis.

Glutamine Pathway. Glutaminolysis plays a key role in the ferroptosis process. Upon deprivation of amino acids, glutamine (Gln) and transferrin (TF) are two essential extracellular compounds to induce ferroptosis via the glutaminolysis pathway (Gao et al., 2015). The degradation of Gln via glutaminolysis can provide fuel for the tricarboxylic acid (TCA) cycle as well as build blocks for essential biosynthetic processes, such as lipid biosynthesis. Therefore, deprivation of Gln or inhibition of glutaminolysis can trigger ferroptosis, suggesting additional strategies for suppressing the accumulation of ROS, lipid peroxidation, and ferroptosis.

P53-Mediated ferroptosis. The P53 gene is a significant tumor suppressor gene, which may regulate ferroptosis in 2 different pathways. Studies have found that P53 modulates ferroptosis by downregulating the expression of SLC7A11, which results in the inhibiton of system X_c^- and subsequent inactivation of GPX4 activity and reduction of antioxidant capacity. In addition, the P53-SAT1-ALOX15 pathway has also been reported to regulate ferroptosis (Ou et al., 2016). P53-mediated activation of SAT1, a transcription target of P53, contributes to lipid peroxidation and sensitizes cells to undergo ferroptosis under ROS stress, which is closely related to the expression level of arachidonate lipoxygenase 15 (ALOX-15).

However, other studies proposed that P53 inhibits ferroptosis by increasing the activity of system X_c^- and reducing the sensitivity of some cells to ferroptosis. The process of reducing ferroptosis sensitivity requires the involvement of a P53 transcription target CDKN1A (encoding P21) through regulating GSH metabolism, this P53-P21 axis has been found to negatively regulate the occurrence of ferroptosis in cancer cells (Tarangelo et al., 2018). Furthermore, the expression of P53 limits erastin-induced ferroptosis by blocking dipeptidyl-peptidase-4 (DPP4) activity, which prevents the generation of DPP4-dependent lipid peroxidation. This molecular link between P53 and DPP4 in the control of lipid metabolism is involved in medicine therapy of colorectal cancer cells (Xie et al., 2017).

1.1.2 Iron metabolism

Ferroptosis is a new type of cell death depends on intracellular iron, meaning iron is essential for the execution of ferroptosis. Cells execute ferroptosis under the treatment of erastin, RSL3, or other inducers normally show higher levels of irons (Yang and Stockwell, 2008) associated with an increased level of lipid ROS (Yang et al., 2014a), and these executors can be pharmacologically inhibited by iron chelators and lipophilic antioxidants (Dixon et al., 2012; Yagoda et al., 2007).

Free Fe^{2+} can be oxidized by ceruloplasmin to Fe^{3+}, which binds to transferrin (TF) on the cell membrane and enters into cells by TF receptor 1 (TFR1). Fe^{3+} is then reduced to Fe^{2+} by iron oxide reductase, the six-transmembrane epithelial antigen of the prostate 3 (STEAP3), and Fe^{2+} is then stored into the unstable iron pool and ferritin in the cytoplasm, which is mediated by divalent metal transporter 1 (DMT1) or Zinc-Iron regulatory protein family 8/14 (ZIP8/14) (Frazer and Anderson, 2014). Free intracellular Fe^{2+} can produce hydroxyl radicals (·OH) or peroxide radicals, which further oxidize lipids, under the action of the Fenton reaction (Figure 1.2). Fenton reaction converts H_2O_2 into ·OH thus limiting the uptake of iron suppresses ferroptosis. Excess Fe^{2+} is oxidized to Fe^{3+} by ferroportin (FPN) (Bogdan et al., 2016). This recycling of internal iron strictly controls iron homeostasis in cells.

In ferroptosis, iron metabolism-related genes are the critical mediators of the lipid ROS formation, such as TF, TFR1, FPN, DMT1, ferritin heavy chain 1 (FTH1), and ferritin light chain (FTL) (Figure 1.1B). Therefore, downregulation of transferrin receptor–mediated import of transferrin-iron via silencing transferrin receptor (TFRC), the gene encoding TFR 1, can inhibit erastin-induced ferroptosis (Gao et al., 2015), moreover the iron-containing heme oxygenase-1 (HO-1) can be a source of iron to accelerate ferroptosis (Kwon et al., 2015).

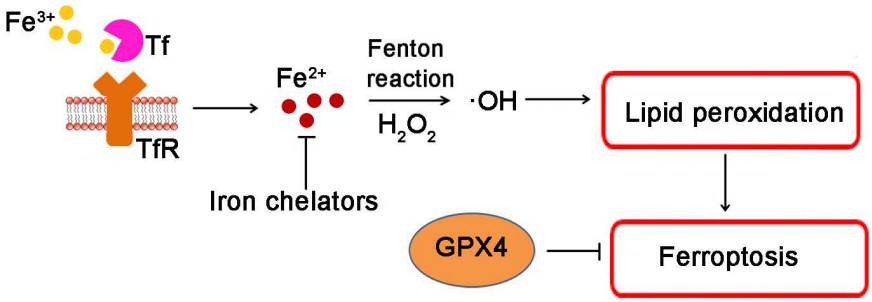

Figure 1.2 Role of iron in ferroptosis. Arrows indicate promotion; blunt-ended lines indicate inhibition. Tf, transferrin; TfR, transferrin receptor; H_2O_2, hydrogen peroxide; •OH, hydroxyl radicals; GPX4, glutathione peroxidase 4.

Based on the previous research, heat shock protein beta-1 (HSPB1) was found as a novel negative regulator of ferroptotic cell death which reduces intracellular iron concentrations and ROS production by inhibiting TRF1 expression (Sun et al., 2015b). Furthermore, iron response element binding protein 2 (IREB2) is the main transcription factor of iron metabolism and the majority of iron is stored within ferritin, inhibiting IREB2 expression can significantly increase the expression of the two factors of ferritin, FTL and FTH1, to store Fe^{2+} and prevent erastin-induced ferroptosis. In addition, miRNAs were reported to have an impact on ferroptosis through regulating iron export, storage, utilization, and uptake. For example, MiR-20a and miR-485-3p can reduce iron output by targeting FPN genes (Babu and Muckenthaler, 2016; Sangokoya et al., 2013); MiR-210 and miR-152 inhibit the expression level of TFR, thereby reducing intracellular iron concentration (Kindrat et al., 2016; Yoshioka et al., 2012).

Disruption of iron homeostasis can affect the normal physiological processes in the body. Cells exposed to high levels of extracellular iron may be sufficient to induce ferroptosis. Interestingly, this process alters the sensitivity of different types of cancer cells to ferroptosis, for example high-grade serous ovarian cancer (HGSOC) cells which are highly susceptible to ferroptosis due to increased TFR1 expression level and decreased iron efflux pump FPN level (Basuli et al., 2017). Therefore, initiation of ferroptosis via increasing the concentration of intracellular iron could be a strategy for cancer therapy.

1.1.3 Lipid metabolism

Iron-dependent lipid peroxidation is one of the hallmarks of ferroptosis (Figure 1.1C), apart from defective lipid peroxide repair and redox-active iron. Lipid peroxidation is fundamental to all pathways.

The membranes of mammalian cells are enriched with glycerophospholipids [hereafter refer to GPs] acylated with at least one polyunsaturated fatty acid (PUFA) chain. PUFAs, which have different chain lengths (C18, C22 or higher) and various degrees of unsaturation (e.g., C18:3, C20:4, C22:5), are essential elements as the substrates of lipid metabolism signal for ferroptosis.

The bis-allylic hydrogen atoms present within PUFAs are more susceptible to oxidative conditions compared with saturated fatty acids (SFA) and monounsaturated fatty acids (MUFA) (Gaschler and Stockwell, 2017). However, free PUFAs are unlikely to promote ferroptosis, to participate in ferroptosis processes, they must be incorporated into GLs with

different head groups [e.g., phosphatidylinositol (PI), phosphatidylcholine (PC), or phosphatidylethanolamine (PE)] (Magtanong et al., 2016).

PEs, which contain arachidonic acid (AA, C20:4) or docosahexaenoic acid (DHA, C22:6) fatty acyl chains, were discovered as the key phospholipids that triggers ferroptosis execution (Kagan et al., 2017; Wenzel et al., 2017). Acyl-CoA synthetase long-chain family member 4 (ACSL4) and lysophosphatidylcholine acyltransferase 3 (LPCAT3), which participate in the biosynthesis and remodeling of PE, activate PUFAs and affect the incorporation of activated PUFAs into membrane GLs. Therefore, suppressing the activity of ACSL4 and LPCAT3 could inhibit ferroptosis due to lack of esterified PUFAs and depletion of the substrates for lipid peroxidation (Dixon et al., 2015; Do Van et al., 2016; Doll et al., 2017). Alternatively, PUFA-containing PE further oxidizes the cells under the catalysis of lipoxygenase (LOX) to promote ferroptosis (Kagan et al., 2017). PUFA-PL oxidation could also lead to membrane thinning and aberrant membrane curvature, forming a structured lipid pore on membrane and accelerating death rate (Agmon et al., 2018).

The models in Figure 1.3 briefly displayed the important role of lipid peroxidation in ferroptosis (Agmon et al., 2018). PUFAs are acetylated by acyl-CoA synthetase and are incorporated into phospholipids with SFAs. Initiation of ferroptosis triggered by PUFA oxidation can be prevented by GSH/GPX4 pathway through reducing the oxidized PUFAs to lipid alcohols. When the activity of GSH/GPX4 is blocked, oxidized PUFAs can cause the release of reactive oxygen species (ROS) and membrane destruction, which can be protected by iron chelators and lipophilic antioxidants.

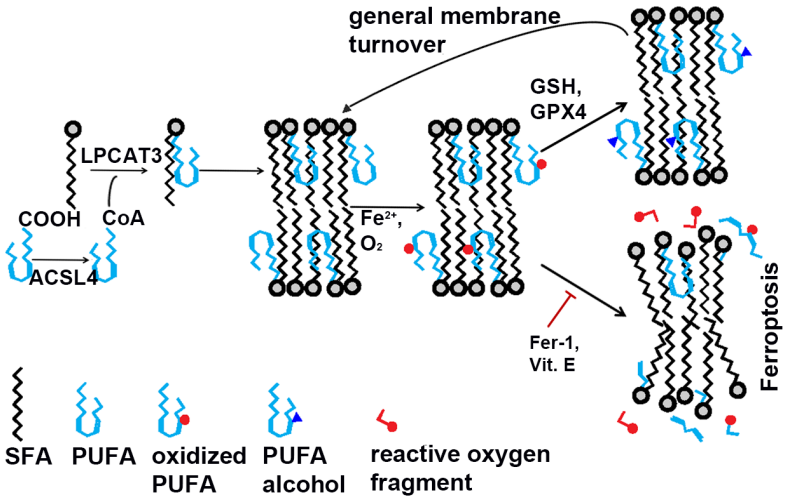

Figure 1.3 Lipids activities during ferroptosis. PUFAs are depicted in light blue, oxidized PUFAs are labeled with red circles, PUFA alcohols are labeled with blue triangles, reactive oxygen species are depicted with red fragment.

Based on previous research, ferroptosis can be prohibited by free radical scavenging (i.e. α-tocopherol (αTOC), ferrostatin), feeding cells with bis-allylic deuterated PUFAs that are less susceptible to oxidation (Magtanong et al., 2019; Skouta et al., 2014; Yang et al., 2016) or adding compounds to compete with the oxidation substrates for the binding site (i.e. plasmalogens, corking). How lipid composition alteration leads to the final implementation of ferroptosis requires more exploration.

1.1.4 MAPK pathway

In addition to the two hallmarks of ferroptosis, iron metabolism and lipid peroxidation, activation of the mitogen-activated protein kinase (MAPK) pathway contributes to ferroptotic cancer cell death as well (Figure 1.1D).

RAS (H-RAS, K-RAS4A and 4B, and N-RAS) activation of cancer cells could contribute to ferroptosis sensitivity by increasing the expression of TFR and ferritin, thereby promoting intracellular iron abundance and lipid ROS accumulation (Yang and Stockwell, 2008). Silencing of oncogenic KRAS expression in KRAS-mutant Calu-1 cells significantly reduces the lethality of erastin (Yagoda et al., 2007). However, ectopic expression of oncogenic RAS increases resistance to erastin-induced ferroptosis in rhabdomyosarcoma cells (RMS), which means the Ras-mediated ferroptosis sensitivity is altered in different cancer types (Dixon et al., 2015). In fact, a broad panel of cancer cell lines has been studied to discover the relationship between certain gene expression levels and cell sensitivity to ferroptosis, however, no correlation was observed between RAS mutation status and the potency of erastin (Yang et al., 2014a).

The above evidences of cell type-specific and mutation-specific sensitivity to ferroptosis extends to the role of MAPK pathway or the RAS-RAF-MEK-ERK pathway. The mammalian family of MAPKs mainly includes extracellular signal–regulated kinase (ERK), p38, and c-Jun NH2-terminal kinase (JNK). The mechanism of action of erastin is involved the RAS/RAF/MEK-dependent oxidative cell death through targeting the VDACs, which has been proved to be an important target for the treatment of hepatocellular carcinoma (HCC). Oncogenic mutations in KRAS, BRAF, and PIK3CA have been confirmed to sensitize cells to cystine deprivation–induced death. Blocking the RAS/RAF/MEK/ERK pathway inhibits erastin-induced ferroptosis in RAS-mutated cancer cells (Yagoda et al., 2007).

Epidermal growth factor receptor (EGFR) is a receptor tyrosine kinase (RTK) that transduces signals through the MAPK and other pathways. When human mammary epithelial (HME) cells express an activated EGFR mutant, deprivation of cystine led to increased cell death

which was associated with synchronous loss of plasma membrane integrity. In addition, elevated MAPK signaling was uncovered to be related to ferroptosis vulnerability, on the contrary, blockade of EGFR or MAPK signaling protected cells against erastin. Xenografts derived from EGFR mutant or activating EGFR mutation non-small-cell lung cancer (NSCLC) prevented tumor growth in mice when treated with a cystine-depleting enzyme (Poursaitidis et al., 2017), suggesting a therapeutic benefit of cystine depletion in some tumors through promoting ferroptosis. In fact, NSCLC cells which have the highest relative MAPK activity were most sensitive to ferroptosis induced by cystine deprivation. This phenomenon is consistent with the observation that some cell lines were sensitized to ferroptosis through activation of the RAS/MAPK pathway (Poursaitidis et al., 2017).

In summary, these findings indicated that responses of cells to ferroptosis induction are associated with a differential MAPK module response in different cell types. More importantly, a potential sensitization approach of tumors to cystine deprivation induced ferroptosis could be exploited through manipulating EGFR/MAPK signaling.

1.1.5 Classification of ferroptosis inducers

Collectively, based on the mechanisms mentioned, compounds that are able to induce ferroptosis can be divided into four categories through distinct mechanisms (Li et al., 2020). The first category includes chemicals that reduce GSH levels by directly inhibiting system X_c^- which is part of an important antioxidant system in cells, such as erastin, sulfasalazine (SAS), sorafenib and buthionine sulfoxamine (BSO). The second category includes RSL3, ML162 and DPI7, which inhibit GPX4 activity without GSH depletion, thereby resulting in accumulation of lipid hydroperoxides. The third category includes chemicals such as FIN56 and statins, which can either deplete endogenous antioxidant coenzyme Q10 (CoQ10) via binding to the enzyme squalene synthase or decrease GPX4 protein abundance to cause lipid peroxidation (Shimada et al., 2016). The final category includes FINO2, an organic peroxide that can promote the oxidation of labile iron and inactivation of GPX4 (Gaschler et al., 2018).

1.2 Calcium and ferroptosis

Calcium is a ubiquitous second messenger functioning as an important regulator of cell growth, migration, and cell death. Although the dysregulation of Ca^{2+} homeostasis has been proposed to be involved in pathogenic mechanisms of various neurodegenerative diseases,

such as Alzheimer's, Parkinson's and Huntington's disease (Czeredys et al., 2013; Schöndorf et al., 2014; Small, 2009; Zündorf and Reiser, 2011), the study of Ca^{2+} signaling is still a novel field of research, especially its role in modulating ferroptosis.

In 1989, glutamate induced Ca^{2+}-dependent cell death was first reported in the N18-RE-105 neuroblastoma X retina cell line, which inhibits the import of cystine via the cystine/glutamate antiporter system X_c^-, resulting in depletion of the antioxidant GSH, burst of oxidative stress, and a massive Ca^{2+} influx (Henke et al., 2013; Murphy et al., 1989). This Ca^{2+}-dependent cytotoxicity has been named oxidative glutamate toxicity or oxytosis (Tan et al., 2001) and has been extensively studied in the hippocampal cell line HT22.

During glutamate induced oxytosis, a sharp increase in ROS generation has been captured when the GSH levels drop below 20%, however, this is just a necessary step in the oxytosis process but not the final step that causes cell death (Maher et al., 2018a). The similarity of oxytosis and ferroptosis has been long debated; especially GSH is also a crucial factor of ferroptosis (Figure 1.4). GPX4 is the key enzyme that protects cells from ferroptosis using GSH as an essential cofactor to convert lipid L-OOH to L-OH (Dixon et al., 2012; Yang et al., 2014b). Loss of GPX4 activity and deprivation of GSH both lead to the activation of 12/15-lipoxygenase (12/15-LOX, the protein product of the ALOX15 gene) (Li et al., 1997; Seiler et al., 2008). 12/15-LOX is an enzyme not only oxidizes PUFAs, but generates metabolites including 12- and 15- hydroxyeicosatetraenoic acid (HETE) which promote Ca^{2+} influx for the final phase of oxytosis (Lewerenz et al., 2013). 12/15-LOX also directly integrates into the membranes of various organelles further increasing lipid peroxidation and ROS production. Approximately 10–12 hours after the induction of oxidative glutamate toxicity, the pro-apoptotic Bcl-2 family member Bid translocates to the mitochondria causing the loss of their membrane integrity (Landshamer et al., 2008). Meanwhile, mitochondria apoptosis-inducing factor (AIF) translocate to the nucleus, where it rapidly induces caspase-independent cell death.

The major source of these ROS appears to be complex I of the mitochondrial electron transport chain, which is followed by an essential lethal influx of store-operated calcium (SOCE) that immediately executes cell death (Maher et al., 2018a; Tan et al., 1998). Of note, there is a mutual requirement for calcium and ROS for each to reach their maximal levels.

Although it has been argued that ferroptosis is distinct from oxytosis, especially the role of Ca^{2+} in ferroptosis has not been fully explored. These two cell death pathways show similarities since both can be inhibited by iron chelators (e.g. DFO) (Maher and Kontoghiorghes, 2015) and lipophilic antioxidants (e.g. ferrostatin-1) (Kang et al., 2014b). Additional evidence supports lethal calcium flux involvement in ferroptosis (Kang et al.,

2014a; Liu and Schubert, 2009; Maher et al., 2018b). Despite this, the role of calcium underlying ferroptosis remains to be fully characterized.

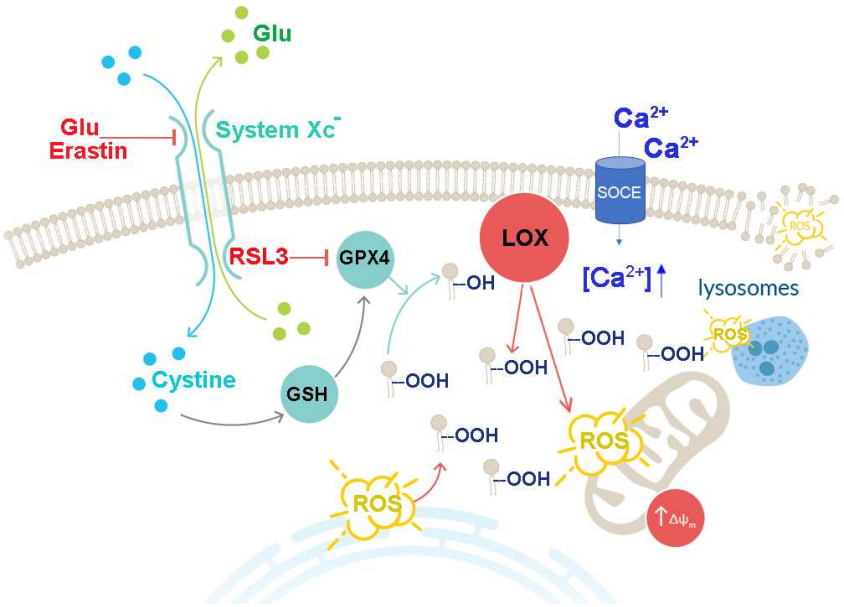

Figure 1.4 The common cell death pathway in oxytosis and ferroptosis (Lewerenz et al., 2018). Cystine uptake by system x_c^- is inhibited by Glu and Erastin which leads to the depletion of GSH and inhibition of GPX4 activity. RSL3 targets GPX4 directly to activate LOX, therefore, lipid hydroperoxides (lipid icons with OOH) accumulate at various membrane sites, including ER and mitochondria. Lysosomes also contribute to the overall ROS production.

1.3 MS4A15 and Ferroptosis resistance

Recently, our lab performed an unbiased Clustered Regularly Interspaced Short Palindromic Repeats activation (CRISPRa) screen to identify genes protecting against ferroptosis. Three established ferroptosis inducers were chosen to treat immortalized murine fibroblast (MF) cells: RSL3, imidazole ketone erastin (IKE) and genetic ablation of *Gpx4*. A single gene was obtained, *Gch1*, from all three conditions (Figure 1.5A). GCH1 promotes the production of its metabolic derivatives tetrahydrobiopterin/dihydrobiopterin (BH4/BH2) which are the endogenous antioxidants, to ultimately prevent peroxidation of certain PUFAs (Kraft et al., 2019). This GCH1-BH4-phospholipid axis exists as an independent parallel system to regulate ferroptosis resistance. This new mechanism completes the ferroptosis pathway and provides a new therapy strategy for cancer entities.

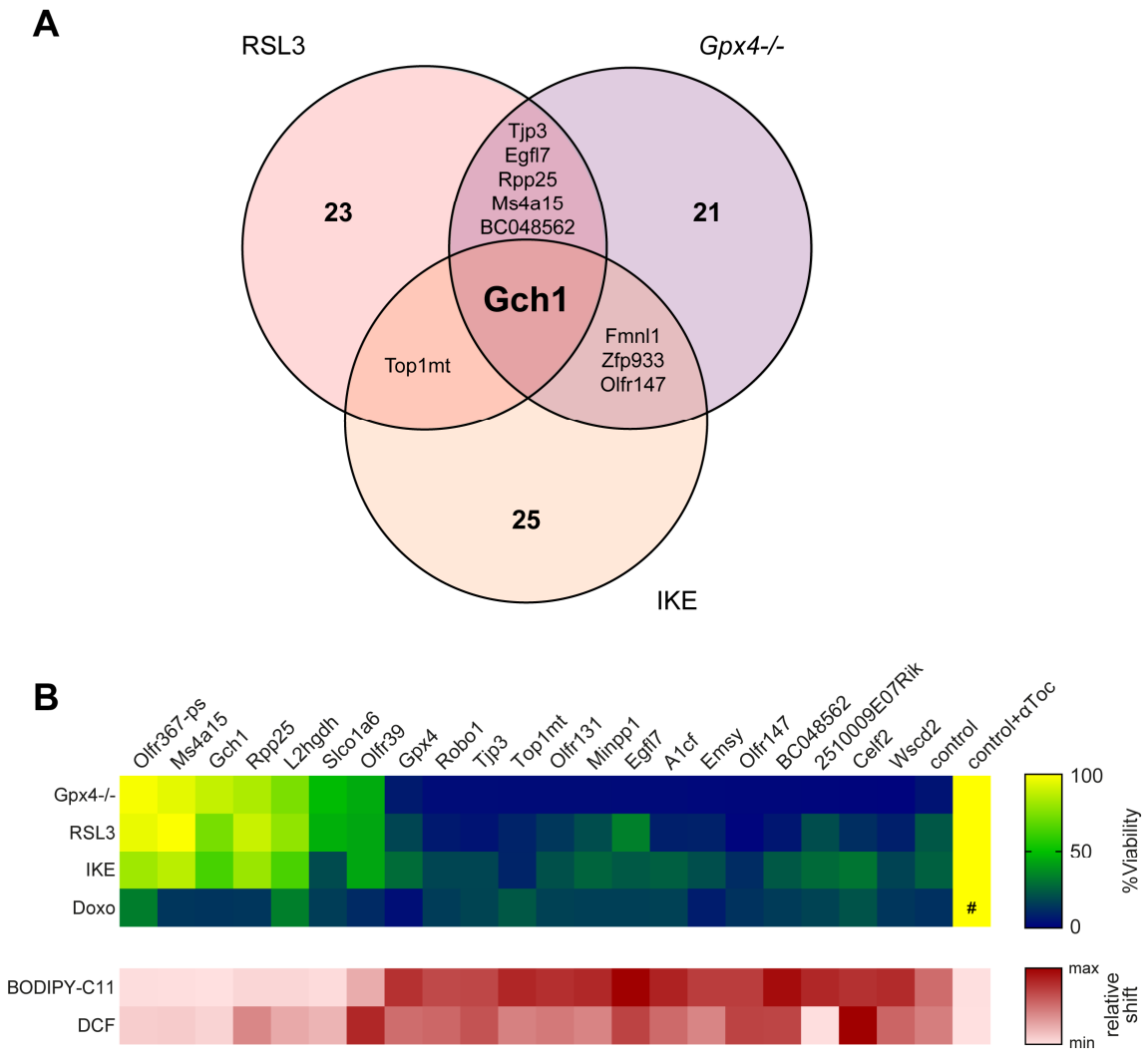

Figure 1.5 The CRISPR activation screen for genes protecting against ferroptosis (Kraft et al., 2019). (A) Venn diagram of overlapping top 30 genes found in each overexpression screen against ferroptosis inducers. (B) Heat map validating 21 overexpressing MF cell lines against challenges Gpx4-/-, 0.3 µM RSL3, 2 µM IKE and 20 µM doxorubicin (Doxo) compared to empty vector control cells (control): BODIPY 581/591 C11 (BODIPY-C11) and 2,7-Dichlorodihydrofluorescein diacetate (DCF) indicate lipid and cytosolic ROS respectively in these lines after 0.3µM RSL3 treatment for 2 h. Untreated cells (#) serve as control treatment for Doxo.

In addition, *Ms4a15* was identified under two conditions from the screen, i.e. RSL3 and GPX4-/-, and exhibited almost complete protection against ferroptosis correlated with suppression of BODIPY-C11 and DCF oxidation, comparable to α-tocopherol (Figure 1.5A, B). MS4A15 belongs to the membrane-spanning 4-domains subfamily A (MS4A) which encompasses a group of genes (MS4A1 to MS4A15 and TMEM176A and B) that primarily clustered to chromosome 11q12-13. The MS4A proteins are predicted to span the cellular

membrane four times and share similarities in their polypeptide sequence and predicted overall topological structure (Eon Kuek et al., 2016).

As reported, the human and mouse genomes contain 16 and 17 MS4A members, respectively. A recent study identified the homologs of MS4A proteins are present in all mammalian lineages as well as in many other deuterostomes. Through the process of tandem duplication, the MS4A family proteins were widely divergent during the evolution of mammals; the most amino acid residues variabilities are highly enriched within the predicted extracellular loops. In contrast to the divergence of the other MS4A family members, *Ms4a15* sequences are conserved across evolution with a single copy identified in bird genomes (Greer et al., 2016).

The functions of many of the MS4A proteins are currently not well defined, recent studies suggest they might be involved in some human diseases, only limited members have been functionally characterized although far less extensively. For example, MS4A1 (CD20), the pan B cell marker, has been shown to interact with the B cell receptor at the cell surface to regulate cell survival and proliferation (Beers et al., 2010); MS4A2 (FcεRIβ) is expressed in mast cells and basophils as part of the high affinity IgE receptor complex and regulates IgE-mediated signaling pathways (Cruse et al., 2010; Donnadieu et al., 2003); HTm4 (MS4A3) is expressed in the perinuclear and involved in hematopoietic cell cycling (Kutok et al., 2011); MS4A12 functions in colon epithelial cell cycling and store operated calcium influx (Koslowski et al., 2008).

Beyond these reports, MS4A15 is poorly understood, including amino acid sequence characteristics, subcellular localization and fundamental functions. MS4A15 is a membrane protein found primarily in lung; it might be involved in signal transduction as a component of a multimeric receptor complex like its close homolog MS4A12, which is mainly expressed in the apical membrane of colonocytes and regulates store operated calcium entry. Knockdown of MS4A12 in colon cancer cells leads to the inhibition of cell proliferation, migration, and chemotactic invasion. Previous study suggested that the expression of MS4A15 was positively associated with the overall survival probability of Lung Adenocarcinoma (LUAD) patients (Shang et al., 2017), indicating MS4A15 as a prognostic biomarker for LUAD.

To date, functional studies related to MS4A15 are rare, discovering the mechanism of MS4A15 is the main goal of this work, especially the protection role in ferroptosis.

1.5 Biomarker

The characteristics of cell surface proteins include their accessibility, the stability, and easy detection. Moreover, the cell surface proteins have attracted increasing attention due to their involvement in vital signaling pathways and determination of cell fate. Therefore, the cell surface proteins associated with various human diseases have been regarded as promising clinical biomarkers (Anderson and LaBaer, 2005), investigation of specific protein or peptide biomarkers associated with human diseases is of great implications for improvement of drug research, for early prediction of a lethal outcome and for patients to receive optimal treatment (Figure 1.6).

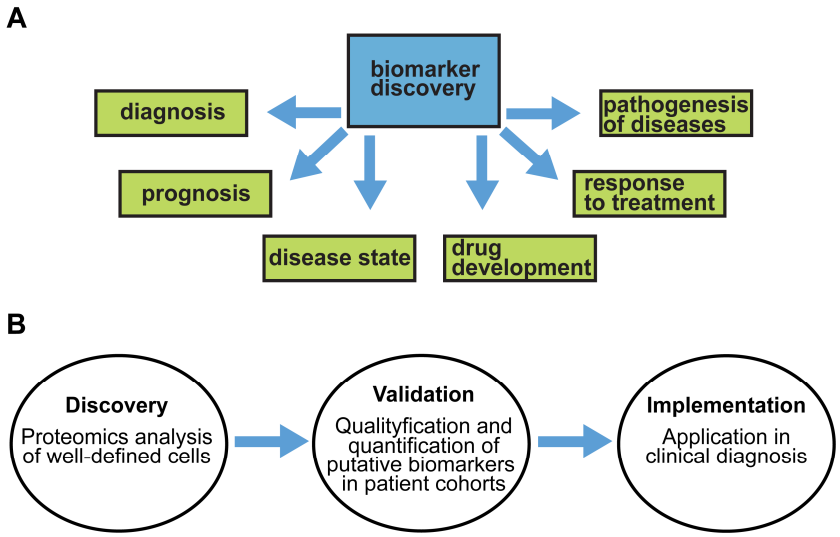

Figure 1.6 The discovery of biomarkers. The implications of biomarker discovery (A) and three major steps of biomarker research workflow (B).

Cell death is a fundamental biological process maintaining tissue homeostasis, while excessive or defective cell death leads to a large number of human pathologies, such as cancers stimulated by failure of cell death execution, and neurodegenerative diseases by increased cell death. Investigation of the cell death molecular mechanisms in depth will likely improve therapeutic strategies; however, the lack of adequate and appropriate biomarkers is the obstacle to stratify patients and to design optimal treatment for the corresponding patient subgroups. Nevertheless, retrospective extrapolation using TUNEL has revealed by exclusion a substantial contribution of apoptosis in human colorectal cancer (Simpson et al., 2013) and cardiovascular disease (Singh et al., 2011), and non-apoptotic cell death in stroke (Li et al., 2003), Alzheimer's (Lassmann et al., 1995), Parkinson's (Hartmann and Hirsch, 2001), and Huntington's (Turmaine et al., 2000) diseases.

Ferroptosis is a non-apoptotic iron-dependent cell death (Dixon et al., 2012), which was extensively characterized. The cumulative implication of ferroptosis in ALS (Kwan et al., 2012), Alzheimer's (Ghosh et al., 2014; Zhang et al., 2018), Parkinson's (Do Van et al., 2016) and Huntington's (Skouta et al., 2014), among others (Di Fonzo et al., 2014; Tuo et al., 2017; Zille et al., 2017), is based on cell culture experiments and in vivo evidence, whereas no conclusively evidence has been demonstrated under pathological conditions in humans so far.

Insights into adequate ferroptosis biomarkers for human diseases will likely provide more chances to target this process for rational therapy design. Therefore, central to current research and clinical efforts is to find ferroptosis-specific biomarkers of human diseases for detection of disease state, accurate diagnosis, better prognosis, and drug improvement, which can accelerate medical development.

1.6 Aim of this work

Investigation of ferroptosis in pathological research and treatment has become a hotspot and focus since it has been first reported in 2012 (Dixon et al., 2012). However, how to interfere with ferroptosis in development of human diseases is still a big challenge, it needs further exploration of the specific molecular mechanisms, downstream signaling pathways and functional changes.

In general, the goals of this work are

(i) To systematically characterize the mechanisms of the novel four-pass membrane protein MS4A15 in mediating ferroptosis resistance.

(ii) To discover promising biomarkers of ferroptosis for early detection and diagnosis of human degenerative diseases.

The real challenge related to this project was to link calcium action and lipids remodeling and to obtain appropriate materials for histochemical staining of biomarker candidates. Calcium signaling is highly complex. The role of calcium in ferroptosis and the function of MS4A15 are poorly understood. To address this from a new perspective, a systematical biology approach was used to analyze the mechanisms, signaling pathways and therapeutic potential of ferroptosis. Moreover, no specific biomarkers of ferroptosis for human diseases have been identified at present, the study of ferroptosis-specific biomarkers of is important for proposing new targets for the treatment of related diseases.

2. Preliminary study of MS4A15[1]

2.1 Introduction

With the development of techniques in biology, more distinct cell death phenotypes have been discovered in the last decades, such as apoptosis, necrosis and ferroptosis. Ferroptosis is a newly identified form of regulated cell death characterized by the iron-dependent accumulation of lipid hydroperoxides to lethal levels (Dixon et al., 2012). This form of iron-dependent cell death is distinct from other cell death modalities (Table 1), and the mechanisms stay not fully understood.

To better understand the molecular mechanisms and signaling pathways of ferroptosis, a CRISPR activation approach was performed by the Schick lab aiming to identify new genes protect against ferroptosis (Figure 1.5A). CRISPR presents a novel approach for gene editing and regulation; so far CRISPR–Cas9-mediated overexpression/knockout screen of ferroptosis has been accomplished (Chavez et al., 2015; Konermann et al., 2015; Maeder et al., 2013; Mali et al., 2013).

Traditional molecular biology techniques restrict researchers to focus on genes with previous information reported or specific hypotheses already known. However, when a novel gene is identified, often no prior information is available and premature attempts to engage in hypothesis-driven researches may be difficult. *Ms4a15* is a novel gene identified in the overexpression screen (Kraft et al., 2019). According to previous research, information regarding MS4A15 is rare, basic information including subcellular localization and fundamental functions of MS4A15 is poorly understood.

Here, genetic manipulation was adapted to study the function of MS4A15 (Figure 1.5B). Cell viability of cellular status upon lethal compound treatment is generally useful for understanding changes induced by the compound treatment in an unbiased manner. Moreover, RNA sequencing, proteomics technology and bioinformatics methods have improved drastically recently, which can be employed as the first step to stratify functionally relevant signaling components, to provide basic insights of MS4A15. Since these technologies only hint to the pathway or direction, hypotheses generated by their analyses need to be validated in independent experiments.

[1] Chapter 2-4 were adapted from a manuscript in preparation: Shan Xin, Constanze Müller, Susanne Pfeiffer, Joel A. Schick

2.2 Results

2.2.1 MS4A15 overexpression specifically abrogates ferroptosis

Through the approach of CRISPR activation screen, the novel four-pass transmembrane protein MS4A15 was identified (Kraft et al., 2019). To test whether MS4A15 preferentially inhibits ferroptosis or it is generally protective against various lethal stimuli, a pooled CRISPRa *Ms4a15* overexpressing cell line (*Ms4a15* OE) was generated using mouse immortalized fibroblasts (MF) (Figure 2.1A) and a 20-fold increase in transcripts was observed compared to a control line with an empty vector.

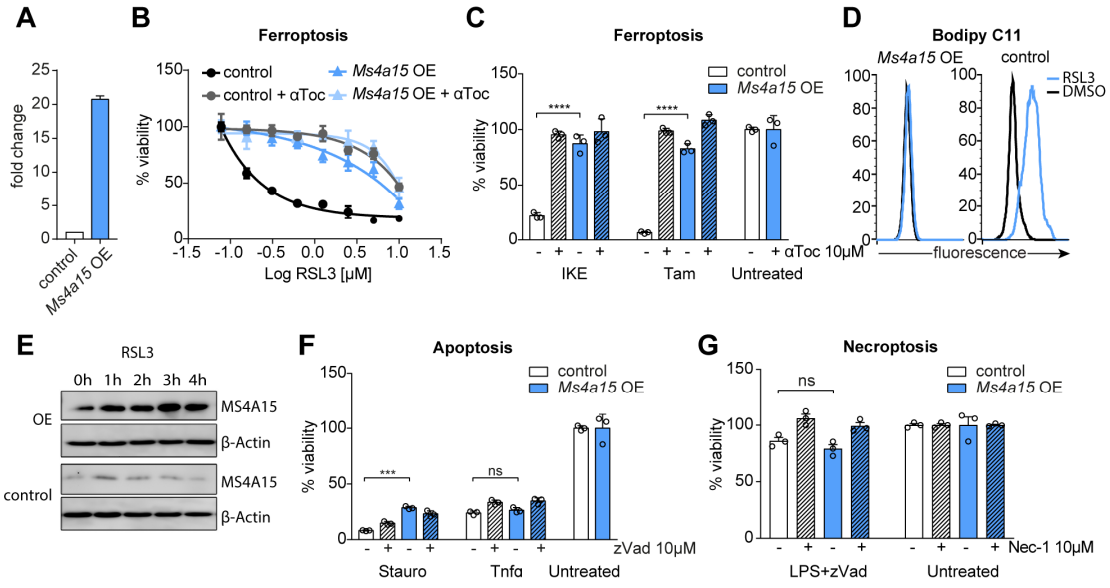

Figure 2.1 MS4A15 specifically protects cells against ferroptosis. (A) Relative *Ms4a15* mRNA expression levels in *Ms4a15*-overexpressing MF-dCas9-Ms4a15 (*Ms4a15* OE) cells and empty vector control (control) immortalized mouse fibroblasts. Relative mRNA expression is shown as mean ± SD of n = 3 technical replicates of three independent repetitions of the experiment with similar results. (B) Dose response curves against RSL3 treatment in MF *Ms4a15* OE cells and control. Addition of 10 μM αToc serves as rescue control for ferroptosis. (C) Survival of MF *Ms4a15* OE cells compared to control against ferroptosis inducers: Ferroptosis induced with 2 μM IKE and Gpx4–/– by using 1 μM tamoxifen with 10 μM αToc rescue. (D) Lipid peroxidation induced by 0.3 μM RSL3 induction in MF *Ms4a15* OE cells and control cells measured by BODIPY 581/591 C11 stain (BODIPY-C11). A typical FACS histogram of *n* = 4 technical replicates of three independent repetitions is depicted. (E) Western blots of MS4A15 protein expression level of MF *Ms4a15* OE cells and control cells after RSL3 treatment (500nM) for 0h, 1h, 2h, 3h, and 4h, respectively. (F-G) Survival of MF *Ms4a15* OE cells compared to control cells against inducers of cell death: Extrinsic apoptosis induced by 20 ng/mL tumor necrosis factor α (TNFα) with 10 μM z-VAD-FMK (zVAD) rescue (F). Necroptosis induced by 1 μg/mL lipopolysaccharide (LPS) cotreatment with 10 μM zVAD with 10 μM necrostatin-1 (Nec-1) rescue (G). Viability data are plotted as mean ± SD of n = 3 technical replicates of at least three repetitions of the experiment with similar outcomes.

Further, when *Ms4a15* OE and parental control cells were treated with different ferroptosis inducers: RSL3 for targeting GPX4, IKE for blocking system Xc^- and tamoxifen for genetic ablation of Gpx4; a strong protection of *Ms4a15* OE was observed(Figure 2.1B, C). One of the hallmarks of ferroptosis is lipid peroxidation; then the lipid-soluble fluorescent indicator, Bodipy-C11, was used to detect lipid peroxidation of *Ms4a15* OE and control cells after treated with RSL3 for three hours. Control cells generated a robust lipid oxidation, while *Ms4a15* OE was virtually unchanged, indicating the role of MS4A15 in protecting from lipid peroxidation (Figure 2.1D). To test whether MS4A15 works in other cell types as well, *MS4A15* overexpression cell lines were constructed using non-small-cell lung cancer Calu-1 cells, because *MS4A15* is highly expressed in human lung tissue (Uhlen et al., 2017). The Calu-1 cells were treated with ferroptosis inducer IKE and conserved protection was observed by both *MSA15*-pCAG-IRES-Puro transfection (Figure 2.2A) and *MS4A15*-pLVTHM viral infection (Figure 2.2B).

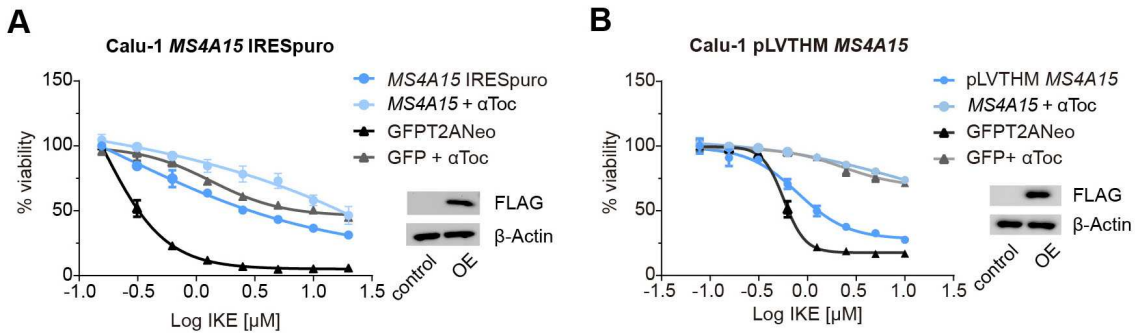

Figure 2.2 Overexpression of MS4A15 in Calu-1 cells protects from ferroptosis. Viability of transfection (A) and viral infection (B) of *MS4A15* compared to empty control in Calu-1 cells treated with RSL3. Viability data are plotted as mean ± SD of n = 3 technical replicates of at least three repetitions of the experiment with similar outcomes. Western blots indicate the overexpression of MS4A15.

To discover the activity of MS4A15 during ferroptosis, the MF cells were treated with RSL3 for up to three hours. The *Ms4a15* OE revealed increased expression level of RSL3 post-treatment compared with the low expression in control cells, suggesting that the increased activity of MS4A15 is important for cells to survive (Figure 2.1E). Next, whether *Ms4a15* protects against ferroptosis specifically or if *Ms4a15* is resistant to different stimuli was detected using extrinsic apoptosis inducer TNFα, necroptosis inducer LPS+zVAD and an unselective inducer of cell death staurosporine. No protection against TNFα and LPS+zVAD was observed, while cells treated with staurosporine showed minor resistance (Figure 2.1F, G). Together, these results indicate that overexpressed MS4A15 can robustly and specifically protect against ferroptosis.

2.2.2 MS4A15 is associated with ER-resident calcium regulators

The results in chapter 2.2.1 suggested that MS4A15 showed a conserved and specific protection on both mouse and human cells, whereas its mechanism still remains unclear. Previous studies reported that MS4A15 may have potential function in different diseases based on its expression pattern and the function of its family members; however, no functional study of MS4A15 has been published yet (Beers et al., 2010; Cruse et al., 2010; Donnadieu et al., 2003; Koslowski et al., 2008; Kutok et al., 2011; Shang et al., 2017).

To investigate the role of MS4A15 more precisely, an immunoprecipitation assay was performed to discover its function according to the interaction proteins. Human C-terminal FLAG-tagged *MS4A15* was constructed and expressed in HEK293 cells and the flag-tag was pulled down. The samples were analyzed using quantitative proteomics. Control GFP-expressing lysates and *MS4A15* OE lysates were probed with anti-FLAG antibodies and differential proteins interpreted as the fold change (FC) $\log_2$(MS4A15/GFP). A robust positive enrichment was seen for MS4A15 itself (p=2.32E-05 (two tailed t-test); $\log_2$FC=9.17) while an expected negative enrichment was seen for GFP (p=0.012; $\log_2$FC=-3.98) (Figure 2.3A).

Strikingly, the highest scoring protein was TMEM33 (p=4.33E-06; $\log_2$FC=20.46), which has featured prominently as a endoplasmic reticulum (ER) resident membrane-bound regulator of intracellular calcium release and cell migration (Arhatte et al., 2019). Other highly enriched proteins include ERLIN1 and ERLIN2 which are located in the ER and known to help the degradation of IP_3Rs. Additional identified proteins such as DNAJ family members are involved in ER-associated degradation (ERAD). Of note, these all were calcium related molecules being pulled down together.

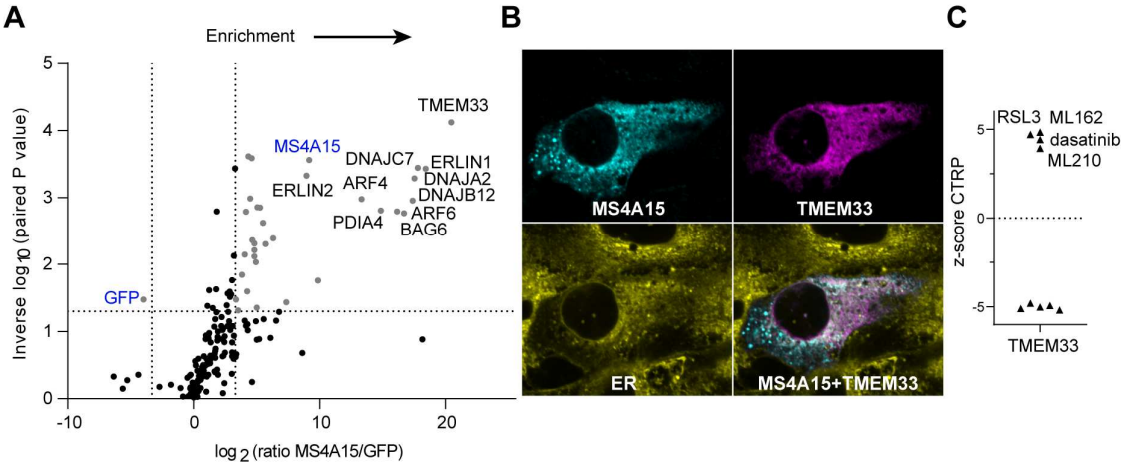

Figure 2.3 MS4A15 binds and co-localizes with TMEM33. (A) Co-immunoprecipitation of MS4A15 with TMEM33 in HEK293T cells when MS4A15 is pulled down. GFP-expressing lysates were used as control. (B) Localization of MS4A15-flag (cyan), TMEM33-myc (magenta) and ER tracker

(concanavalin A, yellow) in Calu-1 cells. The merged image shows co-localization is shown at the right-bottom panel. Scale bars, 10 µm. (C) The extent of correlation between TMEM33 and cytotoxicity of each compound. Data were pulled up from The Cancer Therapeutics Response Portal (CTRP) database. Plotted values are z-Scored correlation coefficients.

In fact, TMEM33 has been reported to be localized to the ER. Therefore, to detect the localization of MS4A15, human C-terminal FLAG-tagged *MS4A15* and C-terminal MYC-tagged *TMEM33* were co-transfected into non-small-cell lung Calu-1 cells and overlapping subcellular localization of MS4A15 and TMEM33 proteins to the ER has been confirmed (Figure 2.3B). Additionally, when the sensitivity of TMEM33 to ferroptosis was examined through mining data of the Cancer Therapeutics Response Portal (CTRP) database for correlated compounds, the association of TMEM33 with three ferroptosis-inducing drugs (i.e. RSL3, ML162 and ML121) has been observed. Hence, these results suggested a potential function of TMEM33 in ferroptosis (Figure 2.3C).

To verify whether MS4A15 and TMEM33 have overlapping or contradictory functions, Calu-1 cells were used to generate transient overexpression and knock down cell lines. However, neither TMEM33 overexpression (Figure 2.4A) nor TMEM33 siRNA knockdown (Figure 2.4B) has virtual impact on ferroptosis sensitivity, indicating that TMEM33 is not sufficient to augment *MS4A15* OE protection. Therefore, MS4A15 may have an independent function in mediating ferroptosis sensitivity at the ER.

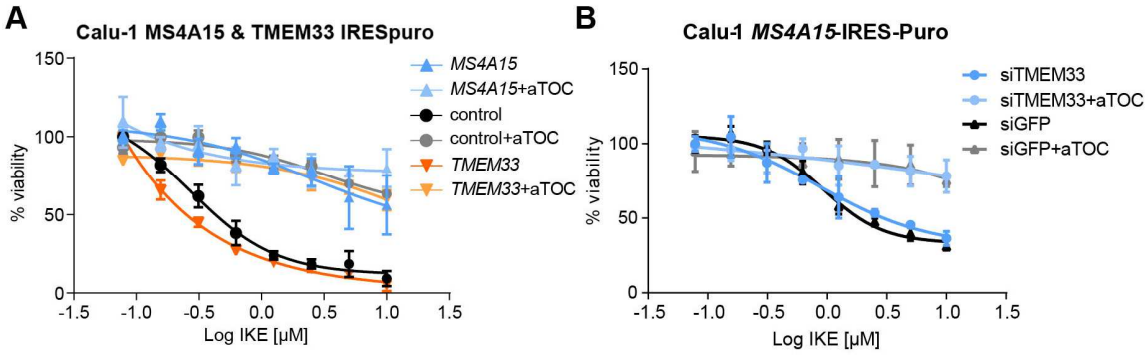

Figure 2.4 MS4A15 protects from ferroptosis independently. (A) Survival of Calu-1 *MS4A15* OE and Calu-1 *TMEM33* OE cells compared to control against IKE with 10 µM αToc rescues. (B) Survival of Calu-1 siTMEM33 cells compared to control of Calu-1 siGFP against IKE with 10 µM αToc rescues. Viability data are plotted as mean ± SD of $n = 3$ technical replicates of at least three independent repetitions of the experiment with similar outcomes.

2.2.3 MS4A15 informatics supports intracellular calcium role

As discovered, several calcium related molecules (e.g. TMEM33, ERLIN1/2, and DNAJA2) were identified from MS4A15 immunoprecipitation, indicating a potential role of MS4A15 in regulating calcium homeostasis. Supporting this, a bioinformatics analysis was performed using The Cancer Genome Atlas database (TCGA) database and a positive correlation between *MS4A15* expression and gene ontology Ca^{2+} signaling factors was found in lung tumors (Pearson coefficient R = 0.49; Figure 2.5A). As TMEM33 has been reported as a modulator of calcium homeostasis through inhibiting inositol 1,4,5-trisphosphate (IP_3) dependent calcium signaling, and ERLIN proteins regulate IP_3 receptors and reside at the interface between calcium flux and lipid regulation (Kuchay et al., 2017; Pearce et al., 2009), IP_3 is a second messenger molecule binds to IP_3 receptors to release Ca^{2+} into the cytosol. The expression level of IP_3 receptors in *Ms4a15* OE cells has been investigated using western blot and a marked downregulation of IP_3R1 protein was observed (Figure 2.5B), suggesting that reduced IP_3R1 levels may be a consequence of disrupted calcium homeostasis.

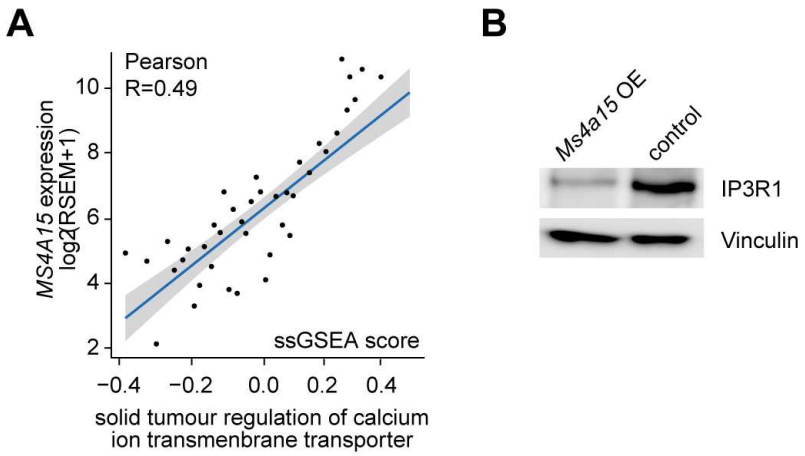

Figure 2.5 MS4A15 associated with calcium flux in the ER. (A) ssGSEA analysis shows positive correlation between MS4A15 and gene ontology calcium signaling members in human lung tumors. (B) Western blots indicate the IP_3R1 level is dramatically downregulated in *Ms4a15* OE compared with control cells.

The correlations between MS4A15 and different pathways were analyzed in LUAD, because *MS4A15* is highly expressed in lung (Uhlen et al., 2017). Comparison of the top co-regulated KEGG pathways from LUAD in TCGA revealed the strongest association of *MS4A15* with vascular smooth muscle contraction (dependent on intracellular [Ca^{2+}]), PPAR signaling, arachidonic acid metabolism, and calcium signaling (Figure 2.6A).

The most highly co-regulated genes associated with MS4A15 in LUAD were shown in the heat map, including chloride intracellular channel protein 5 (*CLIC5*), cardiac troponin (*TNNC1*), sushi domain containing 2 (*SUSD2*), and the beta-1 adrenergic receptor (*ADRB1*). CLIC5 is a redox sensitive membrane ion channel involved in generation of phosphatidylinositol 4, 5-bisphosphate (PIP2) and cell migration was included (Al-Momany et al., 2014). TNNC1 is a highly sensitive Ca^{2+} binding protein which also acts as a Ca^{2+} buffer. SUSD2 is a membrane protein that mediates cell adhesion and migration (Zhang et al., 2017). ADRB1 is a beta-adrenergic G-protein coupled receptor that stimulates IP_3 release and calcium flux (Figure 2.6B). All these genes were found to be upregulated with *MS4A15* (Figure 2.6C; R>0.5) and showed strong correlation with calcium regulation (Figure 2.6D; R>0.5), these evidences demonstrate that these genes have a significant association with Ca^{2+} signaling in primary human cancer tissue. In contrast, TMEM33 displayed an inverted correlation with MS4A15 expression (Figure 2.6C; R = -0.27) and Ca^{2+} transporters (Figure 2.6C; R = -0.31), indicating an unnecessary function of TMEM33 for MS4A15. Taken together, these results suggested that MS4A15 may play an independent role in regulating calcium processes in the ER.

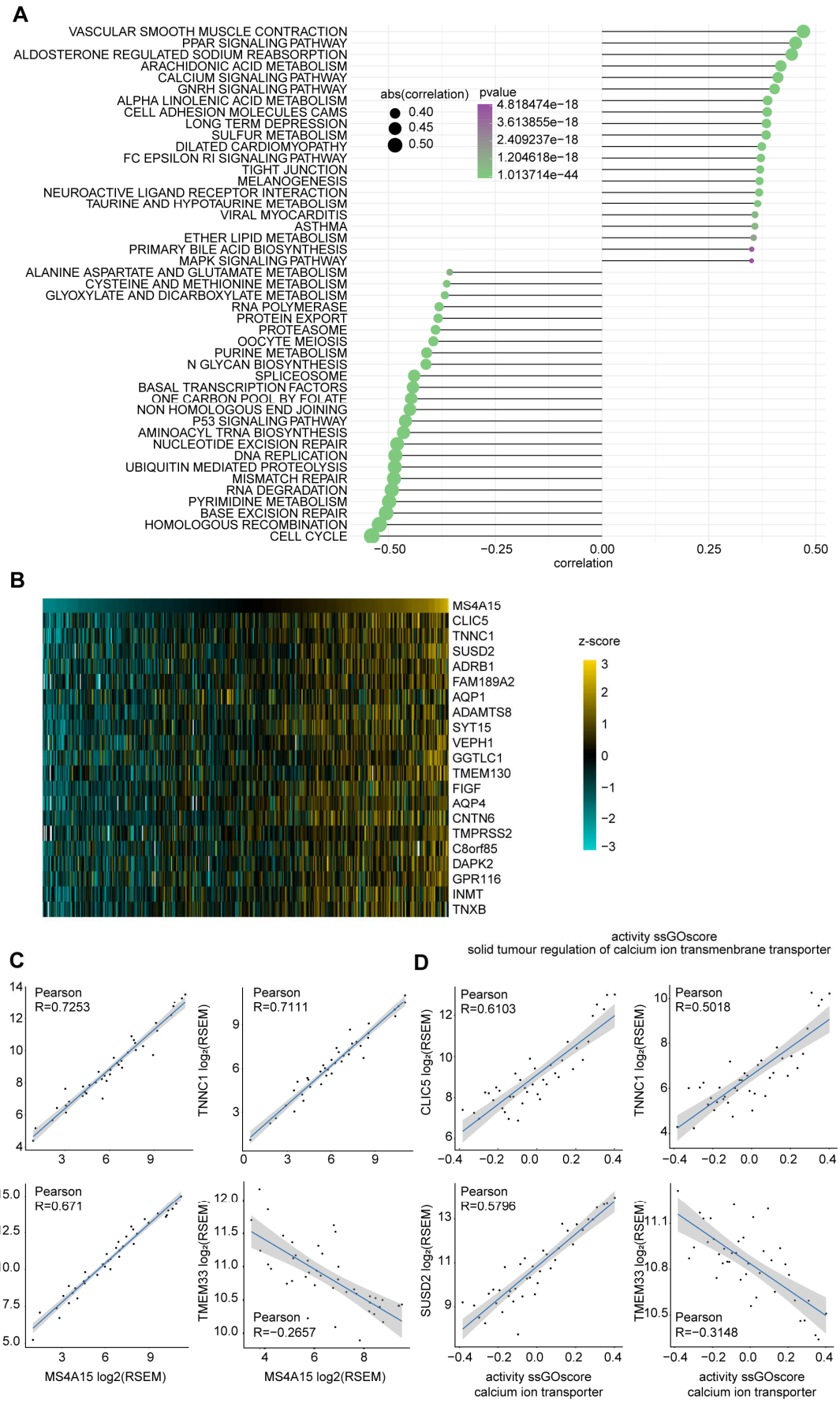
A
VASCULAR SMOOTH MUSCLE CONTRACTION
PPAR SIGNALING PATHWAY
ALDOSTERONE REGULATED SODIUM REABSORPTION
ARACHIDONIC ACID METABOLISM
CALCIUM SIGNALING PATHWAY
GNRH SIGNALING PATHWAY
ALPHA LINOLENIC ACID METABOLISM
CELL ADHESION MOLECULES CAMS
LONG TERM DEPRESSION
SULFUR METABOLISM
DILATED CARDIOMYOPATHY
FC EPSILON RI SIGNALING PATHWAY
TIGHT JUNCTION
MELANOGENESIS
NEUROACTIVE LIGAND RECEPTOR INTERACTION
TAURINE AND HYPOTAURINE METABOLISM
VIRAL MYOCARDITIS
ASTHMA
ETHER LIPID METABOLISM
PRIMARY BILE ACID BIOSYNTHESIS
MAPK SIGNALING PATHWAY
ALANINE ASPARTATE AND GLUTAMATE METABOLISM
CYSTEINE AND METHIONINE METABOLISM
GLYOXYLATE AND DICARBOXYLATE METABOLISM
RNA POLYMERASE
PROTEIN EXPORT
PROTEASOME
OOCYTE MEIOSIS
PURINE METABOLISM
N GLYCAN BIOSYNTHESIS
SPLICEOSOME
BASAL TRANSCRIPTION FACTORS
ONE CARBON POOL BY FOLATE
NON HOMOLOGOUS END JOINING
P53 SIGNALING PATHWAY
AMINOACYL TRNA BIOSYNTHESIS
NUCLEOTIDE EXCISION REPAIR
DNA REPLICATION
UBIQUITIN MEDIATED PROTEOLYSIS
MISMATCH REPAIR
RNA DEGRADATION
PYRIMIDINE METABOLISM
BASE EXCISION REPAIR
HOMOLOGOUS RECOMBINATION
CELL CYCLE
abs(correlation)
0.40
0.45
0.50
pvalue
4.818474e−18
3.613855e−18
2.409237e−18
1.204618e−18
1.013714e−44
−0.50
−0.25
0.00
0.25
0.50
correlation
B
MS4A15
CLIC5
TNNC1
SUSD2
ADRB1
FAM189A2
AQP1
ADAMTS8
SYT15
VEPH1
GGTLC1
TMEM130
FIGF
AQP4
CNTN6
TMPRSS2
C8orf85
DAPK2
GPR116
INMT
TNXB
z-score
3
2
1
0
−1
−2
−3
C
Pearson
R=0.7253
CLIC5 log2(RSEM)
Pearson
R=0.7111
TNNC1 log2(RSEM)
Pearson
R=0.671
SUSD2 log2(RSEM)
MS4A15 log2(RSEM)
Pearson
R=−0.2657
TMEM33 log2(RSEM)
MS4A15 log2(RSEM)
D
activity ssGOscore
solid tumour regulation of calcium ion transmenbrane transporter
Pearson
R=0.6103
CLIC5 log2(RSEM)
Pearson
R=0.5018
TNNC1 log2(RSEM)
Pearson
R=0.5796
SUSD2 log2(RSEM)
activity ssGOscore
calcium ion transporter
Pearson
R=−0.3148
TMEM33 log2(RSEM)
activity ssGOscore
calcium ion transporter

Figure 2.6 Bioinformatics show correlation between *MS4A15* and calcium. (A) ssGSEA shows the correlation between *MS4A15* and the top enriched GO-biological pathways. (B) Heat map of the top expressed genes associated with *MS4A15* in LUAD. (C-D) ssGSEA shows the correlation between four genes and *MS4A15* (C) or calcium factors (D) in lung cancers. The log_2(rsem+1) value means the expression level of *CLIC5*, *SUSD2*, *TNNC1* and *TMEM33*, respectively.

2.3 Discussion

In this chapter, the role of the novel four-pass transmembrane protein, MS4A15, was initially investigated, suggesting a potential role of MS4A15 in modulating calcium homeostasis.

First, *Ms4a15* was verified to protect specifically against ferroptosis other than different stimuli relating to cell death induction (e.g. apoptosis, necrosis). To further discover the function of MS4A15, a pull-down assay was performed. With the identification that the top-scored proteins involved in IP_3R regulation, it was further experimentally demonstrated that the IP_3R level of *Ms4a15* OE cells were significantly downregulated. Moreover, MS4A15 was co-localized with TMEM33 in the ER by immunofluorescence microscopy; nevertheless, TMEM33 is not necessary to augment *MS4A15* OE protection. Therefore, MS4A15 may play an independent role in protecting against ferroptosis through regulating calcium homeostasis.

MS4A15 belongs to the MS4A family which is not well characterized. There are several publications about this family, such as function as olfactory receptors, but MS4A15 is not investigated in those studies. MS4A1/CD20, a component of SOCE activated by the B-cell receptor, accounts for recruiting immune effectors as well as mediates cell growth arrest and cell death within the lipid raft (Deans et al., 2002; Shan et al., 2000). MS4A12, a very close homolog of MS4A15, blocks the replenishment of calcium through acting as a part of SOCE in intestinal cells. MS4A12 also functions as a modulator of epidermal growth factor receptor (EGFR) signaling to regulate calcium flux (Koslowski et al., 2008). Ca^{2+} is a universal secondary messenger, which achieves specificity using complex signaling modalities. Based on the evidences of MS4A15 and MS4A12, the hypothesis was put up that MS4A15 may also be involved in regulating calcium homeostasis.

In fact, TMEM33 has been reported as a modulator of Ca^{2+} homeostasis through inhibiting IP_3-dependent calcium signaling, impeding Ca^{2+} refilling of endolysosomes, and preventing autophagic flux upon ER stress. Moreover, TMEM33-mediated calcium oscillations are able to drive the formation of endothelial tip cell filopodia and EC migration (Arhatte et al., 2019; Savage et al., 2019). Activated IP_3Rs interact with many proteins that mediate their degradation, component of the ERLIN1/ERLIN2 complex mediates the ubiquitination of IP_3Rs and the subsequent endoplasmic reticulum-associated degradation (Wright and

Wojcikiewicz, 2016; Wright et al., 2018). DNAJ chaperone family members are required to promote protein folding and trafficking, prevent aggregation of client proteins, and promote unfolded proteins to ERAD (Shen et al., 2002).

Examination of the activity of IP_3R displayed a dramatically decrease of IP_3R1 in *Ms4a15* OE compared with control cells, indicating that MS4A15 participates in the process of regulating Ca^{2+} homeostasis through affecting IP_3R expression level, however, whether MS4A15 and IP_3R have an additional relationship remains unclear. In the calcium pathway, PIP_2 functions as a substrate for hydrolysis by phospholipase C (PLC) to generate diacylglycerol (DAG) and IP_3 (Michell et al., 1981). DAG activates the calcium-dependent Protein Kinase C (PKC) with the help of the Ca^{2+} released from the ER. IP_3 enters the cytoplasm and activates IP_3Rs to cause a conformational change that leads to calcium release from intracellular Ca^{2+} stores. The reduction of IP_3R1 in *Ms4a15* OE suggests a potential role of MS4A15 in regulating Ca^{2+} release from the ER. Further support was provided by the bioinformatics analysis of the association of *MS4A15* and Ca^{2+} factors in LUAD. All the genes found to be upregulated with *MS4A15* showed strong correlation with Ca^{2+}, demonstrating a strong association with signaling mechanisms involving Ca^{2+} in primary human cancer tissue.

In summary, MS4A15 is associated with calcium and displays a protective effect against ferroptosis strongly and specifically.

Acknowledgement

I thank Susanne Pfeiffer for generation of MF *Ms4a15* OE cell line and detection of lipid peroxidation, Dr. Juliane Merl-Pham for mass spectrometry of the pull-down samples, and Xuanwen Bao for bioinformatics analysis.

3. Functional characterization of MS4A15

3.1 Introduction

MS4A15 shows correlation with calcium in primary human cancer tissue, but cell signaling is very complicated to be effectively queried with existing technology. The activity of a certain protein depends on the abundant cross talk and conditional dependence, therefore, computational interpretation of genomics data using current annotations is not adequate to understand proteins relevant to biological events of interest, while functional studies often give more informative results. Generally, genetic manipulation and pharmacological perturbation approaches are frequently used to distinct the certain biological event of a particular gene.

In adults, there exists about 1,000 g of calcium, which is the fifth most abundant element in the human body. Ca^{2+} plays a vital role in controlling diverse processes such as growth, migration, and cell death. It can trigger protein function through changing protein conformation and local charge, which are versatile tools for signaling transduction. In emphasizing the importance of Ca^{2+} signaling, no other molecule does a better job than Calmodulin, which is an intracellular target of Ca^{2+} that amplifies the diminutive size of Ca^{2+} to the scale of binding proteins (Abzhanov et al., 2006). GCaMP6s is a widely used genetically encoded fluorescent Ca^{2+} indicator consists of the calmodulin-binding peptide M13 and shows high sensitivity and slow decay kinetics.

There is a huge difference between intracellular (~100 nM free) and extracellular (~2 mM) Ca^{2+} concentrations (Figure 3.1 A). Hundreds of cellular proteins have been reported to be involved in the process to control Ca^{2+}, these include phospholipases, PIP_2, inositol (1,4,5) trisphosphate (IP_3), IP_3 receptor (IP_3R), and others. (Figure 3.1A). Ca^{2+} releasing from intracellular store is a universal mechanism for signaling transduction, which can be activated either by G protein-coupled receptors (GPCRs) or by receptor tyrosine kinase (RTK) to promote PLC cleaving PIP_2 into IP_3 and DAG, IP_3 activates IP_3Rs to cause calcium release from intracellular stores and DAG activates the PKC with the help of the Ca^{2+} released from the ER. GPCRs mainly activate PLCβ via catalyzing the exchange of guanosine diphosphate (GDP) for GTP on Gα subunits, while RTKs activate PLCγ through dimerization (Figure 3.1 B). IP_3 is a ligand for the intracellular IP_3R, binding the IP_3R ER channel allows diffusion of Ca^{2+} from the ER to cytoplasm. DAG can be converted to AA by DAG lipase to generate a large amount of bio-reactive molecules, and can be phosphorylated by Ca^{2+}-sensitive DAG kinase to produce phosphatidic acid .

Ca^{2+} is constantly leaking into the cytoplasm from the ER. In response to receptor activation or extra stimulation, persistent IP_3R-mediated release of Ca^{2+} from the ER into the cytosol to drain the ER store. To compensate for this process, SERCA transporters tirelessly pump the Ca^{2+} back into the ER to keep store Ca^{2+} balance. If these channels are blocked, ER Ca^{2+} homeostasis is disrupted, therefore, targeting these pathways have been used for investigate Ca^{2+} function. To better understand the role of Ca^{2+} in cells, pharmacological approaches were discovered to modulate Ca^{2+} homeostasis, e.g. EDTA and cobalt for chelating Ca^{2+}, thapsigargin for store depletion.

The results in chapter 2 proposed that the novel membrane protein MS4A15 has a role in modulating intracellular calcium homeostasis; hence in depth investigation needs to be taken to better understand how MS4A15 mediates ferroptosis resistance through regulating calcium through genetic manipulation and pharmacological modulation.

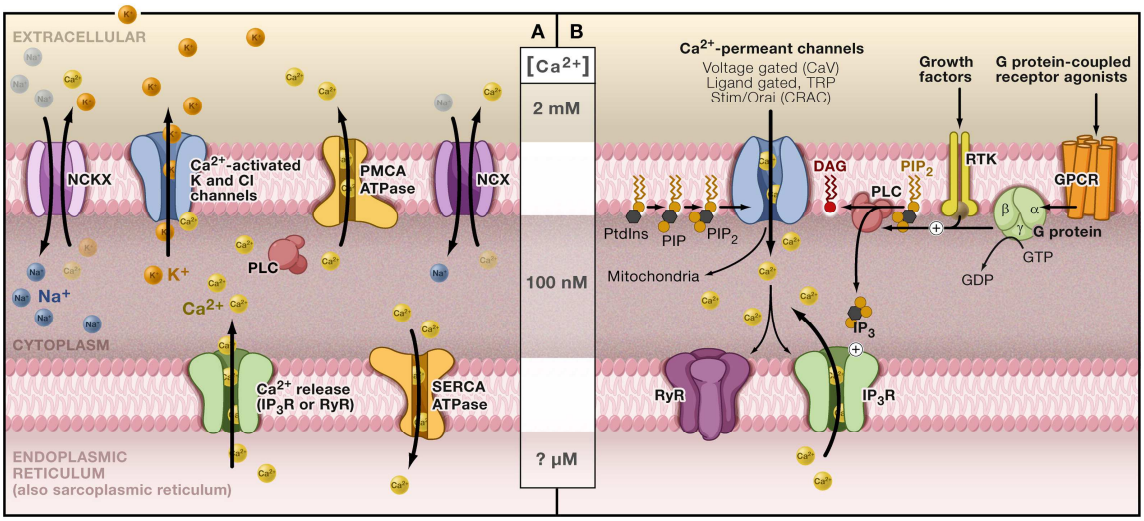

Figure 3.1 The Ca^{2+} signaling network, adapted from (Clapham, 2007). (A) Molecules and channels to maintain the gradients of intracellular and extracellular Ca^{2+}, e.g. the plasma membrane Ca^{2+} ATPase (PMCA), smooth endoplasmic reticular Ca^{2+} ATPase (SERCA), and the Na/Ca exchanger (NCX). (B) The core regulators of the Ca^{2+} signaling in response to stimulation. GPCRs or RTKs-mediated the activation of PLC to cleave PIP_2 into IP_3 and DAG, thus spanning the ER membrane and activating Ca^{2+} release.

3.2 Results

3.2.1 MS4A15 regulates calcium-mediated ferroptosis

All these evidences give a strong suggestion that calcium is involved in the process of ferroptosis, but whether or how the downstream signal is affected remains elusive. To test

whether additional signaling pathways are involved, the cells were treated with EGF to examine the activation of receptor-mediated pathway, because Ca^{2+} flux is the fastest response to receptor tyrosine kinases, and EGF signal is in involved in IP_3-, MAPK-, mTOR- and JAK-STAT pathway. As observed, IP_3R1 expression level was dramatically downregulated in *Ms4a15* OE cells in the absence of EGF. When treated with EGF, IP_3R1 level in *Ms4a15* OE cells increased to control level after 2ng/ml and 3ng/ml EGF induction. MS4A15 and IP_3R1 showed only partial co-localization, suggesting that MS4A15 does not directly affect IP_3R1 (Figure 3.2A). In addition, *Ms4a15* OE displayed increased basal phosphor-ERK level compared with the consistent weak expression in the control cells. While STAT and AKT signaling pathways remains unchanged (Figure 3.2B). These results strongly support the role for MS4A15 in Ca^{2+}-regulating processes.

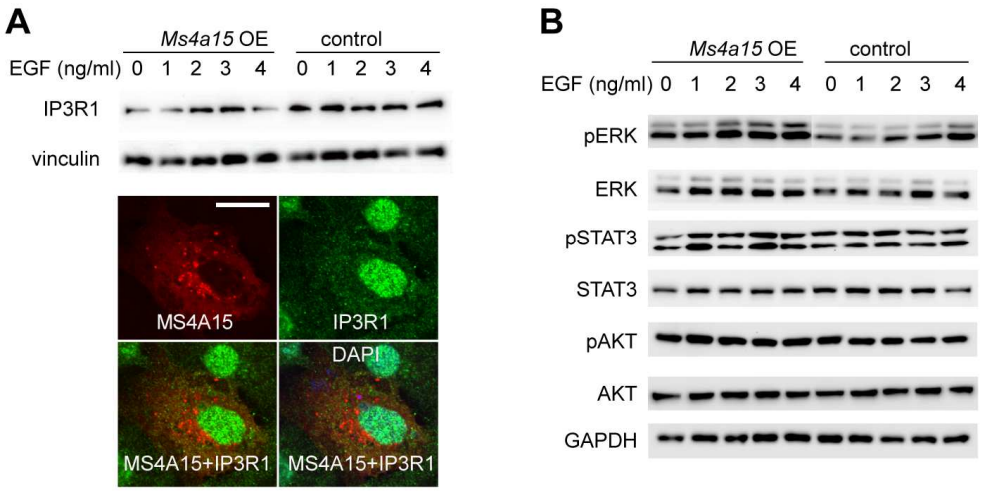

Figure 3.2 MS4A15 regulates downstream MAPK/ERK signaling. (A) Western blots of IP_3R1 in *Ms4a15* OE and control cells after 15min EGF treatment with a concentration of 0 ng/ml, 1 ng/ml, 2 ng/ml, 3 ng/ ml, and 4 ng/ml, respectively (upper panel) and co-localization of MS4A15-FLAG (red) and IP_3R1 (green) (lower panel). Scale bar, 10 µm. (B) Western blots of proteins involved in RTK signaling pathway of *Ms4a15* OE and control cells after 15 min EGF treatment with the concentrations mentioned above.

The effect of calcium modulators on *Ms4a15* OE and control MF cells were next examined using cells expressing the Ca^{2+} sensor GCaMP6s. GPCRs activate PLCβ to cleave PIP_2 into IP_3 and DAG, and elicit Ca^{2+} release from internal stores. When the cells were treated with bradykinin in calcium free medium, GPCR was activated and stimulated Ca^{2+} release from internal stores (Figure 3.3A). In *Ms4a15* OE cells, Ca^{2+} response to bradykinin stimulation was strikingly reduced compared to control cells; while adding $CaCl_2$ back to the medium induced robust Ca^{2+} transients in control cells, only limited response in *Ms4a15* OE has been observed (Figure 3.3B), suggesting less store Ca^{2+} storage and Ca^{2+} uptake inhibition of

Ms4a15 OE. To evaluate global cellular Ca^{2+} stores, cells were treated with calcium ionophore A23187 in calcium free medium and a marked decrease in released calcium from *Ms4a15* OE internal stores was witnessed (Figure 3.3B), further proving the store depletion of *Ms4a15* OE.

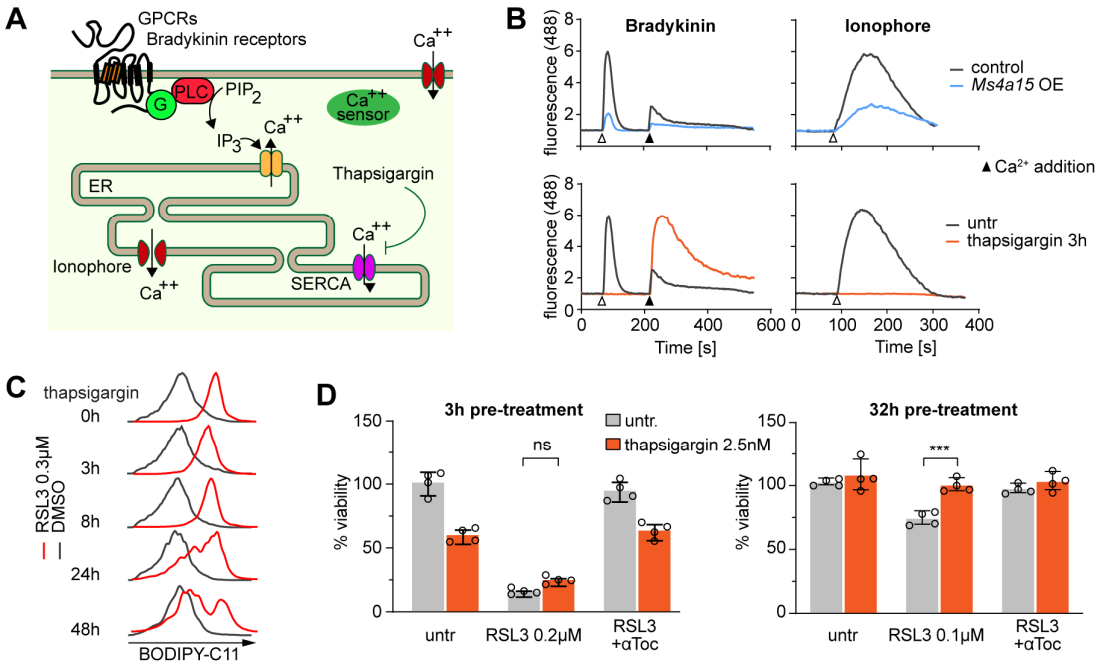

Figure 3.3 *Ms4a15* overexpression protects cells from ferroptosis through store depletion. (A) Schematic of GPCR mediated calcium pathway. (B) ER Ca^{2+} release mediated by 50 nM Bradykinin or 5 µM Ionophore (Δ) and uptake of Ca^{2+} mediated by 2 mM $CaCl_2$ addition (▲) in MF *Ms4a15* OE cells, control cells (Top), and control cells pre-treated with 0.5 µM thapsigargin for 3 h (Bottom). Calcium sensitivity was measured by Ca^{2+} sensor GCaMP6s. Data shown are representative results of three independent experiments done in triplicate. (C) Time -dependent effect of thapsigargin on lipid peroxidation induced by 0.3 µM RSL3 induction in MF *Ms4a15* OE cells and control measured by BODIPY 581/591 C11 (BODIPY-C11). A typical FACS histogram of n = 4 technical replicates of three independent repetitions is depicted. (D) Survival of MF control cells pre-treated with 2.5 nM Thapsigargin for 3 h or 32 h against 0.1 µM (3h) or 0.2 µM (32h) RSL3, 10 µM αToc serves as rescue control for ferroptosis. Viability data represent mean ± SD of n = 4 technical replicates. Statistics, one-way ANOVA.

Thapsigargin, which has similar profile with MS4A15 in regulating calcium levels, was examined for RSL3-induced ferroptosis. Disruption of calcium homeostasis by thapsigargin for up to 48h reduced lipid peroxidation detected by BODIPY-C11, corresponding to the length of treatment (Figure 3.2C). Concurrent treatment of RSL3 with thapsigargin showed slightly protection in ferroptosis response while 32h pretreatment of thapsigargin significantly protected cells (Figure 3.2D) in line with reduced lipid peroxidation (Figure 3.3C). Whereas thapsigargin treatment abolishes bradykinin and ionophore-induced store release, Ca^{2+}

uptake from the extracellular milieu is distinctly enhanced (Figure 3.3B). Therefore, enhanced ferroptosis resistance is a consequence of persistent calcium stores depletion.

The calcium release-activated channels (CRAC) channel is activated when calcium ions (Ca^{2+}) are depleted from intracellular stores, to slowly replenish the level of calcium in the ER (Hoth and Penner, 1992; Zweifach and Lewis, 1993). The ER-resident membrane protein STIM1 can sense intracellular calcium concentrations. When the store is drained, STIM1 interacts with the membrane protein ORAI to refill the stores (Zhou et al., 2018). The expression pattern of *Orais* from the RNA sequencing (RNAseq) data suggested that *Orai1* and *Orai3* were unchanged; while *Orai2* slightly increased in *Ms4a15* OE compared with control cells (Figure 3.4A), suggesting a potential compensatory role. The endoplasmic reticulum Ca^{2+}-ATPase (SERCA) plays an important role in intracellular Ca^{2+} homeostasis by pumping Ca^{2+} from the cytoplasm into the ER (Higgins et al., 2006).

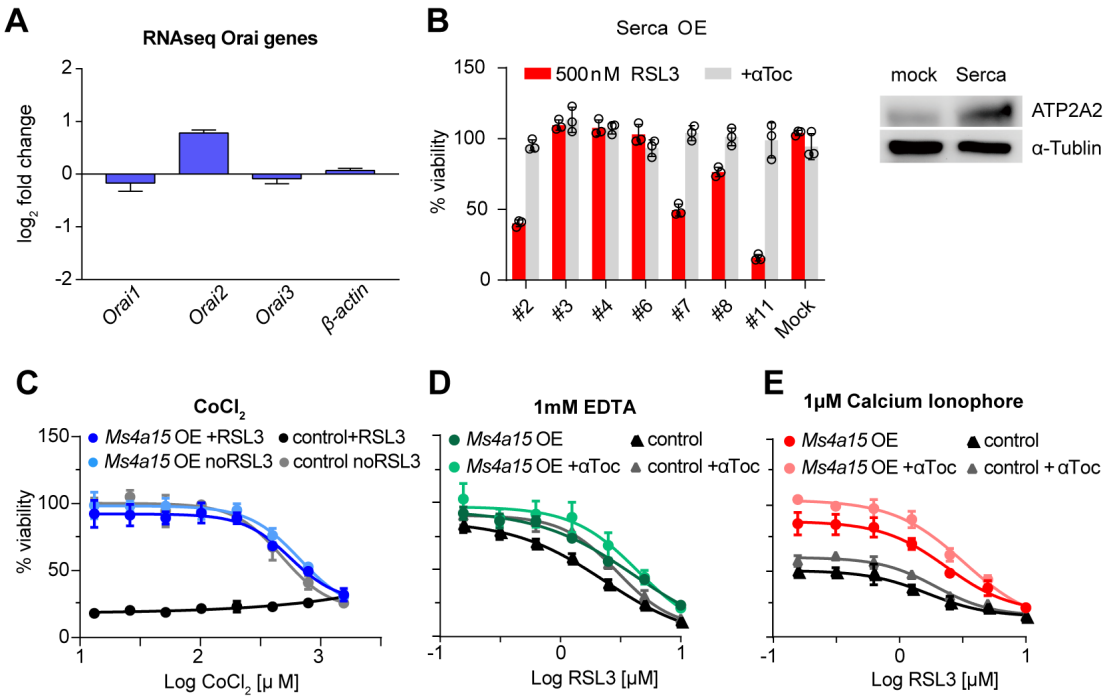

Figure 3.4 Acute flux of calcium does not affect ferroptosis resistance . (A) The changes of Orais mRNA expression in *Ms4a15* OE compared to control. Expression data are shown as mean ± SD of n = 5 technical replicates. (B) Sensitization of MF *Ms4a15* OE cells overexpressing *SERCA2* to ferroptosis induced by 500 nM RSL3 (left) and overexpression of ATP2A2 verified by western blotting. (C) Viability of cells incubated with dose amount of $Cocl_2$ challenged against RSL3. (D-E) Dose response curves of MF control cells treated with 1mM EDTA (D) or 1 μM calcium ionophore (E) against RSL3. Addition of 10 μM αToc serves as rescue control for ferroptosis. Viability data are plotted as mean ± SD of n = 3 technical replicates of at least three repetitions of the experiment with similar outcomes.

To test if levels of calcium in the cell are critical for ferroptosis sensitivity, *Atp2a2* was overexpressed in *Ms4a15* OE cells to promote ER Ca^{2+} restoration. As expected, overexpression of *Atp2a2* (*serca2*) sensitized *Ms4a15* OE cells to RSL3-induced ferroptosis (Figure 3.4B). To verify the effects of prolonged calcium depletion as opposed to acute treatment, cells were supplemented with cobalt, EDTA, and calcium ionophore, respectively, before ferroptosis induction, because ionophore triggers Ca^{2+} release, while EDTA and cobalt chloride inhibit calcium signaling in cells. However, none of these treatments affects ferroptosis sensitivity (Figure 3.4C-E). Taken together, it can be concluded that persistent disruption of calcium homeostasis in *Ms4a15* OE and long term thapsigargin-treated cells leads to ferroptosis resistance.

3.2.2 MS4A15 mediated calcium store depletion does not trigger UPR

The endoplasmic reticulum (ER) is the main site of lipid synthesis, protein folding and cellular calcium storage (Ron and Walter, 2007). As calcium has an important role in mediating chaperone function and protein folding, perturbation of ER calcium homeostasis leads to stress and activation of the unfolded protein response (UPR) (Ron and Walter, 2007). *Ms4a15* OE cells displayed persistent store depletion, RNAseq data was analyzed to explore if this results in ER stress.

During ER stress, inositol-requiring enzyme 1 α (IRE1α), encoded by the endoplasmic reticulum to nucleus signaling 1 (*ERN1)* gene, splices and induces the expression of proteins involved, such as the key modulator of UPR, X-box-binding protein 1 (XBP1). RNAseq data showed that the expression level of *Ire1* slightly increased which leads to spliced XBP1, and activated ATF4 for the C/EBP homologous protein (CHOP) (*Ddit3*) and GADD34 (*Ppp1r15a*). But according to the subtle changes, we cannot make the conclusion that UPR is activated (Figure 3.5A, B). Contrastingly, an increase in IRE1-suppressed peroxisome proliferator-activated receptor γ (PPARγ) expression has been observed, which is associated with lipogenesis (Figure 3.5B). To examine whether ER stress in general contributes to ferroptosis resistance, cells were pretreated with tunicamycin, which specifically causes protein misfolding in the ER, for ferroptosis induction. Whereas, neither no pretreatment nor 24 h pretreatment with tunicamycin could protect against ferroptosis (Figure 3.5C), indicating that alterations in Ca^{2+} homeostasis rather than triggering UPR is responsible for ferroptosis protection.

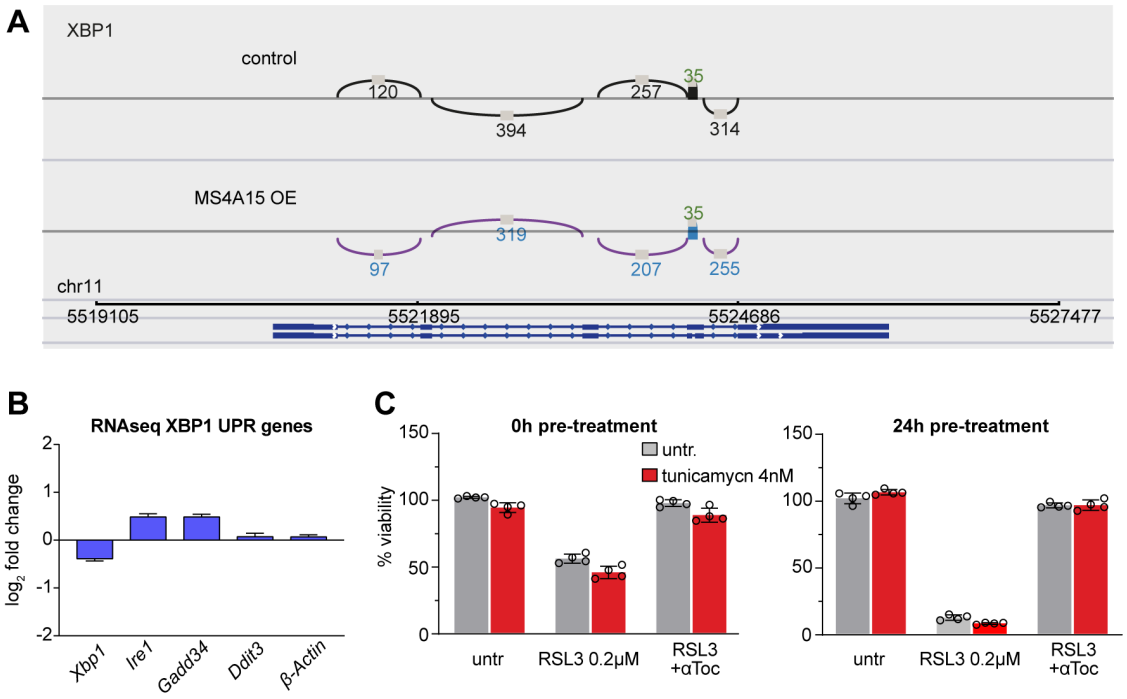

Figure 3.5 MS4A15 induced calcium depletion does not trigger unfolded protein response (UPR). (A) *Xbp1* and *Chop* mRNA expression levels in *Ms4a15* OE compared to control. (B) Expression changes of genes associated with lipogenesis in *Ms4a15* OE compared to control. Expression data are shown as mean ± SD of n = 5 technical replicates. (C) Survival of MF control cells against RSL3 after 0 h or 24 h tunicamycin pretreatment. Viability data are plotted as mean ± SD of n = 3 or 4 technical replicates.

3.2.3 MS4A15 suppresses cell migration

An important cellular feature tightly regulated by the oscillation of Ca^{2+} is migration (Berridge et al., 2000). Growth factor stimulation of IP_3 receptors mediates calcium release from cellular stores into the cytosol and activates the membrane-proximal actin cytoskeleton, thus driving migration (Feldner and Brandt, 2002). As previously reported, the EGFR signaling modulator, MS4A12, reduced cell migration via lowering the threshold for EGF-triggered Ca^{2+} entry (Koslowski et al., 2008). In addition, TMEM33 has been discovered to mediate VEGF-dependent endothelial Ca^{2+} oscillations, filopodia formation, and wound healing (Savage et al., 2019).

To investigate whether MS4A15 has an impact on cell motility, a classic wound healing assay was carried out. Intriguingly, the cellular migration of *Ms4a15* OE has been strongly impeded, as control cells filled in the gap (50 µm) after 7 h while *Ms4a15* OE did not (Figure 3.6A, B), suggesting that Ca^{2+} released from the ER stores can be mobilized and force cell

migration. This result is consistent with the analysis that the adhesion of primary LUAD tumors exhibits a positive correlation with the expression of MS4A15. Strikingly, however, MS4A15 expression is lost in cell lines established from human tumors, suggesting that the tumors may need high expression level of MS4A15 in vivo to protect against ROS species but that motility is impacted as a result (Figure 3.6C). Moreover, using the LUAD patient's data downloaded from TCGA, increased survival of patients with high *MS4A15* expression has been observed, potentially indicating that decreased metastatic migration due to disruption of calcium homeostasis may provide translational insight for cancer therapy (Figure 3.6D).

Another important cellular process tightly regulated by calcium oscillation is cell cycle. Calcium release from internal stores results in induction of resting cells (G0) to reenter the cell cycle (Berridge, 1995). Furthermore, prevention of Ca^{2+} influx via targeting store operated entry could inhibit tumor growth (Kohn et al., 1996). Therefore, the effect of *Ms4a15* expression on cell cycle was assessed, and a distinct G1-S arrest in *Ms4a15* OE cells was observed, which might resulted from store depletion (Figure 3.7).

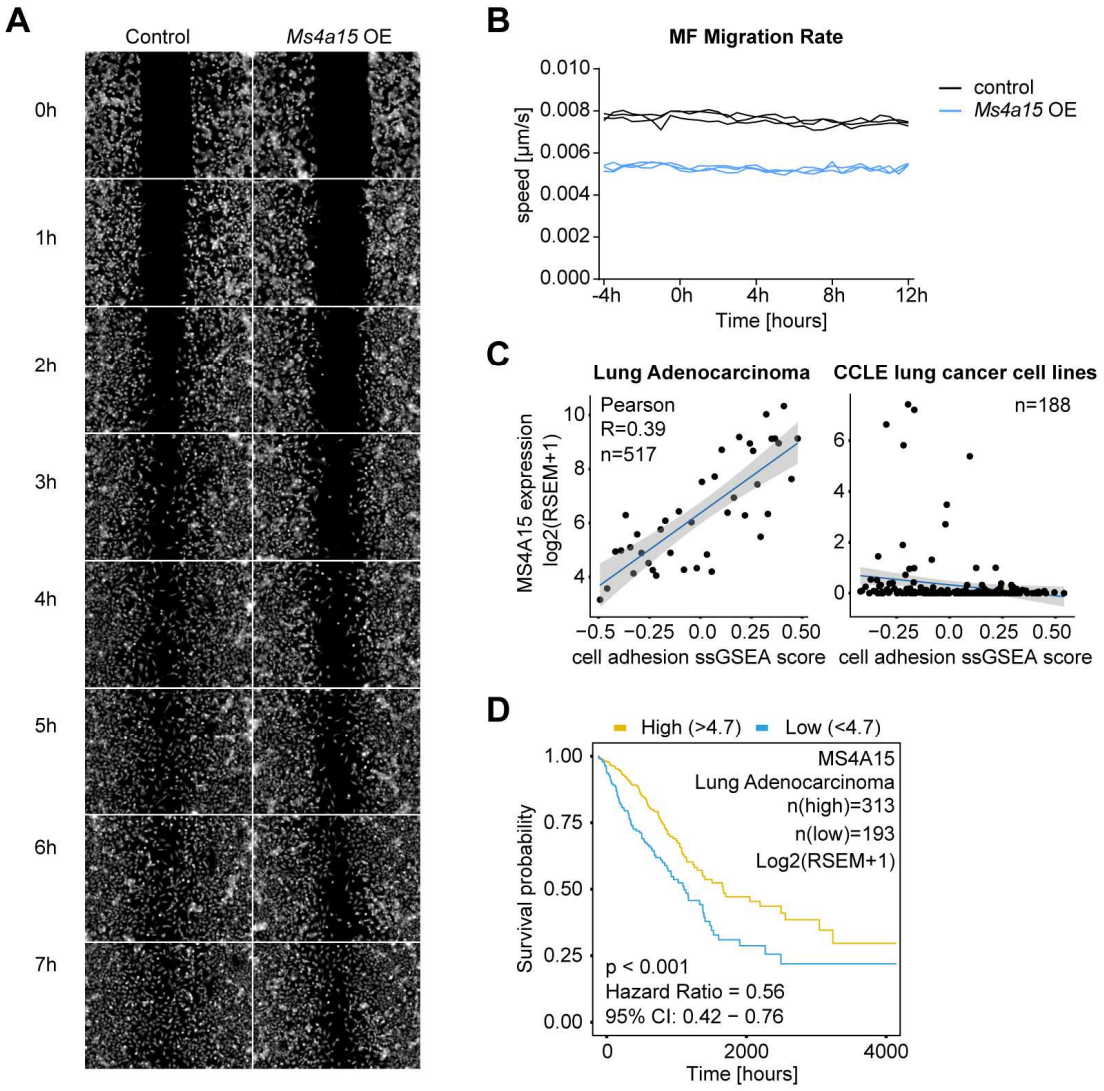

Figure 3.6 *Ms4a15* overexpression suppresses cell migration. (A-B) Digital phase contrast views (A) and migration speed (B) from the wound healing assay of *Ms4a15* OE cells and control using high-content microscopy and Harmony software. The cells were tracked for 8 h and the average speed is calculated by Harmony software. (C) Correlation of *MS4A15* expression level with tumor adhesion (left panel) and tumor cell *MS4A15* expression level in culture (right panel). Data from 188 lung cancer cell lines were used. (D) Kaplan-Meier survival analysis for LUAD patients with high and low *MS4A15* expression levels. Data from 517 patients were calculated by best-cut point method in survival, and patients were classified into low- and high-expression of *MS4A15* groups using a cutoff value of 0.5. The value means the $\log_2$(rsem+1) expression level of *MS4A15*.

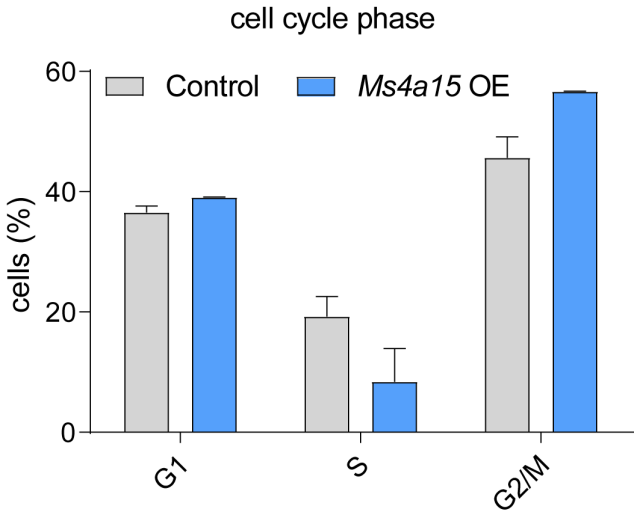

Figure 3.7 G1-S phase is arrested in *Ms4a15* OE cells. *Ms4a15* OE and control cells were cultured and analyzed under the same conditions. Cell cycle analysis is shown as bar chart of cell fractions in different cell cycle states. Cell cycle data are plotted as mean ± SD of n = 3 technical replicates of at least three repetitions of the experiment with similar outcomes.

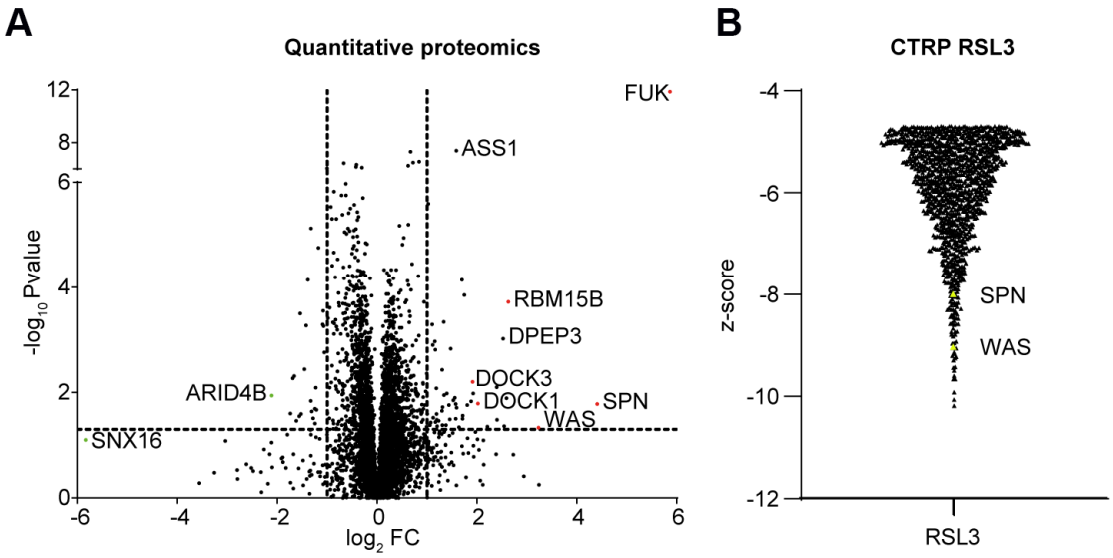

Figure 3.8 Global proteomics analysis of *Ms4a15* OE and control cells. (A) Volcano plot indicates global proteomics analysis of *Ms4a15* OE compared to control cells. The $\log_2$ of the normalized protein abundance ratios and $-\log_{10}$ of corresponding p-values of proteins quantified by at least two unique peptides were plotted. (B) The extent of correlation between protein levels and RSL3 cytotoxicity. Data were pulled up from The Cancer Therapeutics Response Portal (CTRP) database. Plotted values are z-Scored correlation coefficients.

Global proteomics analysis revealed marked increases in proteins involved in actin polymerization. In *Ms4a15* OE cells, the highly enriched Wiskott-Aldrich syndrome protein (WASP) and WAS-associated Sialophorin (SPN), as well as a potent decrease of the EGF regulator Sorting Nexin 16 (SNX16), are implicated in regulating RAC1/CDC42-mediated actin reorganization in tumor cell migration (Feldner and Brandt, 2002) (Figure 3.8A, B). Interestingly, the former two (WASP and SPN) are among the top inversely correlated proteins with resistance to RSL3, indicating the less of these two proteins in certain cells correlates to a more RSL3 sensitive phenotype (Figure 3.8A).

In line with proteomics analysis, immunofluorescence further proved increased intensity of proteins enriched in *Ms4a15* OE, especially WASP (Figure 3.9). Calcium can also regulate multiple cell functions including gene expression; however, the expression level of the known ferroptosis related proteins did not change a lot in *Ms4a15* OE cells, indicating a novel regulation pathway of MS4A15 in protecting against ferroptosis (Figure 3.10). In summary, these results support the theory that *Ms4a15* OE cells persistently deplete calcium from the ER and block calcium uptake causing depress of cellular migration, which is directly linked to ferroptosis sensitivity.

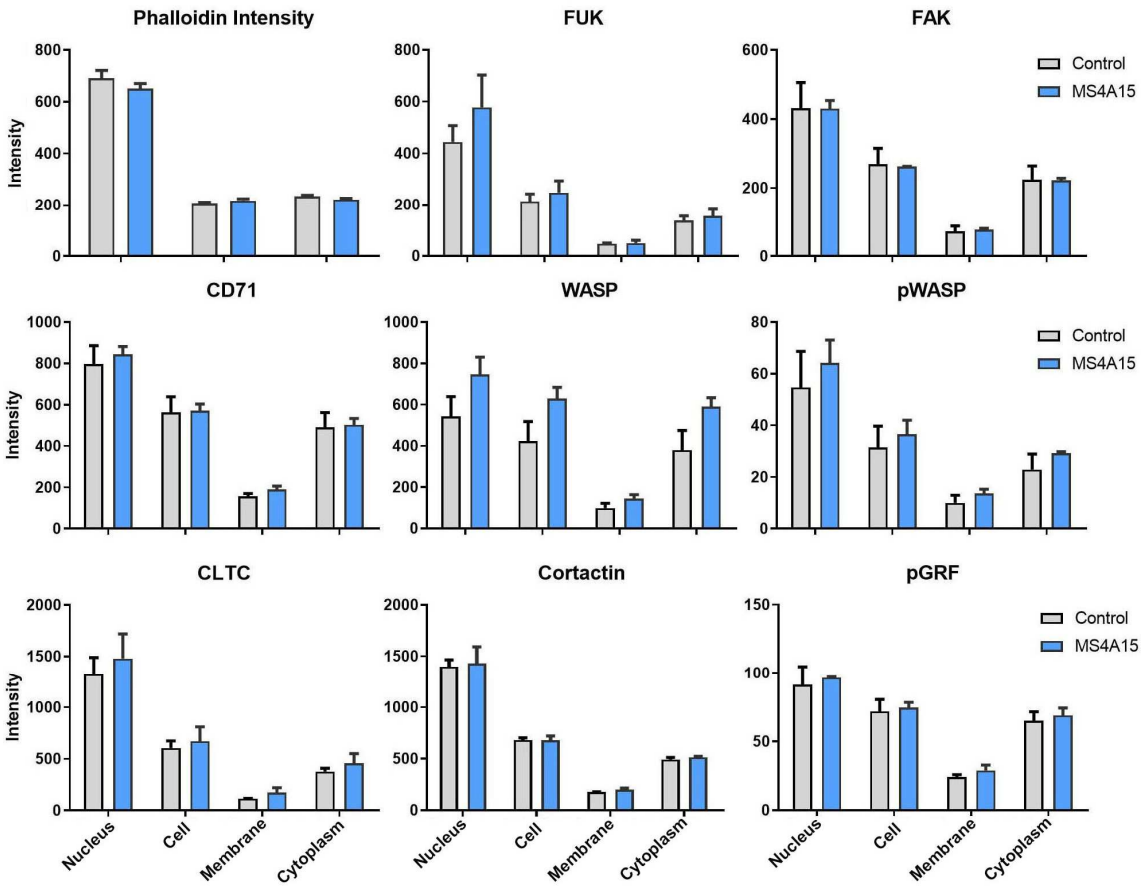

Figure 3.9 Immunofluorescence of highly enriched proteins in global proteomics. Phalloidin-TRITC was used to stain cellular skeleton F-actin. Intensity was detected with high-content microscopy and analyzed by the Harmony software; these data are plotted as mean ± SD of n = 3 technical replicates. FUK, fucose kinase; FAK, focal adhesion kinase; CD71, transferrin receptor protein 1, also short for TFRC;WASP, Wiskott-Aldrich syndrome protein; CLTC, Clathrin Heavy Chain; Cortactin, cortical actin binding protein; GRF, growth-regulating factor.

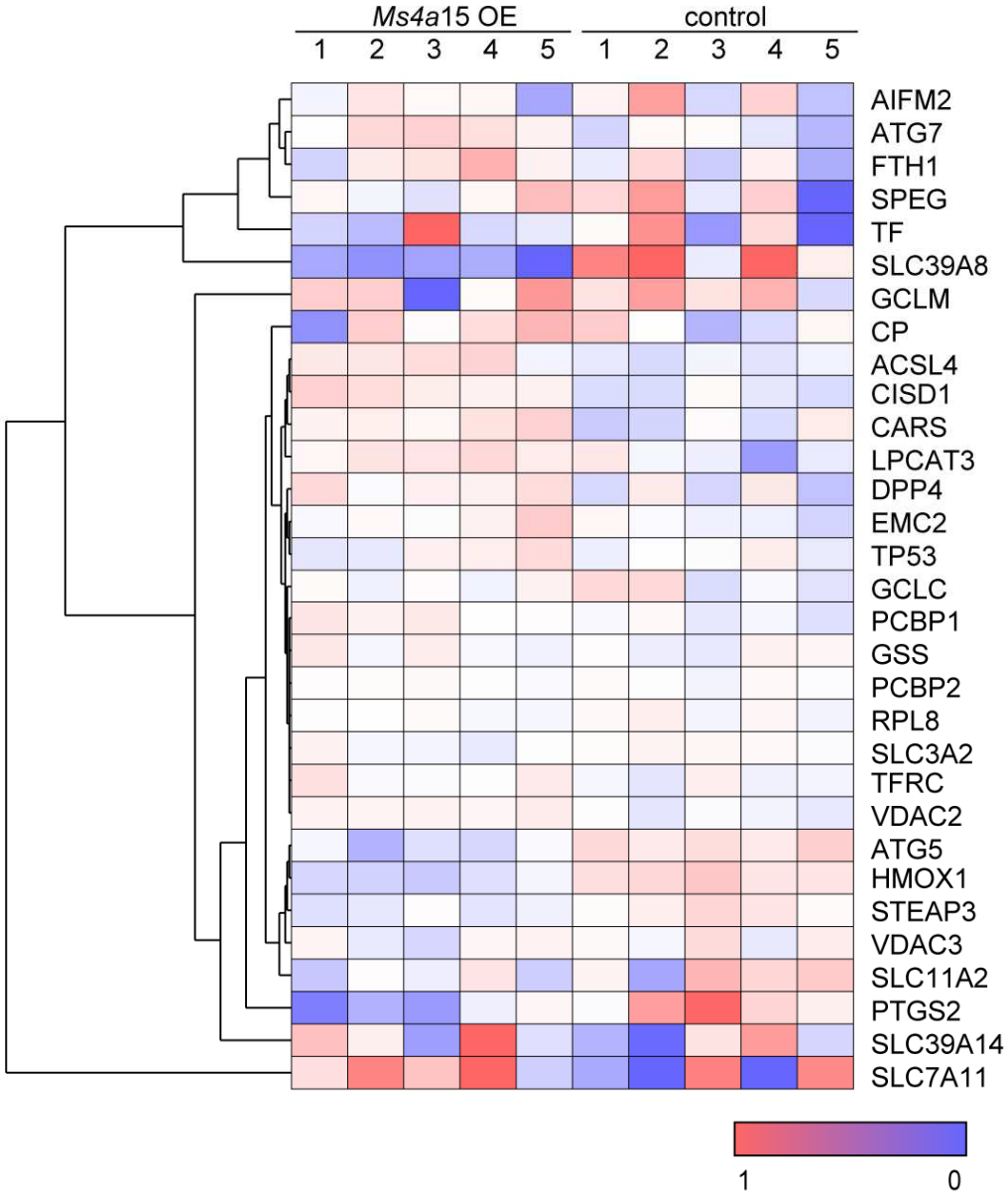

Figure 3.10 Heat map of the ferroptosis related proteins level in *Ms4a15* OE and the control cells. Heat map indicates protein change of *Ms4a15* OE compared to control cells from global proteomics data. The $\log_2$ of the normalized protein abundance ratios and $-\log_{10}$ of corresponding p-values of proteins quantified by at least two unique peptides were plotted. Expression data are shown as mean ± SD of n = 5 technical replicates.

3.3 Discussion

In this chapter, MS4A15 was unrevealed a novel mechanism in protecting against ferroptosis through constitutive depletion of ER Ca^{2+} stores to prevent lipid peroxidation. In normal cells, intracellular Ca^{2+} depletion can be stimulated either by RTK activates PLCγ or by GPCRs activate PLCβ to cleave PIP_2 into IP_3 and bound to IP_3R channel to span the ER membrane, ultimately allowing ER Ca^{2+} release. Indeed, expression of IP_3R1 was downregulated in *Ms4a15* OE cells as a result of calcium homeostasis disruption.

MS4A15 modulates receptor-mediated pathway via increasing phosphor ERK. Extracellular regulated kinases (ERK) pathway has been reported to have two sides effect. On one hand, researches showed that inhibition of RAS-ERK pathway by U0126 rescued erastin-induced ferroptosis (Yagoda et al., 2007). Blocking ERK pathway can prevent ferroptosis has been announced in U57810 and C2C12 cells. Specifically, augmented ferroptosis susceptibility was observed in engineered rhabdomyosarcoma cells exhibiting a higher growth rate driven by increased ERK pathway activation, linking ferroptosis susceptibility to cell motility (Codenotti et al., 2018). In fact, this coincides with our finding that *Ms4a15* overexpression suppressed cell migration, which resulted from the depletion of calcium. Because cell migration needs the calcium triggered from the stores then the actin can be mobilized and force protrusion, lacking of calcium cannot provide energy for the cells to migrate. Several proteins that are highly enriched in *Ms4a15* OE in the global proteomics analysis (i.e. WASP, SPN and SNX16) have been identified involved in actin reorganization and cell migration in vitro (Fawcett and Pawson, 2000). Recent research confirmed this finding, pointing that human cancer cells in a high mesenchymal state typically adopt synthesis of polyunsaturated lipids to migrate slowly, and are highly dependent on the enzymes protect against ferroptosis (Viswanathan et al., 2017; Wu et al., 2019).

On the other hand, some scientists claimed that JNK and p38, but not ERK, contribute to erastin-induced cell death in leukemia cells (Yu et al., 2015). Recently, the protective effect of ERK was discovered that panx1 deletion lead to the activation of MAPK/ERK signaling pathways and increased antioxidant gene HO1 expression, resulting in the inhibition of ferroptotic cell death during renal ischemia/reperfusion injury (Su et al., 2019). Glutamate-induced oxidative toxicity, which is known as oxytosis, shares common characteristics with ferroptosis. It has been reported that during oxytosis, ERK1/2 activation contributes to an adaptive response to oxidative stress of HT22 cells at initial phases when calcium efflux happens (Luo and DeFranco, 2006), indicating a protection role of calcium depletion. Consistently, in this work, control cells with 48h thapsigargin pretreatment showed protection against ferroptosis in line with reduced lipid peroxidation compared to cells with 3h

thapsigargin treatment, demonstrating lipids remodeling process might be activated during constitutive depletion of ER stores. Aberrant calcium homeostasis normally leads to ER stress and UPR activation, however, *Ms4a15* OE cells cause store depletion without activating UPR, suggesting that constitutive calcium homeostasis disruption rather than triggering UPR that is responsible for resistance.

ERK signal stimulation is one of the major effectors of GPCRs. GPCR was activated and stimulated Ca^{2+} release from internal stores when the cells were stimulated with bradykinin in calcium free medium. Ca^{2+} response to bradykinin stimulation of *Ms4a15* OE cells was strikingly reduced compared with control cells, suggesting less Ca^{2+} in the stores. The ATP-dependent SERCA pump, which transports calcium from the cytosol into the ER, is principally responsible for maintaining ER calcium homeostasis (Higgins et al., 2006). Indeed, overexpression of SERCA2 promoted calcium influx into the ER and re-sensitized *Ms4a15* OE cells to ferroptosis induction. Henke et al. have reported that $CoCl_2$, protect cells against erastin and RSL3 induced ferroptosis through reducing calcium influx (Henke et al., 2012). However, neither EDTA or $CoCl_2$ nor ionophore markedly affected ferroptosis sensitivity in this work, indicating acute Ca^{2+} flux and persistent Ca^{2+} dyshomeostasis are distinct cell death phenomena. These results suggest that although calcium homeostasis alteration is the crucial event of *Ms4a15* OE cells, there still be substantial differences in regulation of ferroptosis induced by individual compounds.

Taken together, persistent disruption of calcium homeostasis suppresses cell migration and inhibits cell proliferation, which associated with ferroptosis sensitivity; however, the mechanism needs to be further discovered.

Acknowledgement

I thank Susanne Pfeiffer for detecting calcium signal using FACS, Dr. Juliane Merl-Pham for performing proteomics using LC/MS, and Dr. Thomas Schwarzmayr for RNA sequencing analysis.

4. Constitutive calcium depletion drives lipids remodelling

4.1 Introduction

Previous results demonstrated that overexpression of *Ms4a15* resulted in disruption of calcium homeostasis, reduction of lipid peroxidation and retardation of cell migration. As reported, cancer cell migration and adhesion is a feature of calcium signaling (Berridge et al., 2000) which could be suppressed by PUFAs through remodeling of the fatty acid composition within the membranes (Tonutti et al., 2010). Accumulation of lipid peroxides is one of the hallmarks of ferroptosis, and bioinformatics analysis revealed a role of MS4A15 in arachidonic acid metabolism and ether lipids metabolism. However, neither lipids characteristics in *Ms4a15* OE cells nor the link between calcium depletion and reduced lipid peroxidation has been classified so far.

To systematically characterize the mechanisms of MS4A15, the metabolomic and lipidomic landscape were comparatively examined in this work. Metabolomics profiling has often been reported in the study of cell death, certain metabolites disorder, such as ATP, NADH, and NADPH, directly leads to cell death (Jain et al., 2012; Skouta et al., 2014; Yang et al., 2014a). Specially, as a subset of metabolomics, lipidomics is of great interests for quantitative measurement of lipids which play essential roles in ferroptosis.

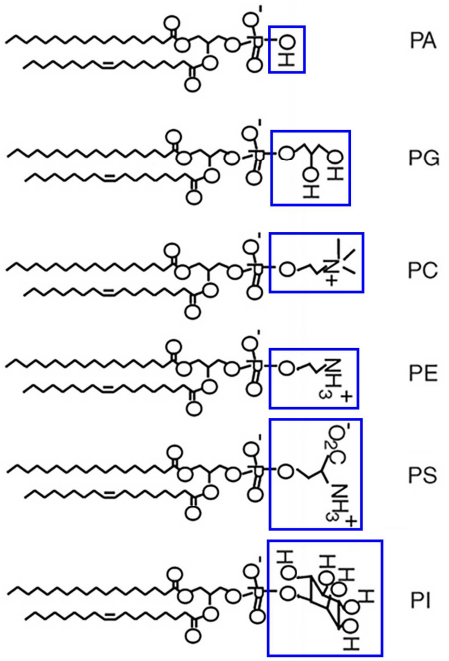

Figure 4.1 General structure of phospholipids and common head groups. GPs contain two fatty acids ester-linked to glycerol at C-1 and C-2, and a polar head group attached at C-3 via a phosphodiester bond. The fatty acids in GLs can vary in carbon group length and saturation degree.

PA, phosphatidic acid; PC, phosphatidylcholine; PE, phosphatidylethanolamine; PS, phosphatidylserine; PI, phosphatidylinositol.

Glycerophospholipids (GPs) are main components of cell membranes which comprise a glycerol backbone and a polar head group (Chilton and Murphy, 1986). The position of glycerol is numbered in a stereospecific manner (sn), so the phosphate group is located at the sn-3 position. Based on the polar head group attached to the phosphate, phospholipids can be classified into different classes: phosphatidylinositol (PI), phosphatidylcholine (PC), phosphatidylethanolamine (PE), phosphatidylserine (PS), and phosphatidic acid (PA) with no polar head (Figure 4.1).

According to the chemical bond of the fatty chain of glycerol on sn-1 position (i.e., acyl ester, ether and vinyl ether bond), phospholipids can be subdivided into diacyl, alkyl-acyl or alkenyl-acyl types. At the sn-2 position, where there is usually esterified an unsaturated fatty acid, the acyl chains are connected by an ester bond. Different combinations of head groups, the length and degree of unsaturation at the sn-1 and -2 yield different species of GPs (Yamashita et al., 2017). When cells undergo ferroptosis, oxidation in ER-associated compartments occurs on only PE species and is specific toward arachidonic acid (AA) and adrenaline (AdA) (Kagan et al., 2017). Hence, inhibition of AA or AdA esterification into PE could be a way to protect from ferroptosis.

The process of regulated cell death, including apoptosis and ferroptosis, can be initiated when certain proteins or pathways are activated. Therefore, pharmacological or genetic perturbations of proteins or pathways can alter the resultant cell death (Fuchs and Steller, 2011). Here, in line with the “omics” approaches, gene activation/silencing and chemical activation/inhibition were utilized to modify certain pathways to study the action of *Ms4a15* OE cells in response to different stimuli, to ultimately uncover the mechanisms of MS4A15 in mediating ferroptosis resistance.

4.2 Results

4.2.1 Lipid metabolites are reshaped in *Ms4a15* OE cells

In the omics’ cascade (i.e., DNA → RNA → proteins → metabolites), metabolites are the most downstream and thus considered to be the reflection of cellular metabolic processes. As a result, the global assessment of metabolites, metabolomics, has rapidly gained popularity in the study of cell death. Ferroptosis is executed by peroxidized membrane

phospholipids, particularly PEs that contain PUFA chains including AA (C20:4) and docosahexaenoic acid (DHA, C22:6). Here, metabolomics profiling assay was performed to capture metabolic changes of *Ms4a15* OE cells using electrospray Fourier transform ion cyclotron resonance mass spectrometry (ESI-FT/ICR-MS). The data was analyzed independently with two electrospray ionization (ESI) modes (ESI- and ESI+), which differ significantly due to the analytical sensitivity and technical variability. The m/z was annotated based on exact mass and mapped in Kyoto Encyclopedia of Genes and Genomes (KEGG), Human Metabolome Database (HMDB) and Lipid maps databases (Figure 4.2A). To gain insight into the metabolic mechanism of MS4A15, metabolic pathways of the significantly altered metabolites were analyzed by searching HMDB (Figure 4.2B). Volcano plots and principal component analysis (PCA) of the ESI-/+ generated data are shown in Figure 4.3, a list of lipids and metabolites were annotated as dramatically differentially expressed between *Ms4a15* OE and control cells ($p<0.05$).

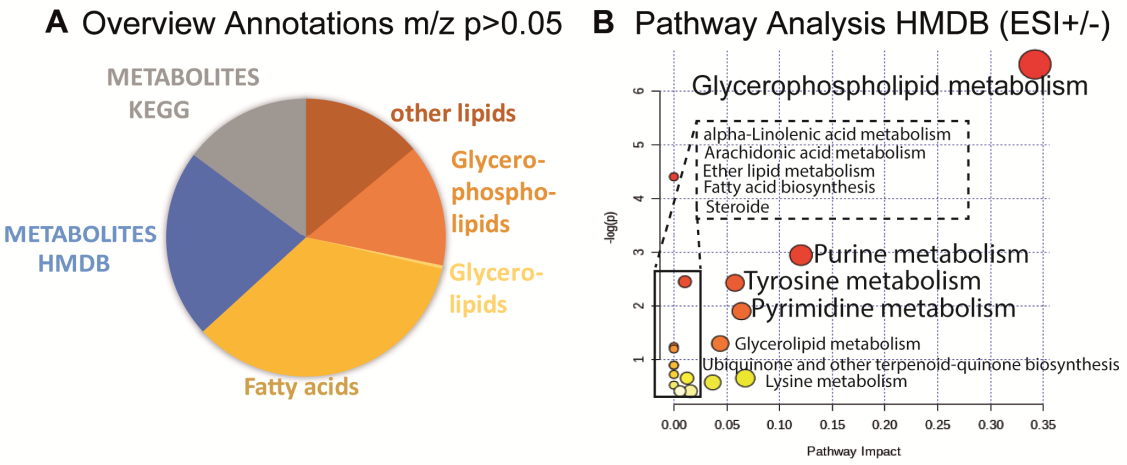

Figure 4.2 Summary of metabolites biological processes. Overview of annotations of metabolites (A) and pathway analysis module indicates the pathways most involved (B).

As PUFAs are easily oxidized, decreasing PUFA content helps the cells to be less vulnerable to ferroptosis inducers. In general, the *Ms4a15* OE cells have more SFA and MUFA as well as less PUFA compared with control, indicating a protection role. Indeed, the ESI- data showed an increase of free/saturated fatty acids of *Ms4a15* OE, such as Myristoleic acid (C14H26O2), an omega-5 fatty acid; PI(18:0/18:2, C45H83O13P); PE(22:5(4Z,7Z,10Z,13Z,16Z)/18:0, C45H80NO8P) and the ester of pyrophosphoric acid, uridine diphosphate (UDP, C9H14N2O12P2). The downregulated lipids and metabolites in the ESI- data including PE(O-16:0/0:0, C21H46NO6P), PI(18:0/20:4(8Z,11Z,14Z,17Z), C47H83O13P) PC(O-15:0/0:0,C23H50NO6P), Lysophosphatidic acid(LPA, 18:0/0:0,

C21H43O7P), LPA(P-16:0, C19H39O6P), and adenosine monophosphate (AMP, C10H14N5O7P), an ester of phosphoric acid that binds to AMPK and leads to the activation of a cascade of cellular metabolic processes (Figure 4.3A).

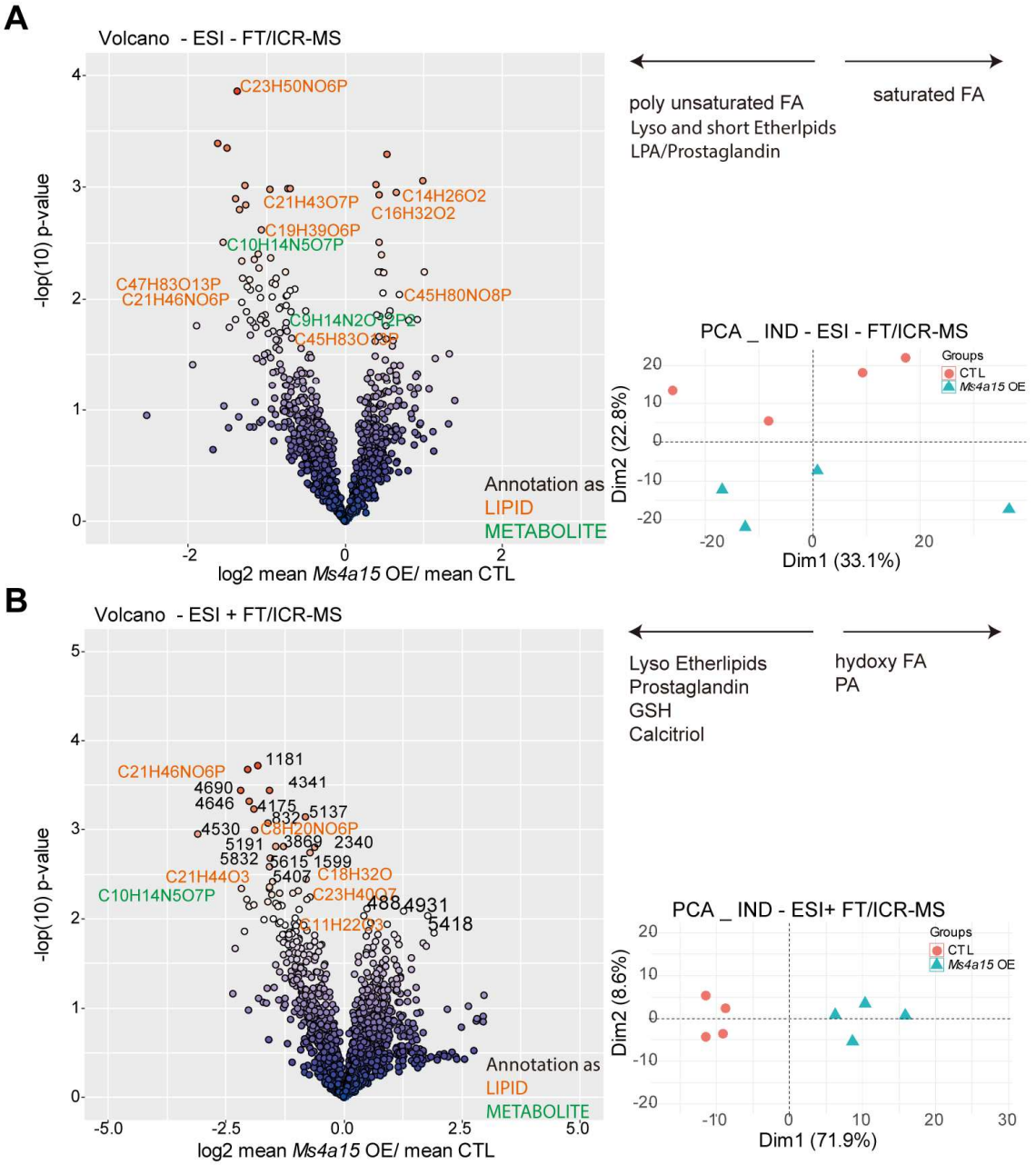

Figure 4.3 Metabolomis analysis acquired by ESI-FT/ICR-MS. Volcano plots and respective unsupervised PCA of *Ms4a15* OE and control samples in ESI- (A) and in ESI+ (B) modes. Volcano plots show log_2 fold change of the MS4A/CTL mean ratios plotted against $–log_{10}$ of adjusted p values, red dots represent lipids, and blue dots represent metabolites. In PCA plots, red dots represent control samples; blue triangles represent *Ms4a15* OE samples.

In addition to the increase of hydroxyl fatty acid, the ESI+ data showed a list of lipids which were significantly downregulated in *Ms4a15* OE cells (Figure 4.3B). For example, calcitriol (C27H44O3), the active form of vitamin D being used for taking up calcium into the cells. SLC7A11 expression level shown in the heat map of the known ferroptosis related proteins was slightly increased (Figure 3.10), metabolomics analysis showed however that the calcitriol-dependent antioxidant GSH reduction was observed in *Ms4a15* OE cells, demonstrating that the protection role of MS4A15 is through a novel mechanism whereas not depend on GSH/GPX4 pathways. Other highly downregulated metabolites include a branch of short- and lyso- ether lipids, e.g., PI(22:4(10Z,13Z,16Z,19Z) /16:0, C47H83O13P) which consists of one chain of palmitic acid (C16:0) at the C-1 position and one chain of (10Z,13Z,16Z,19Z-docosatetraenoyl) at the C-2 position; C45H81O13P that consists of one chain of palmitic acid at the C-1 position and one chain of mead acid at the C-2 position; while PC(15:0/P-16:0, C39H78NO7P) consists of one chain of pentadecanoic acid (C15:0) at the C-1 position and one chain of plasmalogen 16:0 at the C-2 position; LysoPE(0:0/22:6(4Z,7Z,10Z,13Z, 16Z,19Z), C27H44NO7P) has a free alcohol in either the sn-1 or sn-2. These metabolic analyses indicate that MS4A15 may play an independent role in alterations of lipids structure through mediating calcium signaling.

In some cases, the extensive usage of metabolites within well studied pathways, such as amino acid metabolism and lipid metabolism, rather than a particular metabolite, is of greater importance. Previously, targeted deletion of the luminal Ca^{2+} buffering protein Calreticulin was shown to drastically alter lipid homeostasis in mice (Guo et al., 2002). Since MS4A15 informatics revealed a role in arachidonic acid metabolism and ether lipids metabolism (Figure 2.6A), further investigation has been conducted to understand how Ca^{2+} homeostasis disruption in *Ms4a15* OE cells directly impacts cellular lipid composition and metabolism. An untargeted mass spectrometry-based lipidomics analysis was performed on *Ms4a15* OE cells treated with RSL3/DMSO for 3 hours, and parental control cells which were incubating with thapsigargin (3 or 16 hours) before being treated with RSL3/DMSO for 3 hours.

There were more than 4600 individual lipid species have been detected. The Non-targeted cluster analysis demonstrated that *Ms4a15* OE and 16h thapsigargin-treated control cells (Tgn^{long}) have similar lipids profile in both ESI+ and ESI- modes, whereas control cells were clustered together with 3h thapsigargin-treated control samples (Tgn^{short}) (Figure 4.4A). Similarly, an unsupervised principal component analysis (PCA) delivered a clear separation of *Ms4a15* OE and Tgn^{long} treatment from control and Tgn^{short} in the second component (PC1=33.1%, PC2=15.2%), which was showed in the heat map that the relative abundances of several lipid species were altered significantly of *Ms4a15* OE and Tgn^{long} in response to calcium depletion (Figure 4.4B). Retention time and detected masses were used to annotate

the species and categorize them in the LIPID classification system. The pie chart gives us an insight of the important lipids categories which were decreased or increased in *Ms4a15* OE and Tgn^{long} that displayed in the heat map (i), those exclusive to *Ms4a15* OE (ii), and shared in *Ms4a15* OE and Tgn^{long} (iii). The majority of modulated lipids are gylcerophospholipids, followed by several fatty acid species (Figure 4.4C).

Generally, PUFA lipids are the driven factors of ferroptosis which have strong sensitization. Indeed, Ca^{2+} depletion of *Ms4a15* OE and Tgn^{long} cells cause a significant increase ($p < 0.05$, two sided Welch-test) of the main saturated fatty acids (palmitic (C16:0), stearic (C18:0)), and MUFAs (gondoic (C20:1), erucic acid (22:1)) (Figure 4.4D). Also, a dramatic decrease of the PUFA lipids are observed, such as alpha-linolenic acid (ALA, the essential omega-3 fatty acids) derivatives eicosapentaenoic acid (EPA, C20:5), doasapentaenoic acid (DPA, C22:5n-3) and doxosahexaenoic acid (DHA, C22:6), which support lipid peroxidation and can change the fatty acid composition of the membranes (Figure 4.4D). There was about 39% of the total cellular lipid content has been reshaped in total, suggesting the crucial role of calcium depletion in lipid remodeling.

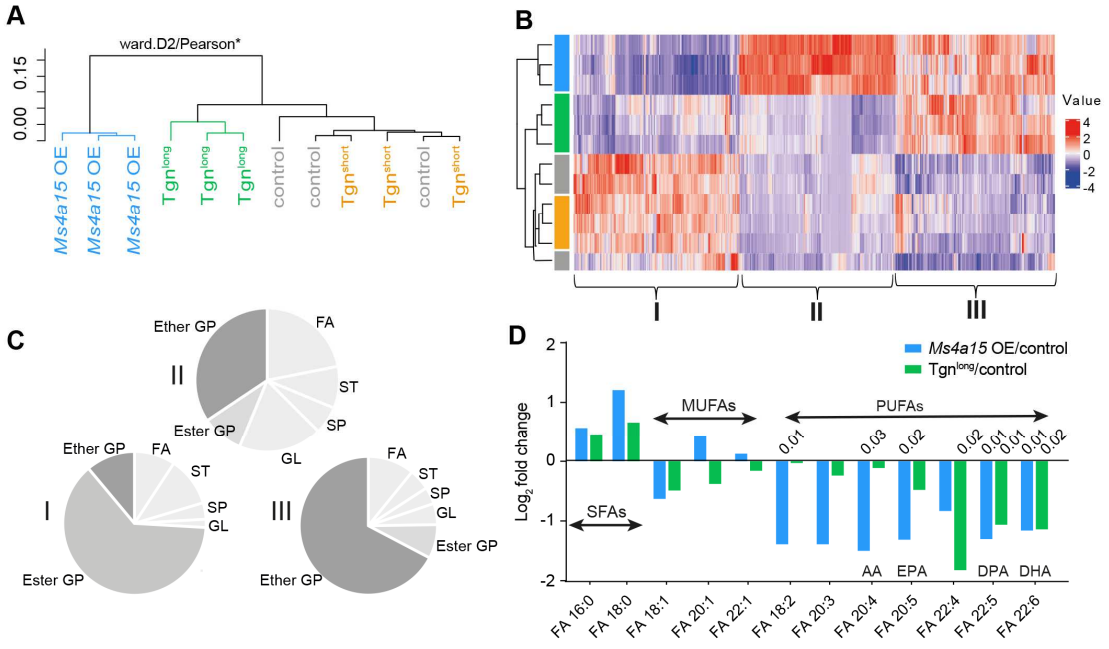

Figure 4.4 Untargeted lipidomics reveals calcium depleted cells protect from ferroptosis through changes of specific lipids. (A) Non-targeted cluster analysis (wardD2) of *Ms4a15* OE and parental control cells with treatment as indicated. (B) Heat map (one-way ANOVA; FDR-corrected p-value <0.05) showing changes in lipid profile. The relative abundance of lipid is color-coded from red indicating high signal intensity to dark blue indicating low intensity and clustered using Pearson correlations. (C) Pie diagram shows the categories of the alteration of lipids abundant of *Ms4a15* OE/Tgn^{long} compared to control / Tgn^{short} corresponding to the groups in (B). GP, glycerophospholipid; FA, Fatty acid; ST, Sterol Lipid; SP, Sphingolipid; GL, glycerolipid. (D) Fold change of free fatty acids of *Ms4a15* OE/Tgn^{long} compared to control / Tgn^{short}. $p < 0.05$, two sided Welch-test.

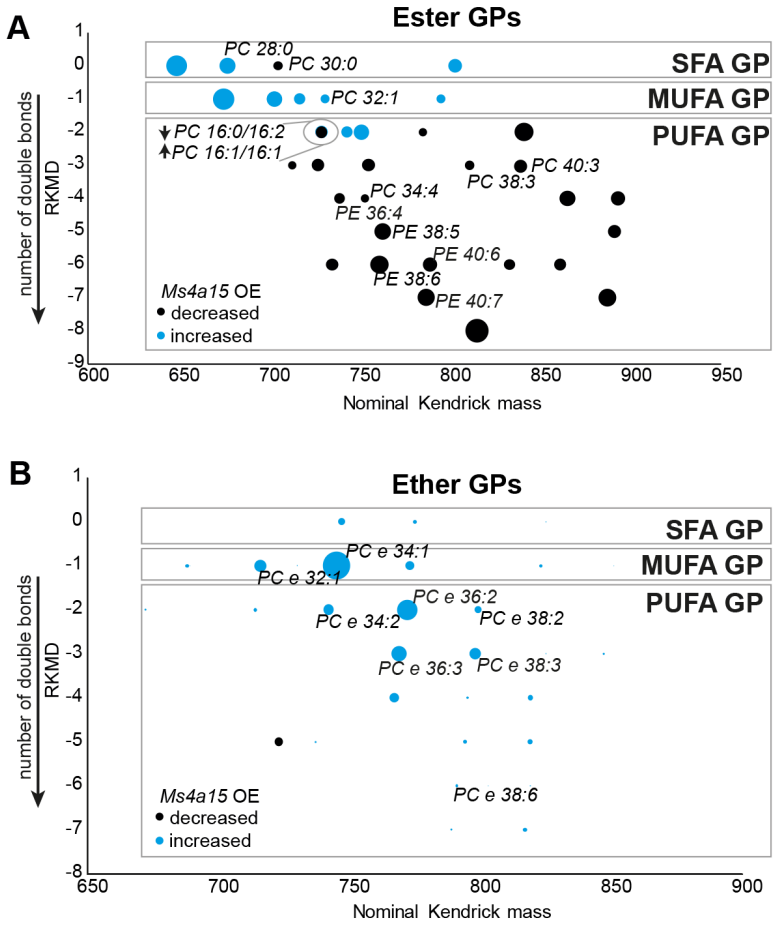

Figure 4.5 Significantly modified ester and ether glycerophospholipids in *Ms4a15* OE. GP, glycerophospholipid; SFA GP, saturated phospholipid; MUFA GP, monounsaturated phospholipid; PUFA GP, polyunsaturated phospholipid

To better explore the role of MS4A15 in lipids remodeling, the Kendrick mass defect plot was applied as a helpful tool to reveal homologous series of various lipid classes. Therefore, the most significantly changed ester lipid species detected in *Ms4a15* OE were transformed into the Kendrick scale. In line with the metabolomics analysis (Figure 4.3), the plots illustrate a dramatic increase in saturated GPs and MUFA GPs. In contrast, PUFA GPs are downregulated in *Ms4a15* OE (Figure 4.5 A). Along with the distinct transformation to mono- and saturated species, the Kendrick plot showed a decrease in higher molecular weight PUFA GPs. Importantly, *Ms4a15* OE displayed a dramatic increase in ether lipids abundance (Figure 4.5 B). Consequently, *Ms4a15* OE reveals a decrease in number of double bonds and in chain length of ester lipids, suggesting the elongation and desaturation are inhibited.
Notably, the increased GPs in ferroptosis-resistant models are almost exclusively ether lipids, compared with the decreased ester lipids in ferroptosis-sensitive models (Figure 4.6A). Among the ether lipids detected, which have been confirmed to be vinyl-ether lipids

(plasmalogens) by acidic hydrolysis, glycerophosphocholines (PCs) and glycerophosphoethanolamins (PEs) are two predominant lipid groups (Figure 4.6B) PCs and PEs are two major types of plasmalogens, i.e. ethanolamine plasmalogens (PlsEtns) and choline plasmalogens (PlsChos) that have been reported to function as endogenous antioxidants against lipid peroxidation (Brites et al., 2004). PlsEtns and PlsChos are occupied by C16:0 (palmitic acid), C18:0 (stearic acid) or C18:1 (oleic acid) carbon chains at the sn-1 position, and normally contain a polyunsaturated fatty acid at sn-2 position, specifically AA or DHA (Figure 4.7). Further analysis showed consistently increased amount of PCs and PEs in *Ms4a15* OE/Tgn^{long} (Figure 4.6C). The abundance of other GPs were detected, including phsphoinositols (PIs), phosphoserins (PSs) and GPs which were changed according to the length and saturation degree. This is in particular the case for higher molecular weight and unsaturated species with a strong trend from ester- to ether-type sn-1 bonds. For example, PA(O-36:4), PA(O-36:3), PS(42:6) and PS(42:7) were markedly decreased in *Ms4a15* OE cells, and primarily saturated or monounsaturated C16, C18 and C20-containing species were increased, e.g. PI(26:0), PI(O-26:1), PI(O-28:0), PS(28:1), PA(O-36:1) (Figure 4.6D). Overall, *Ms4a15* OE/ Tgn^{long} cells showed increased amount of SFA- and MFUA- containing GPs as well as decreased PUFA containing GPs (Figure 4.5A).

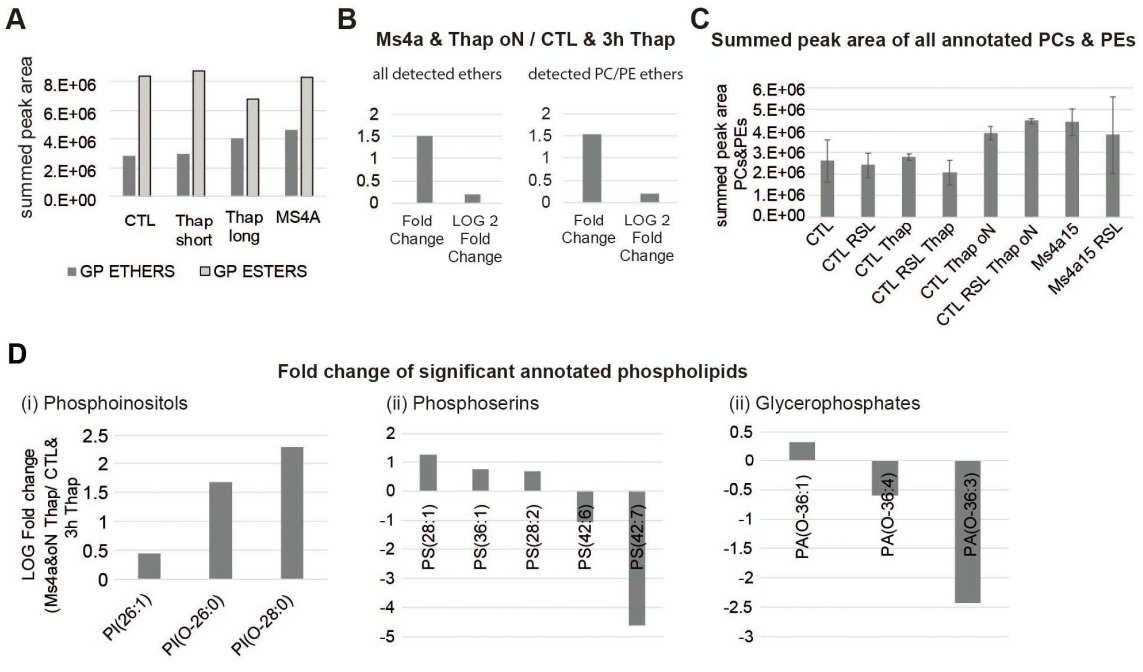

Figure 4.6 Untargeted lipidomics reveals lipids change of calcium depleted cells. (A) Abundance of ether and ester lipids changed in samples detected. (B) All detected ethers are mainly PC/PE ethers. (C) Summed peak area of all annotated PC and PE lipids all samples. (D-E) The RKMD plots reveal homologous series of PEs/PCs (D) and ether PEs/PCs (E). (F) Fold change of

phosphoinositols, phosphoserins and glycerophosphates in *Ms4a15* OE/Tgn^{long} compared with control/Tgn^{short}.

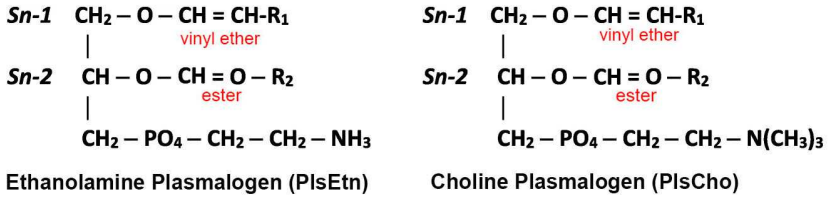

Figure 4.7 Chemical structures of Plasmalogens. R1 = saturated fatty acid (SFA), monounsaturated fatty acid (MUFA). R2 = polyunsaturated fatty acid (PUFA).

Consequently, persistent disruption of calcium homeostasis favors lipids remodeling which serves as the protective mechanism against oxidative stress of cells. In fact, lipids significantly degraded in *Ms4a15* OE cells are mainly C40H76NO8P (PC(18:2(9Z,12Z)/14:0)), which is a tetradecanoate ester PUFA; DAG, the analogue of phorbol esters that mostly found in lipid droplets; one species of ether lipids C37H71O7P (PA(P-18:0/16:1(9Z))); and 2-Hydroxypropyl stearate (C21H42O3) (Figure 4.8). Ester PUFA lipids and their analogues are the major targets of RSL3, leading to the burst of lipid peroxides.

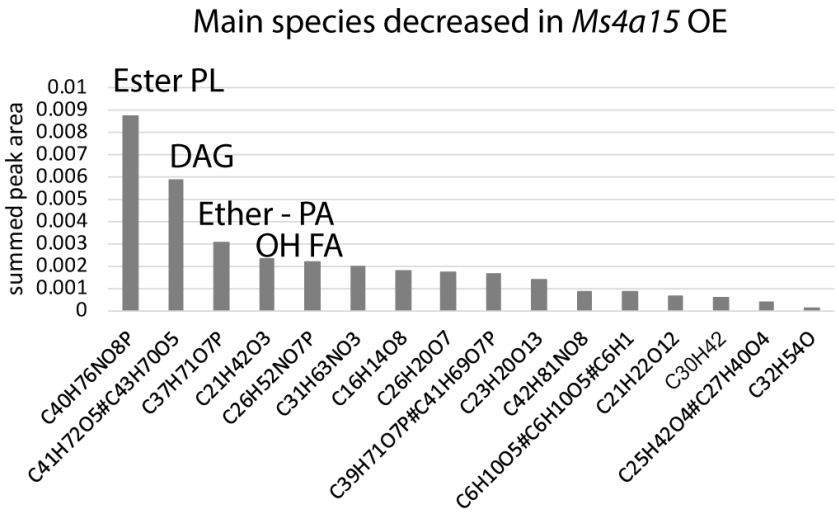

Figure 4.8 Lipid species decreased in *Ms4a15* OE.

In contrast, the lipids dramatically increased in *Ms4a15* OE cells are mainly MUFAs, SFAs and plasmalogens (Figure 4.9A), such as C40H78NO8P (PE(15:0/20:1(11Z))) that consists of SFA pentadecanoic acid at the C-1 position and MUFA eicosenoic acid at the C-2 position, and C42H84NO7P (PC(18:0/P-16:0)) that consists of SFA stearic acid at the C-1 position and plasmalogen 16:0 at the C-2 position. These MUFAs and plasmalogens which act as antioxidants were strongly depleted to protect cells from lipid peroxidation after RSL3

treatment in *Ms4a15* OE cells, however, remained unchanged in control cells (Figure 4.9B). These results indicate that phospholipids with one monounsaturated fatty acyl chain or one plasmalogen chain are easier attacked by ferroptotic ROS and depletion of MUFAs or plasmalogens does not drive cells undergo ferroptosis. Conclusively, MS4A15 promotes lipid remodeling through mediating calcium signaling and ultimately regulates ferroptosis resistance.

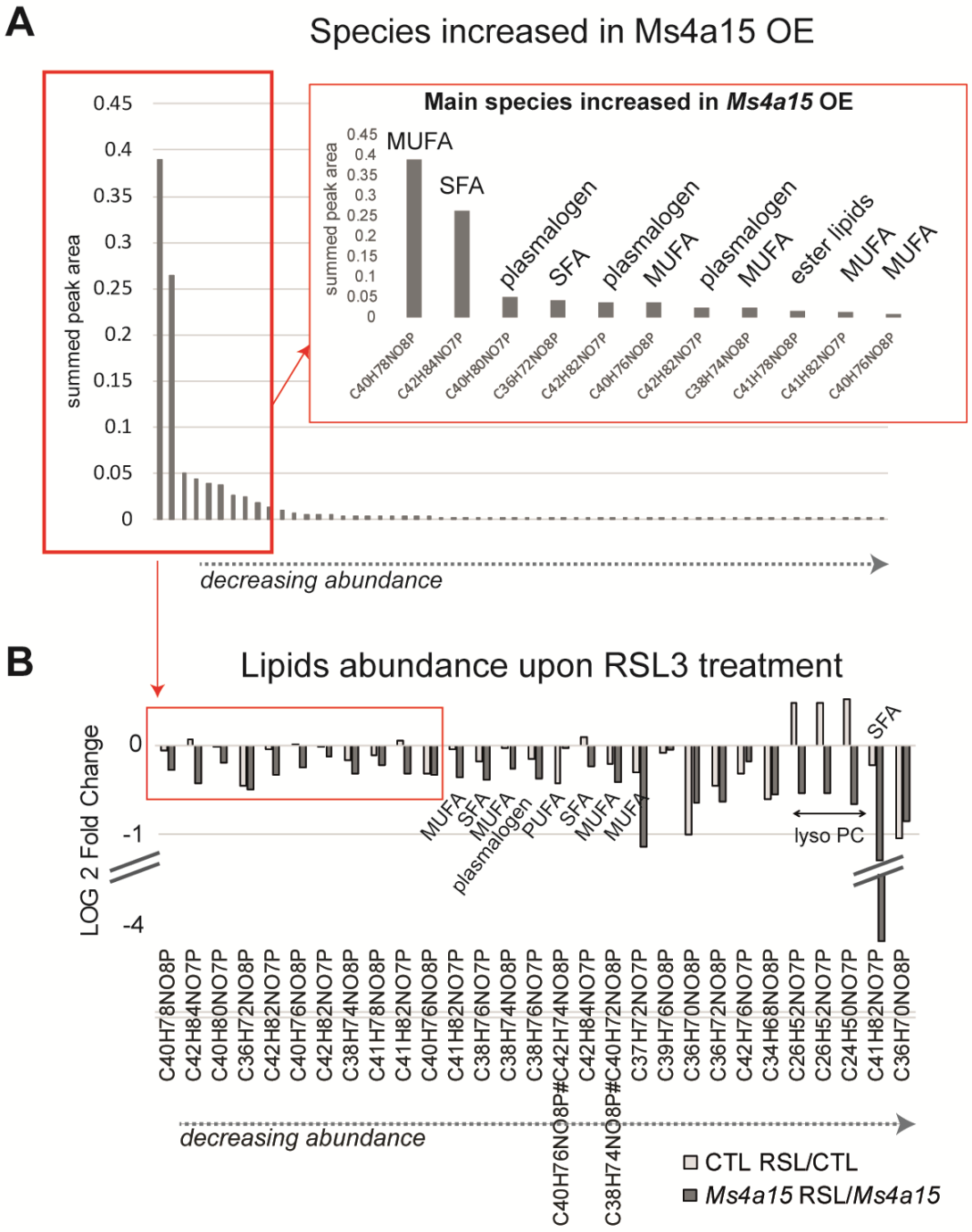

Figure 4.9 lipids profile in *Ms4a15* OE. (A) Lipid species increased in *Ms4a15* OE. All of these are putative PE- or PC- glycerophopholipids, NO7Ps indicate ether lipids and NO8Ps indicate ester lipids. (B) Change of lipids abundance upon RSL3 treatment in *Ms4a15* OE and control.

PUFA lipid arachidonic acid (AA) is the key driver that stimulates ferroptosis execution, since lipid peroxides mainly derive from AA. Lipidomics analysis suggested that *Ms4a15* OE and Tgn^{long} cells caused a dramatic decrease of free AA (Figure 4.10A). Consistent with these lipids profile, RNA sequencing data suggested that *Ms4a15* OE cells display upregulation of cyclooxygenase-1 (*Cox-1*; *Ms4a15*/Parental Log_2= 4.39; *p*(adj)= 0.0), which produces prostaglandins from enzymatically converting AA, suggesting reduction of AA. Additionally, calcium-dependent Phospholipase A2 (*Pla2g1b*, EC 3.1.14); Log_2=5.36; p(adj)= 0.00093), which releases AA from membrane GPs, has been also strongly upregulated in *Ms4a15* OE, hinting that AA production was limited (Figure 4.10B).

In conclusion, these data suggested that the lipids profiling has been significantly altered in *Ms4a15* OE and Tgn^{long} cells through depleting store Ca^{2+} and blocking Ca^{2+} uptake. Briefly, MS4A15 showed a protection role through reshaping the lipid structure within cell membranes, leading to increased MUFAs and ether lipids as RSL3 targets but decreased PUFAs. However, the mechanism of calcium homeostasis perturbation in affecting lipids remodeling needs to be further discovered.

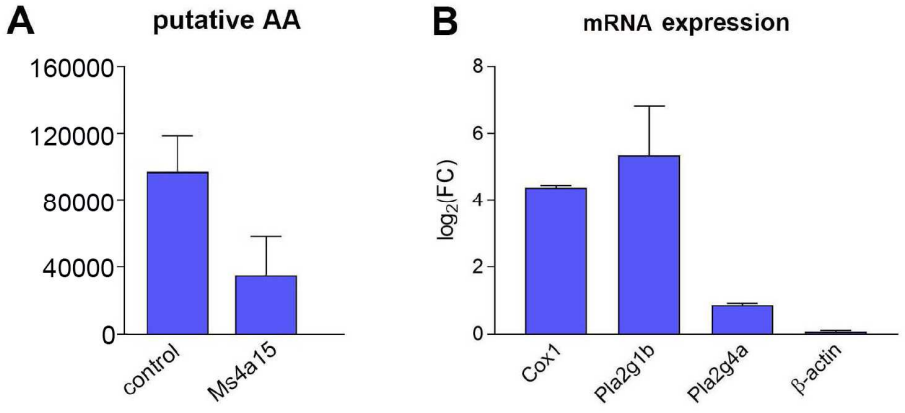

Figure 4.10 Arachidonic acid level is limited in *Ms4a15* OE cells. (A) Free AA content in *Ms4a15* OE and control cells. Putative AA content are shown as mean ± SD of n = 5 technical replicates. (B) Fold change of mRNA expression levels of *Cox1*, *Pla2g1b* and *Pla2g4a* in *Ms4a15* OE compared with control cells. β-actin was used as internal control. Expression data are shown as mean ± SD of n = 5 technical replicates.

4.2.2 DPA and DHA are the key drivers of ferroptosis sensitivity

Lipid peroxidation and ferroptosis is specifically driven by PUFA lipids, the lipid profile showed marked downregulation of highly unsaturated fatty lipids in *Ms4a15* OE and Tgn^{long} treated cells; while upregulation of ether lipids and MUFAs have been observed. Ether-linked lipids, especially plasmalogens, have been reported to function as endogenous antioxidants against lipid peroxidation. Two complementary approaches were carried out to modify lipids metabolism and to examine the effects of these lipids on ferroptosis sensitivity. If the control cells supplemented with certain plasmalogens in the culture media become more resistant to ferroptosis or the *Ms4a15* OE supplemented with specific PUFA lipids are sensitized, then modification of these lipids can regulate ferroptosis sensitivity. The cells were pretreated with indicated compounds for 48 h before ferroptosis induction.

Due to the dramatic decrease of DPA, DHA and EPA in *Ms4a15* OE cells (Figure 4.4B), exogenous DPA, DHA and EPA were used for supplementation with *Ms4a15* OE cells which resulted in susceptibility to ferroptosis in a dose-dependent manner (Figure **4.11**). There were more than 60 species plasmalogens were increased in *Ms4a15* OE, however, control cells supplemented with the antioxidants plasmalogens (C18(Plasm)-22:6 PE, C18(Plasm)-18:1 PC and C18(Plasm)-20:4) in the culture medium did not prevent ferroptosis (Figure 4.12).

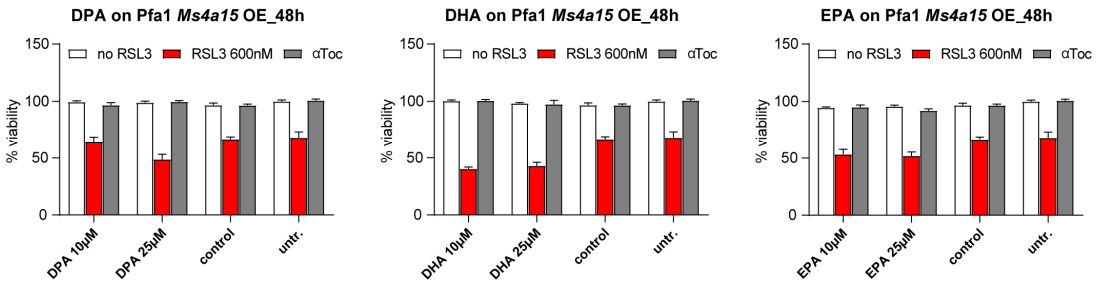

Figure 4.11 Addition of PUFAs sensitizes *Ms4a15* OE cells from ferroptosis. Survival of *Ms4a15* OE cells pretreated with DPA, DHA and EPA species at concentrations indicated in figures for 48h. Ferroptosis induced with 500 nM RSL3 with 10 μM αToc rescue. Viability data are plotted as mean ± SD of n = 3 technical replicates of at least three repetitions of the experiment with similar outcomes.

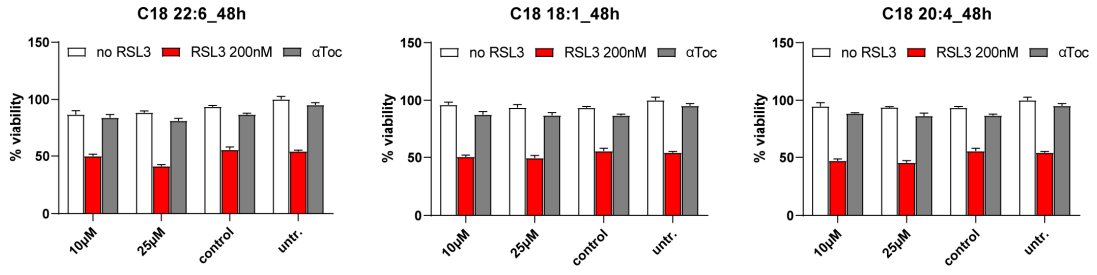

Figure 4.12 Addition of plasmagens does not protect control cells from ferroptosis. Survival of control cells pretreated with C18(Plasm)-22:6 PE, C18(Plasm)-18:1 PC and C18(Plasm)-20:4 PE at concentrations indicated in figures for 48h. Ferroptosis induced with 200 nM RSL3 with 10 μM αToc

rescue. Viability data are plotted as mean ± SD of n = 3 technical replicates of at least three repetitions of the experiment with similar outcomes.

To validate this result, RNAseq and proteomics data were applied to check the expression levels of plasmalogen biosynthesis enzymes. Fatty acyl reductase (FAR1) is the rate-limiting enzyme of plasmalogen synthesis which located in the outer peroxisomal membrane (Honsho et al., 2010). Glyceronephosphate O-acyltransferase (GNPAT) catalyzes the first step of plasmalogen biosynthesis and followed by the exchange of the acyl group for an alkyl group by alkyl-glycerone phosphate synthase (AGPS) (Biermann et al., 1999; Brown and Snyder, 1982). Consistent with the result that addition of exogenous plasmalogen failed to protect control cells, the mRNA and protein expression levels of *Far1*, *Agps*, *Gnpat*, are relatively unchanged (Figure 4.13A). Consistently, knockdown of *Gnpat* of either *Ms4a15* OE or control cells to inhibit the biosynthesis has no impact on ferroptosis sensitivity , indicating plasmalogens may not be the key factors to prevent ferroptosis (Figure 4.14). To uncover if MS4A15 participates in the process of plasmalogen biosynthesis, the colocalization of MS4A15 with peroxisome marker Catalase was performed, because the first step of plasmalogen biosynthesis is in peroxisome, however no overlap was observed (Figure 4.13B), suggesting that MS4A15 is not involved in the plasmalogen biosynthesis process directely.

Taken together, these results indicating that certain PUFA lipids, i.e. DHA, DPA and EPA, may form critical mass of lipid peroxides required for executing ferroptosis, but plasmalogens may not be the essential regulator for ferroptosis resistance. More analysis needs to be done to provide evidences for calcium alteration affecting lipids reshaping.

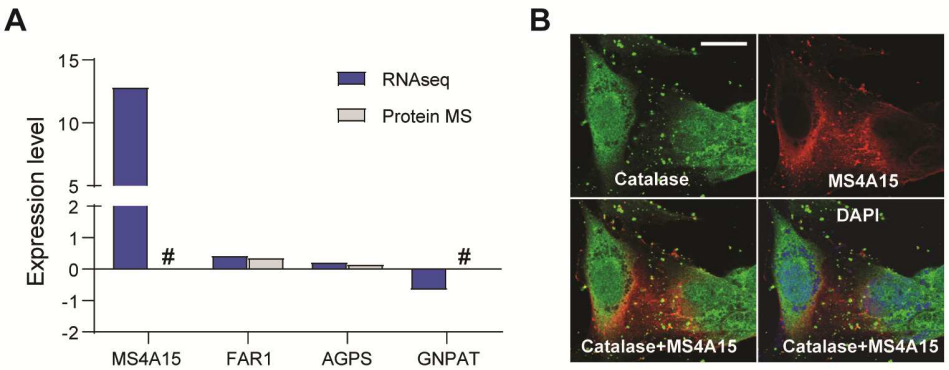

Figure 4.13 MS4A15 does not affect plasmalogen biosynthesis directly. (A) Expression levels of genes/proteins in plasmalogen biosynthesis. (B) Co-localization of MS4A15 and Catalase. Data are shown as mean ± SD of n = 5 technical replicates. Scale bar, 20 µm.

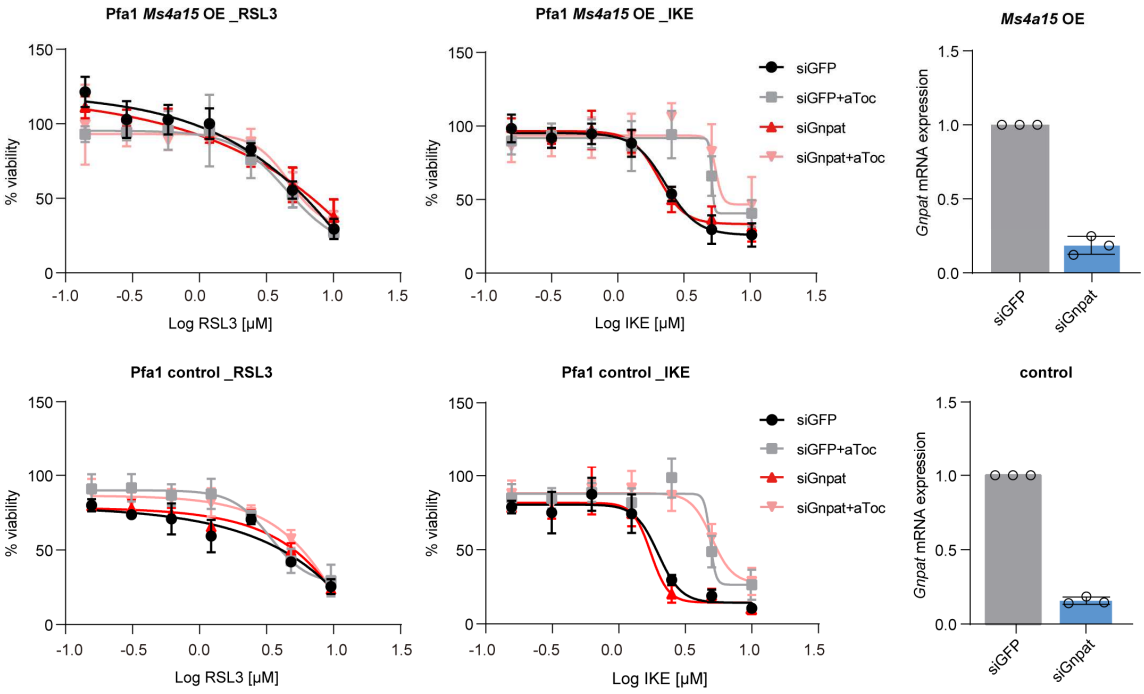

Figure 4.14 Knockdown of siGnpat does not affect ferroptosis sensitivity. (A-B) Viability of siRNA knockdown of *Gnpat* (siGnpat) compared to control (siGFP) in *MS4a15* OE cells (A) and parent control (B) treated with RSL3 (left) and IKE (right) with the concentration indicated in the figure. mRNA expression levels of *Gnpat* confirms the knockdown efficiency. Expression data are shown as mean ± SD of n = 3 technical replicates. Viability is shown as mean ± SD of n = 3 technical replicates.

4.2.3 Global calcium genes define a signature for ferroptosis sensitivity

Strict control and regulation of calcium signaling is essential for appropriate cellular function, which was confirmed by the role of calcium perturbation during cell proliferation, gene transcription and cell death (Berridge et al., 2003; Berridge et al., 2000; Parkash and Asotra, 2010). Increasing reports have indicated that altered calcium influx/efflux is associated with some cancers and can be applied in cancer therapy through inhibiting EMT (Stewart et al., 2015), yet, the mechanisms are not completely understood. Global survey for the function of calcium homeostasis in ferroptosis resistance through data mining from the CTRP database was performed, and the top 100 RSL3-resistant/sensitive cancer cell lines in the CTRP database were analyzed for CCLE KEGG calcium signaling gene expression using Cancer Cell Line Encyclopedia (CCLE) expression data.

From the unbiased hierarchical cluster heat map, clear separations of these cell lines in line with their ferroptosis sensitivity have been observed. Several clusters were associated with ferroptosis sensitivity. one of the clusters upregulates Calcium Voltage-Gated Channel Subunits (*CACNA 1A/1B/1G/1F/1E/1I*), Calcium/Calmodulin Dependent Protein Kinase II

Beta (*CMK2B*), Plasma Membrane Calcium Pumps (*ATP2B2/3*), and Nitric oxide synthases (*NOS1/2*), to drive the susceptibility to ferroptosis. The other clusters clearly downregulated in sensitive cell lines including histamine receptor Histamine Receptor H1 (*HRH1*), Troponin C1 (*TNNC1*), *NOS3* and PLC subtypes E1/B1/B4; in particular a cluster containing *EGFR*, *ERBB2/3* (*HER2/3*), *ITPR3* (IP3 receptor 3) and *GNAQ* (the Gq alpha subunit coupled to activation of PLC-beta and IP3 release) (Figure 4.15).

The resistant cell lines, in contrast, formed smaller unique clusters, possibly reflecting single gene contribution to resistance. Upregulation of Adrenoceptor Beta 2 (*ADRB2*), Platelet Activating Factor Receptor (*PTAFR*), and Purinergic Receptor P2X (*P2RX6/7*) or downregulation of Bradykinin B Receptors (*BDKRB1/2*), Ryanodine Receptor 1 (*RYR1*), are crucial factors in resistance. One prominent but nonexclusive cluster in the resistant cell lines downregulates Cyclic ADP-Ribose Hydrolase (*CD38*), *P2RX1* and cGMP phosphohydrolyase (*PDE1B*). Intriguingly, several RSL3-sensitive lines also display this downregulated cluster and lack the *EGFR*/*ERBB* cluster, but upregulate the *ATP2B*/*CACNA*/*CAM2K* cluster. This would appear to have the effect of neutralizing the *CD38*/*P2RX1*/*PDE1B* cluster (Figure 4.15).

Consistently, PCA analysis identified a distinct separation of resistant (red) and sensitive (green) cell lines based on the scores of PC1 (22.6%) and PC2 (8.3%) (Figure 4.16). In the RSL3 resistant group, *EGFR*, *ERBB2/3*, *ASPH*, *ADRB2* and *PLCD3* were the key drivers, while *ATP2A3*, *CD38*, *P2Rx5*, *PLCG2* and *ADORA2A* were the main factors in the RSL3 sensitive group, which is convincing because overexpression of *ATP2A2* sensitized *Ms4a15* OE cells. The *GNAQ*, *SPHK1* and *PLCB4* are noteworthy as they show where resistant and sensitive cell lines grouping together. These results suggested that manipulation of calcium homeostasis could provoke sensitivity.

Through identification of calcium homeostasis involvement in ferroptosis, a mechanism has been elucidated that allows us to realize a polygenic signature for identification and targeted sensitization for individual lines. These results suggested manipulation of this pathway could provoke sensitivity, therefore providing a new strategy to reverse the resistance of cancer drug therapy.

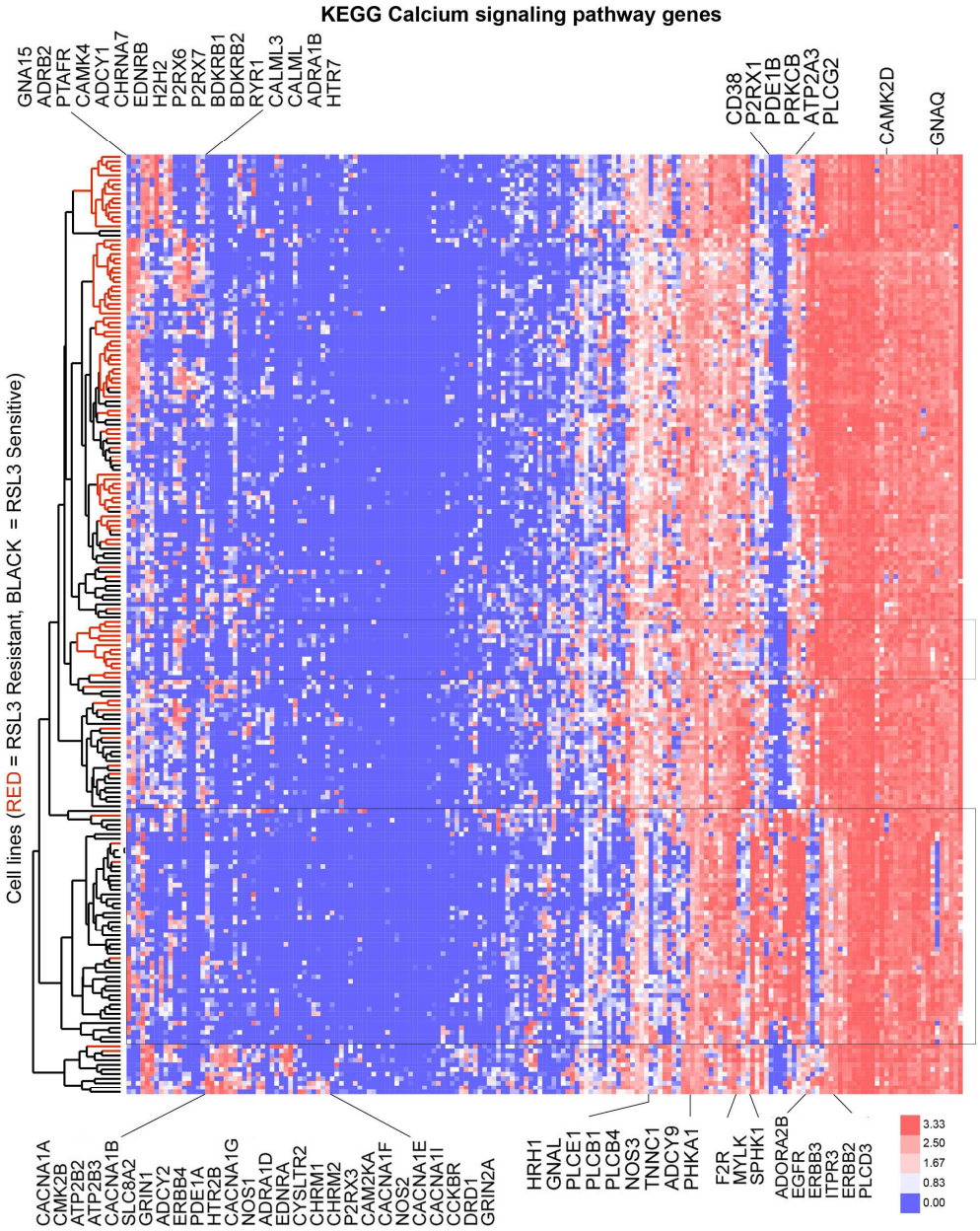

Figure 4.15 Unsupervised hierarchical cluster of genes in RSL3-resistent/sensitive cell lines. Each column represents normalized gene expression of genes in the KEGG_CALCIUM pathway. Each row represents the different cell lines separated by their sensitivity to RSL3 induced ferroptosis. Red, RSL3 resistant; Black, RSL3 sensitive. The relative abundance of lipid is color-coded from red indicating high signal intensity to dark blue indicating low intensity and clustered using Pearson correlations

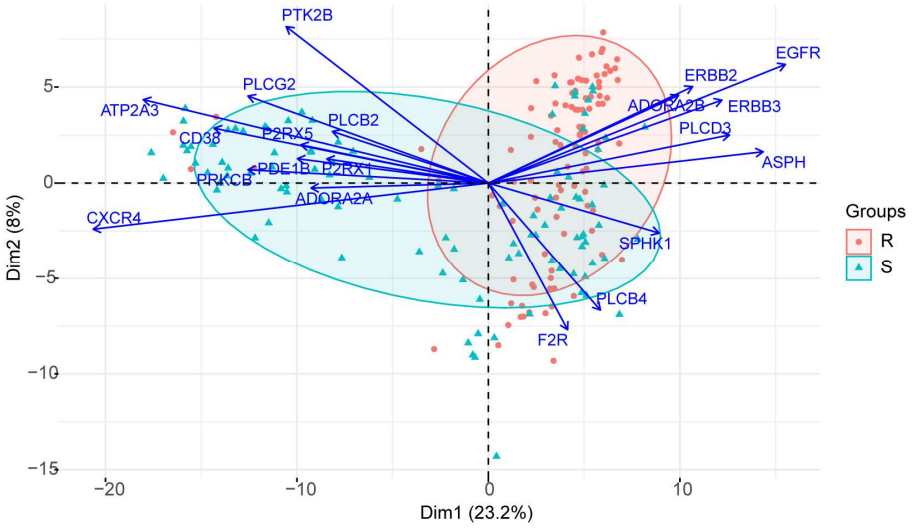

Figure 4.16 Principal component analysis (PCA) of genes in KEGG calcium pathways. Cells have been divided into two groups, including 102 ferroptosis resistant cell lines (R) and 102 ferroptosis sensitive cell lines (S).

4.3 Discussion

Calcium blockers have been reported to have anti-peroxidative protection to membrane lipid peroxidation through altering the structure of the membrane lipid bilayer (Mason et al., 1999a). In this study, MS4A15 was found to play an important role in protecting cells against ferroptosis through disrupting calcium homeostasis and impairing store operated calcium entry as well as preventing lipid ROS production. How calcium alteration affects lipids remodeling was explored in detail.

Metabolomics showed that calcitriol was downregulated in *Ms4a15* OE cells (Figure 4.3). Apart from enhancing cytotoxicity induced by alternative signals like doxorubicin, quinone menadione, and hydrogen peroxide, calcitriol can also regulate cell death through increasing the calcium concentration to disturb calcium signaling, releasing cytochrome *c* or reducing intracellular glutathione to increase the production of ROS (Ravid and Koren, 2003; Sergeev, 2005; Weitsman et al., 2005). Hence, downregulation of calcitriol may help to decrease intracellular calcium concentration.

The reduced ER Ca^{2+} in *Ms4a15* OE reveals lipids with a decrease in number of double bonds and in chain length. The n-3 PUFAs (i.e. EPA (C20:5), DPA (C22:5n-3) and DHA (C22:6)), which can change the fatty acid composition of the membranes and affect different types of membrane proteins are dramatically decreased. EPA, DPA and DHA are

synthesized from α-linolenic acid through a series of enzymatic desaturation and chain elongation reactions (Dyall and Michael-Titus, 2008). *Ms4a15* OE cells incubated with exogenous EPA, DPA and DHA obtained sensitivity to ferroptosis, from which DHA showed the most significant effect followed by DPA and EPA, indicating that PUFAs are the proximate executioners of ferroptosis. Desaturation and elongation steps of the longer chain omega-3 PUFAs in *Ms4a15* OE are inhibited (Figure **4.11**). Of note, the *Ms4a15* OE cells display an accumulation of MUFA-containing phospholipids. One recent research highlighted the role of MUFAs as ferroptosis inhibitors via preventing the accumulation of lipid ROS and displacing PUFAs at the plasma membrane, further suggesting the protective effect is associated with decreased lipid saturation (Magtanong et al., 2019). Together, these results were interpreted as an indication of a reduced elongation and desaturation capacity of fatty acids due to depletion of intracellular ca^{2+} prevents from being elongated and desaturated.

Additionally, there were more than 60 species plasmalogens increased in *Ms4a15* OE, which are crucial endogenous antioxidants in protecting lipids from oxidative stress (Brites et al., 2004). When plasmalogens were exposed to oxidizing conditions, the vinyl ether bond is preferably oxidized, thus protecting the PUFAs in the sn-2 position from being oxidized (Braverman and Moser, 2012). Yet, the control MF cells supplemented with plasmalogens did not show protection to ferroptosis. Indeed, the RNAseq data provides the information that genes involved in initiation of plasminogen biosynthesis at peroxisomes are unchanged, suggesting that the increase of plasmalogens may be a result of calcium depletion but not the key mediator of ferroptosis. One possibility is that, cell membranes contain plasmalogens were reported less fluid than the plasmalogen-deficient membranes (Hermetter et al., 1989), accumulation of plasmalogens could, at least in part, compensate for PUFA induced membrane fluidity for incorporation into the phospholipid bilayer. This might be the reason that *Ms4a15* OE exhibited slower migration. PUFAs have inhibitory effects on migration and calcium influx (Kim et al., 2014; Tonutti et al., 2010). PUFA deprivation, on the other hand, increases calcium import (Zhang et al., 2012). Theoretically, cells could compensate for reduced calcium influx by downregulating PUFA production via various mechanisms.

One striking feature of ether-linked membrane phospholipids is their high AA content (Nakagawa and Waku, 1989) Indeed, plasmalogens serve as a PUFA store at the sn-2 position from where AA could be released through the activity of a plasmalogen-specific PLA2 (PlsEtn-PLA2). AAs are widely known to be degraded by COX pathway and dramatically reduced in *Ms4a15* OE, in keeping with this, *Cox1* is one of the most significantly upregulated genes in *Ms4a15* OE which reduces the abundance of AA. AA can be released either after PLA2 action, or after PLC and DAG lipase. MS4A15 constantly releases calcium and keeps a very low concentration of the ER store and downregulates the

activities of phospholipases, ultimately limiting AA release. However, overexpression of *ATP2A2* keeps pumping in calcium into the ER store and disrupting the low-concentration balance, ultimately resulting in ferroptosis susceptibility.

Calcium signal guides the cell fate via coordinated activity of a suite of calcium channels, pumps, exchangers and binding proteins. According to unbiased hierarchical clustering and principal component analysis of the 204 cancer cell lines from CCLE, genes that drive ferroptosis susceptibility including *ATP2A3*, *CD38*, *P2Rx5*, *PLCG2* and *ADORA2A*. From which, overexpression of *ATP2A2*, for example, has been proved to be able to sensitize the *Ms4a15* OE cells, in line with the report that *SERCA2* overexpression drives proliferation and migration of colorectal cancer cells. On the contrary, genes drive ferrroptosis resistance including *GNAQ*, *SPHK1, ERBB2/3* and *PLCB4* et.al. Of interest, activating mutations in *GNAQ*, which is altered in 32.2% of uveal melanoma patients and 3.79% of melanoma patients, drive uveal melanoma oncogenesis. Moreover, overexpression of *ERBB2/3,* also known as human epidermal growth factor receptor 2 (*HER2/3*), occurs in ~20–25% of breast cancers and causes a worse outcome. *ERBB2/3* belongs to the EGFR family which regulates calcium efflux from the ER. Therefore, overexpression of some of these genes into the *Ms4a15* OE cells could be a strategy to make the cells be susceptible to ferroptosis. On the contrary, knockdown of genes classified in the RSL resistant group could be regarded as an alternative strategy to alter calcium homeostasis.

Ferroptosis resistance is related to cancer cells therapy resistance, solving the link between calcium homeostasis and ferroptosis resistance is of great significance for cancer therapeutics. To verify this hypothesis that calcium homeostasis mediates ferroptosis, more genetic experiments need to be done in the future. Such an understanding could aid in guiding the development of therapies specifically targeting altered calcium signaling in cancer cells during tumorigenic progression.

Acknowledgement

I thank Susanne Pfeiffer for testing compounds for kill curve, and Dr. Constanze Müller for performing metabolomics and lipidomics analyses.

5. Discovery of ferroptosis-specific biomarkers[2]

5.1 Introduction

Cell death is a basic biological process that maintains tissue homeostasis; however, excessive or defective cell death can cause a large number of human diseases. There has been no conclusively evidence that ferroptosis, a newly characterized type of cell death, is pathologically induced in human so far; nonetheless, there exist certain connections with ischemic organ damage, Huntington's disease and cancer, et.al., where ferroptotic cell death may play an essential role in vitro and in vivo (Do Van et al., 2016; Skouta et al., 2014; Stockwell et al., 2017). Due to the lack of specific ferroptosis biomarkers, investigations into tissue pathophysiology are impeded. Currently, a handful of critical ferroptosis regulators have been identified primarily by genetic and chemical screens in vitro. A thorough understanding of the appropriate biomarkers in ferroptosis will likely provide an opportunity to target this process for early detection, accurate diagnosis and rational therapy design.

An unambiguous determination of ferroptosis contribution in these diseases would directly enable clinic pathological assessment and treatment (Figure 5.1). The execution of ferroptosis happens at the membranes. Cell surface proteins account for only about 22% of all proteins in the human genome, however, two-thirds of the protein-based drug targets are surface proteins currently. Therefore, the cell surface proteins are attractive biomarkers of human diseases for novel therapies, due to their involvement in vital signaling pathways and execution of ferroptosis at the membrane (Hopkins and Groom, 2002; Overington et al., 2006).

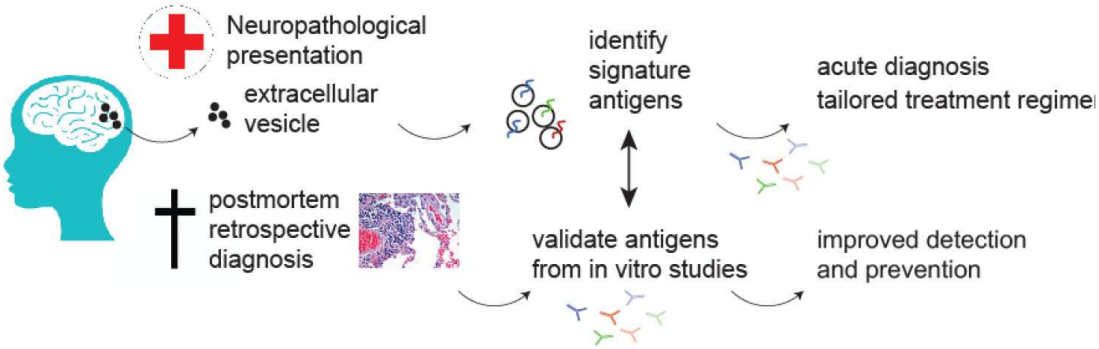

Figure 5.1 Detection of cell death in acute and postmortem presentations. Currently, diagnostic tools for the detection of contemporary or postmortem cell death are limited to apoptosis. This proposal seeks to validate ferroptosis-specific antigens present in (top) extracellular vesicles and

[2] This chapter was adapted from a manuscript in preparation: Shan Xin, Susanne Pfeiffer, Joel A. Schick

(bottom) tissue to enable appropriate diagnostic and treatment regimes. Retrospective diagnosis will impact future treatments associated with similar clinic pathological presentation.

5.2 Results

5.2.1 Identification of cell surface proteins involved in ferroptosis

Due to a lack of discriminating ferroptosis cell death markers, direct demonstration of ferroptosis in humans is missing. Therefore, marker discovery was carried out using the established model of ferroptosis human HT-1080 fibrosarcoma cells, since HT1080 exhibits strong intrinsic sensitivity to ferroptosis. HT1080 cells were treated with RSL3 for biotinylation of cell surface proteins, and a critical time point (3 hours) and RSL3 concentration (2 µM) were identified immediately preceding overt cell death as evinced by membrane impermeable carbocyanine monomer (TO-PRO-3) exclusion (Figure 5.2).

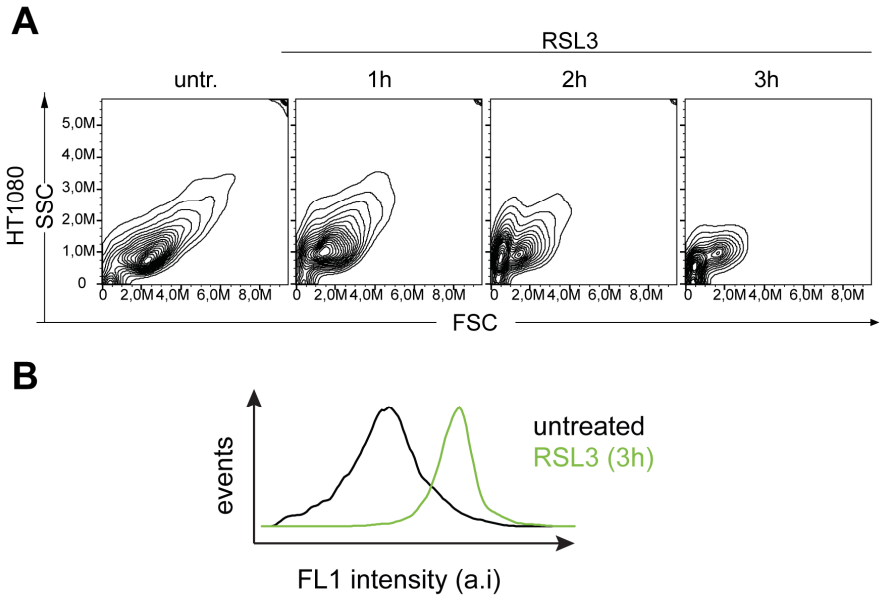

Figure 5.2 Identification of the critical time point for RSL3 treatment. (A) Population shift contour of HT1080 cells treated with RSL3 time course. (B) Oxidized lipid (Bodipy C11) stain of RSL3-treated HT1080 fibrosarcoma for 3 hours. Oxidation of the unsaturated dye results in a shift of the fluorescence emission peak from ~590 nm to ~510 nm (FL1).

Forward scatter revealed two distinct TO-PRO negative populations, termed P1 and P2, with P2 population more tending to approach membrane lapse indicative of viability loss, with elevated TO-PRO-3 labeling (Figure 5.3A). This time point was termed as early-stage ferroptosis. These two populations were isolated for biotinylation of cell surface proteins

using cleavable, cell impermeable biotin and magnetic streptavidin beads. To identify and quantitate differentially expressed proteins, the biotinylated samples were extracted for mass spectrometry analysis and revealed a list of predominantly secreted/membrane-bound proteins (Figure 5.3B). When protein hits were ranked according to the ratio with a minimum of two peptides assigned by MS/MS analysis, protein ratios relative to an unselected control population were determined for each population. Only proteins with positive identification by two different peptides were considered. Overlapping enrichments were observed from both populations, however P2 displayed greater ratios and was chosen for candidate selection. Highly enriched proteins were mapped by volcano plot and evaluated for cell surface or membrane localization (COMPARTMENTS: unification and visualization of protein subcellular localization evidence) with a top score of five indicating high confidence (Figure 5.3). Of the highest scoring 10 proteins, only CDC5L lacks secretory assignment, supporting the robust methodology of membrane protein biotinylation (Figure 5.3D). Moreover, interrogation of associated GO-terms revealed primarily lipid processes implicated in ferroptosis (Figure 5.4).

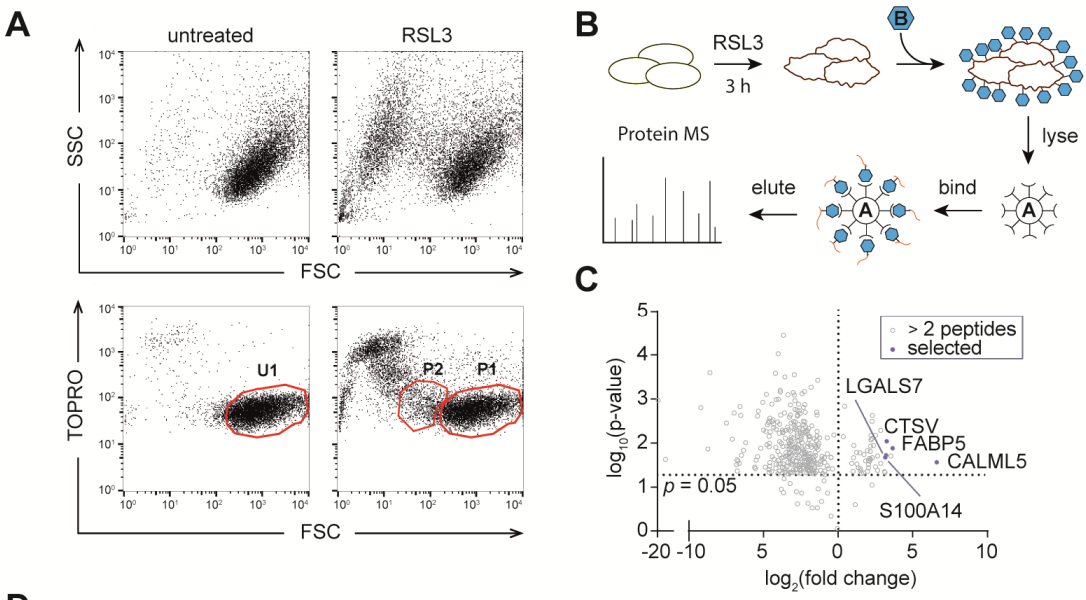

D

symbol	name	P1:U1	P2:U1	*p*-value	membrane	secreted
CALML5	Calmodulin-like protein 5	7.86	98.62	0.0274	2	5
FABP5	Fatty acid-binding protein	1.93	12.53	0.0133	5	5
CDC5L	Cell division cycle 5-like	2.06	11.52	0.0196		
CTSV	Cathepsin L2	1.16	9.59	0.0091	3	5
LGALS7	Galectin-7	0.88	9.33	0.0191	2	5
S100A14	Protein S100-A14	0.79	8.96	0.0213	2	5
LYZ	Lysozyme C	1.87	8.90	0.0466	1	5
TXN	Thioredoxin	0.87	8.83	0.0476	2	5
ANXA1	Annexin A1	1.15	8.76	0.0446	5	5
S100A8	Protein S100-A8	1.10	7.33	0.0052	5	5

Figure 5.3 Cell surface biotinylating assay isolates membrane proteins in early stage ferroptosis. (A) Flow cytometry results of untreated and short (3h) ferroptosis induction (RSL3). (B) Schematic overview of cell surface biotinlyation for populations P1/P2 from (A). (C) Identified proteins in volcano plot in relation to control population. (D) Top 10 identified proteins and likelihood of membrane localization/secretion (0-5, 5 is maximum).

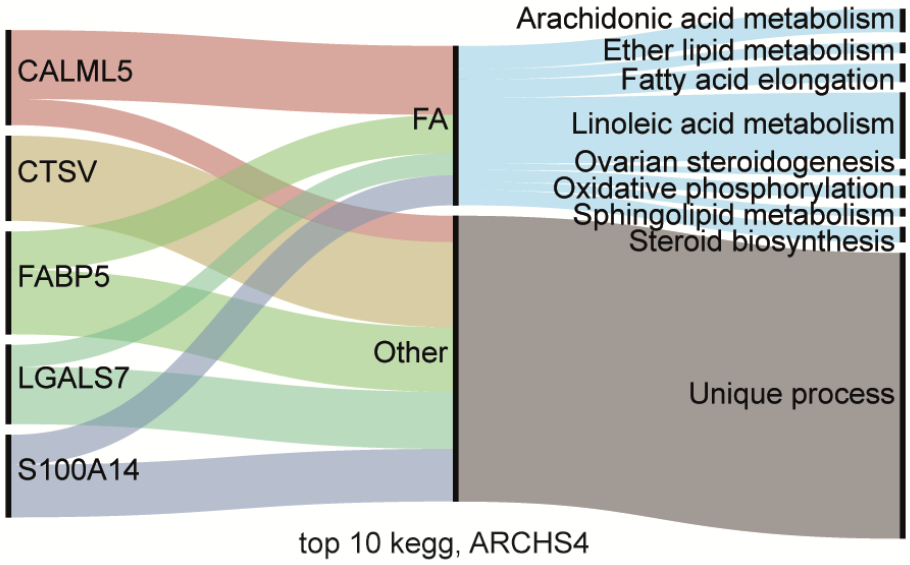

Figure 5.4 Comparative Toxicogenomics Database (CTD) Gene-Disease Associations. Identified proteins revealed a strong association with lipid and fatty acid (FAA) metabolism.

5.2.2 Biomarker candidates are specific to ferroptosis in vitro

The top five cell surface proteins: (Calmodulin-like protein 5 (CALML5), Fatty acid-binding protein 5 (FABP5), Cathepsin V (CTSV), Galectin 7 (LGALS 7), and S100 Calcium Binding Protein A14 (S100A14)), were chosen as the biomarker candidates to validate the differential expression of ferroptosis-associated proteins identified in our analysis against those antibodies that are commercially available. Immunofluorescence staining of the antibodies against the biomarker candidates was first performed to validate the differential expression of the cells treated with RSL3 and straurosporine (at equivalent EC50) as a nonspecific cell death inducer using high-content microscopy. The results indicated that as the duration of RSL3 treatment increased, the expression level of all these five proteins are getting higher, indicated by the fluorescence signal and intensity calculation. However, when cells were treated with straurosporine, a nonspecific inducer of cell death, the expression of CALML5 and S100A14 stay unchanged, while the expression level of FABP5, CTSV and LGALS7 are mostly unchanged (Figure 5.5).

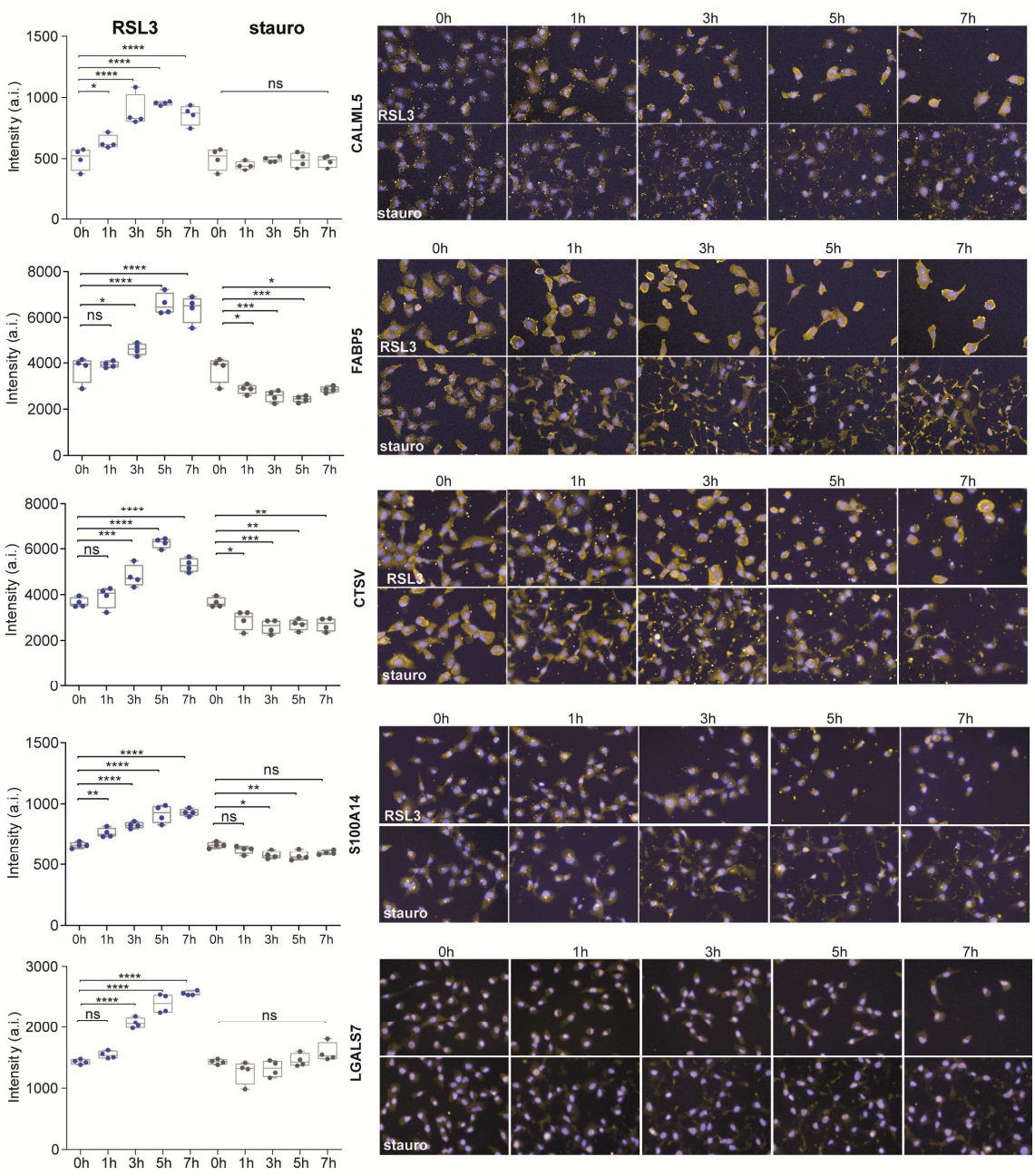

Figure 5.5 Validation of the expression pattern of the biomarker candidates within HT1080 cells using high content microscopy analysis. (A) Panels indicate marker cell intensity (arbitrary intensity units). (B) Right panels show cellular localization and intensity.

The mRNA levels of *CALML5, FABP5, CTSV, S100A14,* and *LGALS7* are consistent with the immunofluorescence protein data that the expression level are increased after RSL3 treatment, indicating the transcriptional regulation of the expression of these candidates (Figure 5.6).

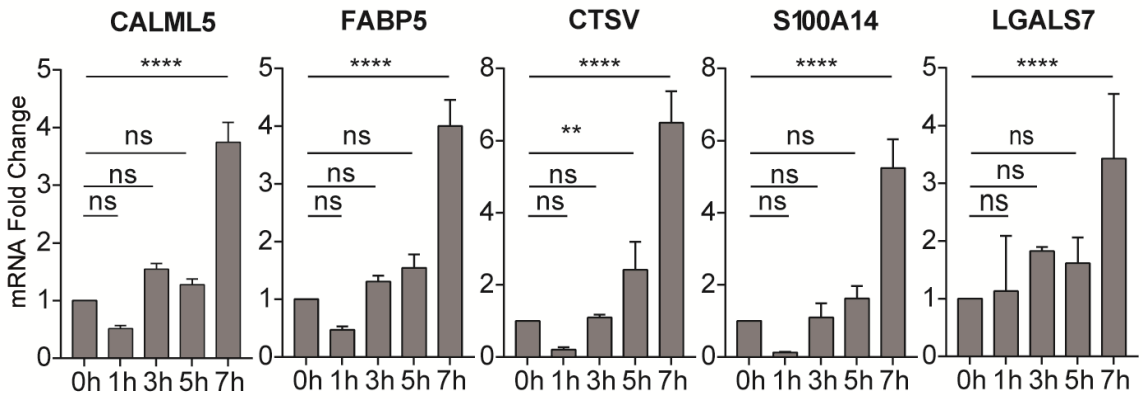

Figure 5.6 mRNA expression level of the biomarker candidates. Relative mRNA expression levels of *CALML5*, *FABP5*, *CTSV*, *S100A14*, *LGALS7* in HT1080 cells treated with RSL3 for 0h, 1h, 3h, 5h and 7h, respectively. Relative mRNA expression is shown as mean ± SD of n = 3 technical replicates of three independent repetitions of the experiment with similar results.

Furthermore, immunofluorescence staining was carried out to investigate specificity of the different candidate biomarkers. The protein levels were examined under different compounds treatment. HT1080 cells were treated with different drugs for 8 h at various concentrations, and the specific concentration of each compound was determined to correspond to IC70-80 as determined by DAPI staining (Figure 5.7A, B). Next, appropriate concentration of each drug was selected to treat the cells for 8 h, and the protein levels of the five candidates were measure under certain conditions using immunofluorescence staining. All of these proteins are highly expressed after RSL3 treatment, whereas the expression only slight increased after IKE treatment, which may due to different activation pathways of ferroptosis. Overall, no significant change of the expression level of the five candidates has been observed when cell death was induced using other oncological substances. Consequently, CALML5, FABP5, CTSV, S100A14, and LGALS7 are putative cell surface protein biomarkers specific for RSL3-induced ferroptosis (Figure 5.8).

Although the antigens discovered are promising beginning for such a study, they will have to be tested for specific staining in tissue, absence of background and individual bands in Western blots. In order to investigate the potential clinical value of these ferroptosis biomarker candidates in human tissues, specific immunohistochemical staining would be performed on pathological (stroke, Alzheimer's, Parkinson disease) and control donor tissue sections. These potential ferroptosis biomarkers would be significantly elevated in degenerative diseases patients compared with control groups. So far, FABP5 is the only one that highly increased on the patients' tissues based on initial evaluation of some of these antibodies on control human paraffin embedded tissue, which showed strong staining and

low to absent background in control sections from glioblastoma brain tumors, while the others are essentially undetectable. Currently, the focus of us is to identify high-performing antibodies, and validate the specificity of FABP5 and breadth of ferroptosis in human degenerative diseases. FABP5 is a lipid binding protein; mass spectrometry analysis of material from the same source serves as a strong complement to histological analysis of human tissue.

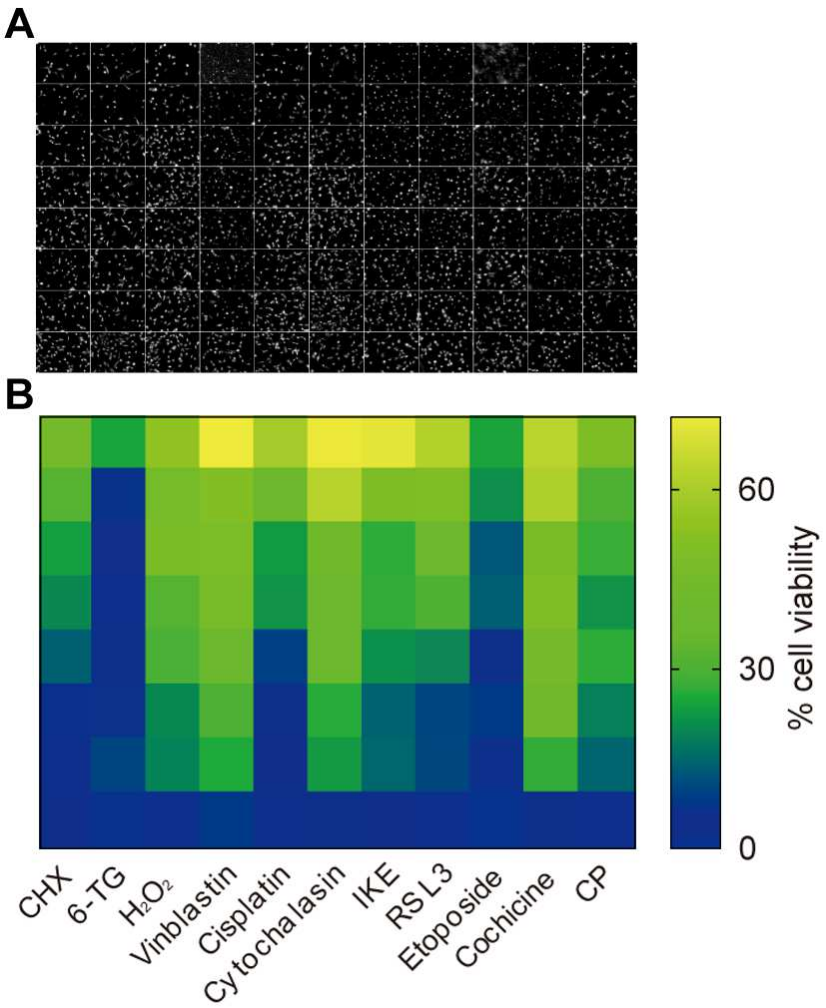

Figure 5.7 Detection of appropriated death rate detection upon cell death induction. (A) Digital phase contrast images using high content Cells treated with different compounds listed in (B) at concentrations indicated in methods for 8 h. (B) Heat map of the cell viability of cells treated with different compounds at concentrations indicated in methods for 8 h. CHX, cycloheximide; 6-TG, 6-thioguanine; H_2O_2, hydrogen peroxide; CP, cyclophosphamide.

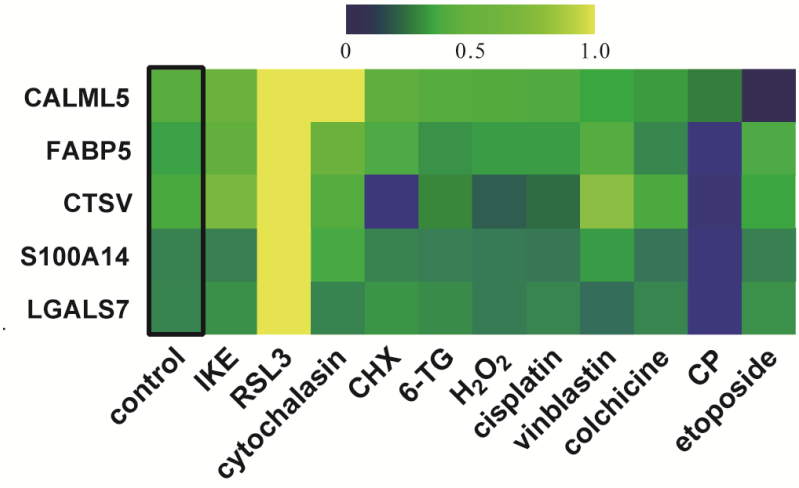

Figure 5.8 Validation of the specificity of the the biomarker candidates for ferroptosis. Marker specificity upon cell death induction. Heat map (yellow=high signal) derived from high content microscopy following stimulation with ferroptosis inducer RSL3 or cancer therapeutics (CHX, cycloheximide; 6-TG, 6-thioguanine; H_2O_2, hydrogen peroxide; CP, cyclophosphamide).

5.3 Discussion

Cell surface proteins are responsible for cellular contact and communication, and contributing more than two-thirds of known protein-based drug targets while accounting for only about 22% of all proteins in the human genome (Hopkins and Groom, 2002; Overington et al., 2006). Nevertheless, it is a difficult to investigate cell surface proteins due to their low absolute content and their hydrophobic nature. In this chapter, several cell surface proteins that are specifically associated with ferroptosis were identified via using mass spectrometry analysis to compare an isogenic pair of cells treated with RSL3 or control (DMSO).

In the cell surface analysis, only CDC5L, which is from the highest scoring 20 proteins, lacks secretory assignment, supporting the robust methodology of P2 membrane protein biotinylation. Furthermore, the results about the investigation of the top five biomarker candidates demonstrated that the expression level of these proteins can be specifically upregulated with RSL3 treatment but not with the treatment of other drugs that induce different cell deaths, which nicely proves the cell biotinylation assay to be a valuable tool as well as illustrates the validity of the cell line model.

Among all the highly enriched proteins, CALML5 or calmodulin-like skin protein (CLSP) is of the highest score, which encodes a novel calcium binding protein expressed in the epidermis (Hwang et al., 2007; Sun et al., 2015a) and shows elevated levels in skin disease like

psoriasis (Méhul et al., 2006). Loss of *CALML5* leads to an impaired epidermal barrier (Sun et al., 2015a), indicating a role of CAML5 in maintaining cell integrity. In the present study, the expression of CALML5 increased with the time course treatment of RSL3, suggesting a potential role not necessarily in responding to cell death challenge. However, based on initial staining on human paraffin embedded tissue, CALML5 is essentially undetectable which may be caused by three reasons. First, antibodies work differently on fixed cells and on paraffin-embedded tissue; second, CALML5 may express highly at the initiation of cells death to protect cells but not after execution; third, the fixation of the tissues was not good. These reasons may also apply to CTSV which is a proteolytic enzyme with strong staining on fixed cells after ferroptosis induction but remains undetectable on paraffin-embedded tissue. Loss of CTSV has been reported to result in the development of fibrosis, proliferative vasculopathy and the altered phenotype of keratinocytes in systemic sclerosis (Noda et al., 2013). Indeed, CTSV expression level was remarkably and uniformly decreased in cultured dermal fibroblasts from early-stage systemic sclerosis compared with healthy controls (Noda et al., 2013), indicating the importance in maintain health.

FABP5 is a lipid binding protein, previous studies have reported the upregulation of FABP5 in many types of tumors, such as atherosclerosis (Furuhashi et al., 2017), lymph node metastasis (Lv et al., 2019; Wang et al., 2016) and high Gleason score prostate cancer (Fujita et al., 2017). As many diseases are followed with cell death, FABP5 acts as a potential ferroptosis-specific biomarker for human disease. In fact, FABP5 deficiency leads to suppress the development of insulin resistance, diabetes mellitus and atherosclerosis (Furuhashi et al., 2017). Additionally, in clear cell renal cell carcinoma (ccRCC), FABP5 may exert a pro-proliferative role that overexpression of FABP5 promoted cell proliferation, while silencing of FABP5 significantly inhibited cell proliferation (Lv et al., 2019). Overall, FABP5 expression significantly correlates with the clinical characteristics; thus, upregulation of FABP5 can be a promising indicator for detecting some ferroptosis related diseases, which is in line with the result that FABP5 expression is elevated specifically after RSL3 treatment as well as highly increased on the patients' tissues according the initial evaluation.

LGALS7 and S100A14 were among the top five ferroptosis biomarker candidates. Ferroptosis is involved in various diseases such as cancers. According to the previous studies, the upregulation of LGALS7 expression level in breast cancer cells drastically increased their metastasis ability (Demers et al., 2010); while S100A14 has been reported as an independent prognostic factor in triple-negative breast cancer (TNBC) (Ehmsen et al., 2015) and in hepatocellular carcinoma (HCC) (Mohamed et al., 2019) due to the high expression level in these tumors together with equally poor outcomes. In our results, the expression levels of these two proteins showed a robust increase after RSL3 treatment in

vitro, whereas only very weak signal can be detected in patients' paraffin-embedded tissues. This inconsistence may due to the difference between in vitro and in vivo; therefore, tissue staining with higher concentrations of the antibodies should be tested in the second evaluation.

In conclusion, a panel of biotinylated cell surface proteins, whose expression was correlated with ferroptosis, has been identified. Theses putative biomarkers may provide a novel therapeutic strategy for human degenerative diseases. A further understanding of the mechanism underlying the link between the expression level of the other ferroptosis biomarker candidates and degenerative diseases may enable the development of diagnostic tests and new therapeutic strategies for a variety of important diseases.

Acknowledgement

I thank Susanne Pfeiffer, Dr. Juliane Merl-Pham and Dr. Stefanie Hauck for performing cell surface biotinylation to identify the candidates.

6. Summary

Ferroptosis has argued a perspective for the potential utilization in human diseases since it has been first reported (Dixon et al., 2012), with the fast-growing investigation in pathological research. In this dissertation, the mechanism and potential application of ferroptosis were evaluated through the functional exploration of MS4A15 and the discovery of putative biomarkers.

MS4A15 protects cells from ferroptosis through calcium-driven lipid remodeling

The ER-located membrane protein, MS4A15, was investigated to protect against ferroptosis robustly and specifically through modulating Ca^{2+} homeostasis and depressing IP_3R expression, ultimately preventing lipid ROS generation. This is consistent with previous reports about this family that MS4A1/CD20, a component of SOCE, accounts for recruiting immune effectors as well as mediating cell death within the lipid raft (Deans et al., 2002; Shan et al., 2000). MS4A12 blocks the replenishment of Ca^{2+} through acting as a part of SOCE in intestinal cells (Koslowski et al., 2008). In contrast to MS4A1 and MS4A12, which promote SOCE, MS4A15 leads to constitutive depletion of ER stores and loss of capacitive Ca^{2+} entry. Thapsigargin has similar profile with MS4A15 in regulating calcium oscillation. Strikingly, 48h pretreatment of thapsigargin before challenge with RSL3 significantly protected cells in line with diminished peroxidized membrane lipids. More importantly, promoting calcium influx via overexpressing ER Ca^{2+} ATPase 2 re-sensitized cells to RSL3-induced ferroptosis. Taken together, enhanced ferroptosis resistance is a consequence of persistent calcium stores depletion.

Calcium blockers (amlodipine, verapamil, diltiazem) have been reported to protect against membrane lipid peroxidation through altering the structure of the membrane lipid bilayer, this mechanism also prevented the glutathione decrease caused by inhibition of peroxide generation (Mak et al., 1992; Mason et al., 1999b). Here, a close correlation between calcium levels and fatty acyl composition of lipids was demonstrated. Compared with ferroptosis sensitive cells (MF control and tharpsigarging short-term treated), the resistant cells showed an accumulation of SFAs, MUFAs and plasmalogen species, but a dramatic decrease of long chain fatty acids and PUFAs, indicating that the fatty acid elongase and desaturase activities may be under a calcium-dependent regulatory effect. One recent research reported that MUFAs act as ferroptosis inhibitors via preventing the accumulation of lipid ROS and displacing PUFAs at the plasma membrane, further suggesting the protective effect is associated with decreased lipid saturation (Magtanong et al., 2019). Additionally, plasmalogens species, which are crucial endogenous antioxidants in protecting

lipids from oxidative stress, were increased to compensate for PUFA induced membrane fluidity and resulted in the slower migration of *Ms4a15* OE.

In this context, *Ms4a15* OE cells incubated with exogenous EPA, DPA and DHA obtained sensitivity to ferroptosis, whereas, the control MF cells supplemented with plasmalogens did not show protection to ferroptosis. Plasmalogens are crucial endogenous antioxidants in protecting lipids from oxidative stress (Brites et al., 2004). When plasmalogens were exposed to oxidizing conditions, the vinyl ether bond is preferably oxidized to protect the FUFAs from being oxidized (Braverman and Moser, 2012). The reason why plasmalogens did not show protection role is uncertain, which may because of the lack of appropriate protocols or not enough species added. It could also because of the possibility we put up that, accumulation of plasmalogens could compensate for PUFA induced membrane fluidity for incorporation into the phospholipid bilayer.

Further experiments could be conducted to clarify this problem via i) updating current protocols for pretreating plasmalogens before adding into cells; ii) adding different plasmalogen species at once into the cells; iii) modulation of the rate-limiting genes of plasmalogen biosynthesis.

Regulating calcium homeostasis to reverse cancer therapy resistance

Calcium signaling is complex; this complexity indicates that disruption of calcium homeostasis can be a feature of certain pathological states, including cancer. Intriguingly, cancer cells that escape from other types of cell death are likely to undergo ferroptosis, suggesting a new strategy for cancer therapy. Indeed, alterations of calcium signal for cancer treatment have been reported that manipulation of intracellular calcium signal can control EMT induction in human breast cancer cells, therefore preventing metastases (Davis et al., 2014) .

Based on the results in this context, persistent Ca^{2+} depletion affects fatty acids desaturation capacity, ultimately constraining PUFA synthesis. However, since PUFAs can regulate T-cell activation and proliferation, reduced PUFA would affect cell proliferation and the immune response. Human cancer cells in a high mesenchymal state are typically inhibiting synthesis of PUFA to migrate slowly in a GPX4-dependent manner and contribute to therapy-resistance (Viswanathan et al., 2017). Consistently, persistent cancer cells which escape from conventional cytotoxic treatment via a dormant state depend on the GPX4 pathway. In keeping with this, overexpression of *Ms4a15* retards cell migration as well as drives lipids remodeling through alteration of calcium homeostasis. Therefore, execution of ferroptosis through triggering calcium influx may be critical for reversing therapy-resistance in cancer strategy.

Cancers are heterogeneous and are able to acquire resistance to chemotherapy over time; there are not many effective strategies to chemotherapy resistant cancers currently. To verify whether altering Ca^{2+} homeostasis can reverse cancer therapy-resistance, genetics modulation need to be conducted in ferroptosis resistant cancer cells to regulate the sensitivity. The key genes that drive ferroptosis sensitivity are mostly reported to be involved in cancer oncogenesis. These genes are divided into two groups which promote Ca^{2+} influx and efflux, respectively. We may be able to either overexpress the genes that drive ferroptosis susceptibility to sensitize the cells, or knockdown of key genes classified in the RSL resistant group as an alternative strategy to alter Ca^{2+} homeostasis, and ultimately initiate ferroptosis of cancer cells. Exploring more novel mechanisms would be beneficial for cancer therapy.

Utilization of ferroptosis in human diseases

Excessive or defective cell death leads to a large number of human pathologies, such as apoptosis in human colorectal cancer (Simpson et al., 2013) and cardiovascular disease (Singh et al., 2011), and non-apoptotic cell death in stroke (Li et al., 2003), Alzheimer's (Lassmann et al., 1995), Parkinson's (Hartmann and Hirsch, 2001), and Huntington's (Turmaine et al., 2000) diseases.

Although extensive research indicated that ferroptosis could be triggered by diverse physiological conditions and pathological stresses in animals, no conclusive evidence has been demonstrated under pathological conditions in humans yet. The cumulative implication of ferroptosis in ALS (Kwan et al., 2012), Alzheimer's (Ghosh et al., 2014; Zhang et al., 2018), Parkinson's (Do Van et al., 2016) and Huntington's (Skouta et al., 2014), is based on cell culture experiments and in vivo evidence, whereas no evidence has been demonstrated under pathological conditions in humans so far. In this work, several cell surface proteins that are specifically associated with ferroptosis were identified using mass spectrometry analysis. Among which, CALML5, FABP5, CTSV, S100A14, and LGALS7 are putative cell surface protein biomarkers specific for RSL3-induced ferroptosis.

Further experiments need to be performed on various types of patients' paraffin-embedded tissues, such as stroke, Alzheimer's, Huntington's and Parkinson's diseases, for immunohistochemistry stain of the biomarker candidates. The results might provide evidence for characterizing ferroptosis in acute and postmortem conditions in Human by a combination of marker discovery on cells and human pathologic tissue. Insights into adequate ferroptosis biomarkers for human diseases will likely provide more chances to target this process for rational therapy design. Therefore, central to current research and clinical efforts is to find ferroptosis-specific biomarkers of human diseases for detection of disease state, accurate

diagnosis, better prognosis, and drug improvement, which can accelerate medical development.

The exact mechanism(s) of ferroptosis still needs to be further elucidated, however, the identification of the connection between calcium and ferroptosis together with the discovery of ferroptosis-specific biomarkers have established a new level of ferroptosis in diagnosis and therapeutics of human diseases. I hope that this work will contribute to the treatment for the diseases.

7. Methods and materials

7.1 Molecular biological methods

7.1.1 Phenol-Chloroform Extraction of genomic DNA for NGS

TE Lysis Buffer	10 mM Tris/HCl pH8 1 mM EDTA 50 mM KCl 2 mM MgCl2 fresh: 200 µg/ml RNAseA; 625 ng/ml ProtK
Phenol	Roth, 0038.1
Phenol/Chloroform/Isoamylalcohol	Roth, A156.3
Chloroform	Merck, 1.02445.2500
Ethanol (100%)	Merck

Genomic DNA was isolated from certain cells based on the requirement. Cells were harvested and lysed overnight at 60 °C in TELysis buffer. The reaction was stopped at 95 °C for 2 min. Subsequently, added one volume of Phenol to each sample and invert 5-8 times, spun at 14,000rpm for 5 min at 4 °C. The supernatant was removed carefully and transferred to an Eppendorf tube. Added one volume of Phenol/Chloroform/Isoamylalcohol to each tube inverted 5-8 times and spun at 14,000rpm for 5 min at 4 °C. Removed the supernatant to a new tube and added one volume of Chloroform, invert 5-8 times, spun at 14,000 rpm for 5 min at 4 °C. Removed the supernatant to a new tube, added 2.5 volumes of 100% Ethanol and spun at 14,000 rpm for 5 min at 4 °C. Removed the remaining ethanol and solved genomic DNA in 40 µL HPLC water and heat it for 30 min at 55 °C, stored at -20 °C for following experiments. The concentrated gDNA can be used for PCR reactions.

7.1.2 Molecular cloning of the reporter plasmids

The cloning of the plasmids used in this study were previously described (Kunzelmann and Mehta, 2013). To this end, the MS4A15/Ms4a15 and TMEM33 introns were amplified by PCR using primers that contain restriction enzyme recognition sites at their ends and the corresponding splice signals / mutations.

Table 2 Amplification primers used in this study

Genes	Primers

Human *MS4A15*	tctcatcattttggcaaagaattcgccaccatgtctgcagctcccgccagcaatg
	cctctagctacctagctagctcacttatcgtcatcgtctttgtaatcgacgactccttgggcatatgcc
	ac
Human *TMEM33*	acgagactagcctcgaggtttaaacgccaccatggcagatacgaccccgaacg
	ccttcgccgctgccactagtcaggtcctcctcgctgatcagc
Mouse *Ms4a15*	tctcatcattttggcaaagaattcgccaccatgtgggagcgcagaggcagaggggagtcag
	cctctagctacctagctagcttaaaatctaagccacgctgtt

Prior to ligation, the PCR products and the Plasmid were digested with the enzymes. The digested plasmid backbone was treated with FastAP (Thermo) to remove the 5' phosphate at the ends. Linearized and dephosphorylated plasmid backbones and PCR products were purified by using the Wizard SV Gel and PCR Clean-Up System (Promega) according to the manufacturer's instructions.

Insert and backbone DNA was ligated using T4 DNA ligase (NEB) according to the manufacturer's instructions. E. coli cells (XL2) were transformed with the ligation product. After selection on LB-Amp-plates, positive clones were validated by colony PCR, subsequent restriction digest and sequencing (Eurofins GATC). Sequencing results were analyzed using the Finch TV and Vector NTI.

7.1.3 RNA isolation and reverse transcription, qPCR

Total RNA was isolated with the InviTrap Spin Universal RNA Mini Kit (Stratec Molecular 1060100200) according to the manufacturer's instructions including a DNAse treatment step (Promega M6201). Subsequently, 2 µg total RNA of each sample was reverse transcribed using random hexamer primer and AMV Reverse Transcriptase (NEB).

Quantitative PCR reactions were prepared using the LightCycler480 (Roche) with Power SYBR Green PCR Master Mix (Thermo Fisher Scientific 4368577). Differences in mRNA levels compared to control were calculated by the $2^{-\Delta\Delta Ct}$ method (Livak and Schmittgen, 2001) using Gapdh as a reference gene. Each sample condition contains at least three biological replicates and all measurements were performed with four technical replicates.

Table 3 qPCR primers used in this study:

Genes	Primers
Human *MS4A15*	ccgagaagaaccacaccagt
	tgacgctgaggatgttggt

Human *TMEM33*	cactcatctttgtaaattcctatcca
	ggcagcatgaagcaaagag
Human *CALML5*	gccctgcagtggaatgag
	ttcatggaactcggcagtc
Human *FABP5*	gcagacccctctctgcac
	tcgcaaagctattcccactc
Human *LGALS7*	ggcttggttcctcccaat
	ccttgctccttgctgttga
Human *S100A14*	cttctgagctacgggacctg
	ttctcttccaggccacagtt
Human *CTSV*	ggcaacacacagaagattatatgg
	tcattttcatattcttttcccaca
Mouse *Serca2a2*	gggcaaagtgtatcgacagg
	tcagcaggaactttgtcacc
Mouse *Ms4a15*	gtcagcagccggtacagc
	ggatgacaacgaacacacca
Mouse *Tmem33*	gctcaggccttgttagagga
	gcaaagaaaataacaagactggaaa
Mouse *Actin*	cctctatgccaacacagtgc
	gtactcctgcttgctgatcc
Mouse *Gapdh*	gggttcctataaatacggactgc
	ccattttgtctacgggacga

7.2 Protein biochemistry

7.2.1 SDS - PAGE and western blotting

SD-polyacrylamide gel electrophoresis (SDS-PAGE) and western blotting was performed as previously described in (Aumiller et al., 2012).

Buffers used in this part are:

Lysis buffer	63 mM Tris-HCl, pH 6.8 10% glycerol 2% SDS 2.5% DTT 1x protease inhibitor tablet
SDS-running buffer (5x)	125 mM Tris/HCl, pH 7.5 1.25 M glycine 5% SDS
Blotting buffer	Tris pH 8.3 (48 mM) Glycine (39 mM) Methanol (20 % (v/v)) SDS (0.03 % (w/v))
TBST	NaCl (137 mM) Na2HPO4 (10 mM) KCl (2.7 mM) KH2PO4 (1.7 mM) Tween-20 (0.1 % (v/v))
Milk	5% in TBST

Approximately $5x10^6$ cells per condition were lysed in 300 µL lysis buffer for 30 min. DNA was shredded with a sonicator and was pelleted for 20 min at maximum speed centrifugation at 4 °C. The supernatant was mixed with 4x Roti®-Load (Roth) and run on a 6-12% SDS-PAGE gel and transferred onto PVDF membranes using electrophoretic semi-dry western blot transfer system. Membranes were blocked with 5% non-fat milk in PBS-T for 1 h at room temperature and incubated in specific primary antibody overnight at 4 °C. Membranes were washed for 3X10 min in PBS-T before addition of HRP-coupled secondary antibodies for 1 h at room temperature. ECL prime Western blotting detection reagent (GE Healthcare) was used for chemiluminescence detection according to the manufacturer's instructions. Each experiment presented was repeated at least twice.

Following antibodies were used:

Primary antibodies:

Table 4 Antibodies used in WB.

Antibodies	Source	Dilution

Mouse anti-MS4A15	Regina	1:10 in 2.5% BSA - TBST
Rabbit monoclonal anti-ERK1/2	cell signaling	1:1,000 in 2.5% BSA - TBST
Rabbit monoclonal anti-pERK1/2	cell signaling	1:1,000 in 2.5% BSA - T
Mouse monoclonal anti-STAT3	cell signaling	1:1,000 in 2.5% BSA - TBST
Mouse monoclonal anti-pSTAT3	cell signaling	1:1,000 in 2.5% BSA - TBST
Rabbit monoclonal anti-Akt	cell signaling	1:1,000 in 2.5% BSA - TBST
Rabbit monoclonal anti-pAkt	cell signaling	1:1,000 in 2.5% BSA - TBST
Mouse monoclonal anti-IP_3R1	Biozol	1:500 in 2.5% BSA - TBST
Mouse monoclonal anti-ß-Actin (8H10D10)	cell signaling	1:2,000 in 2.5% BSA - TBST
Mouse monoclonal anti-Flag M2	Sigma	1:1,000 in 2.5% BSA - TBST
Rabbit polyclonal anti-Flag	Sigma	1:1,000 in 2.5% BSA - TBST
Mouse monoclonal anti-Myc-Tag (9E10)	Abcam	1:500 in 2.5% BSA - TBST
Rabbit monoclonal anti-Myc-Tag (71D10)	cell signaling	1:500 in 2.5% BSA - TBST
Mouse monoclonal anti-Vinculin	Abcam	1:1,000 in 2.5% BSA - TBST
Rabbit polyclonal anti-ATP2A2	Elabscience	1:500 in 2.5% BSA - TBST

Secondary antibodies:

Antibodies	**Source**	**Dilution**
Anti-rabbit-HRP	cell signaling 7074	1:2,000 in 2.5% BSA - TBST
Anti-mouse-HRP	cell signaling 7076	1:2,000 in 2.5% BSA - TBST

7.2.2 Immunoprecipitation and mass spectrometry

HEK 293T cells were seeded at $1x10^6$ in 10 cm plates the day before transfection. Transfections were performed in triplicates with 10 µg of each plasmid using Lipo2000. The transfected cells were harvested 24 h later in 1 ml RIPA lysis buffer (50 mM Tris HCl, pH 8.0, 150 mM sodium chloride, 1% NP40, 0.5% sodium deoxycholate, 0.1% SDS, 1 mM EDTA,

protease inhibitors (Complete mini, EDTA-free, Roche Diagnostics)). Cells were crosslinked using 1% formaldehyde at RT for 10 minutes, with incubation for 7 minutes followed by 3 minutes centrifugation at 1,800xg. The supernatant was removed and the reaction was quenched with 0.5 ml ice-cold 1.25 M glycine/ PBS. Cells were transferred to a 1.5 ml Eppendorf tube, spun, washed once in 1.25 M glycine/PBS and lysed in 1 ml RIPA buffer per cells for 60 minutes on ice. Cell lysates were homogenized using vortex after 30 minutes. Lysates were spun for 30 minutes at 20,000 g after lysis to remove insoluble debris.

Lysates were precleared by incubation with 20 µl protein G agarose beads (Protein A/G PLUS-Agarose, Santa Cruz) for 2 h. 2 µl antibodies were incubated in the precleared lysates for 1 h, after that 20 µl of beads were added and immunoprecipitation was performed overnight. All steps were performed with mild agitation at 4°C. The beads were washed three times with RIPA buffer and incubated in 1X Roti Loading Dye (Phosphate buffered, 8% SDS, 40% glycerol, 20% β-mercaptoethanol, 0.015 % mg/ml bromophenol blue) at 65 °C for 5 min. Samples were stored at 80°C for mass spectrometric analysis.

Dried beads after pulldown of MS4A15 from formaldehyde-fixed samples were resuspended in 50 µl 1x Laemmli and de-crosslinked for 60 minutes at 99 °C. After centrifugation, the supernatant containing eluted proteins was digested using a modified FASP procedure (Wiśniewski et al., 2009). Briefly, after reduction and alkylation using DTT and IAA, the proteins were centrifuged on a 30 kDa cutoff filter device (Sartorius), washed thrice with UA buffer (8 M urea in 0.1 M Tris/HCl pH 8.5) and twice with 50 mM ammoniumbicarbonate. The proteins were digested for 2 h at room temperature using 0.5 µg Lys-C (Wako Chemicals, Neuss, Germany) and for 16 h at 37 °C using 1 µg trypsin (Promega, Mannheim, Germany). After centrifugation (10 min at 14,000 g) the eluted peptides were acidified with 0.5% TFA and stored at -20 °C.

LC-MS/MS analysis was performed on a Q-Exactive HF mass spectrometer (Thermo Scientific) online coupled to an Ultimate 3000 nano-RSLC (Thermo Scientific). Tryptic peptides were automatically loaded on a C18 trap column (300 µm inner diameter (ID) x5 mm, Acclaim PepMap100 C18, 5 µm, 100 Å, LC Packings) at 30 µl/min flow rate prior to C18 reversed phase chromatography on the analytical column (nanoEase MZ HSS T3 Column, 100Å, 1.8 µm, 75 µm x 250 mm, Waters) at 250 nl/min flow rate in a 95 minutes non-linear acetonitrile gradient from 3 to 40% in 0.1% formic acid. Profile precursor spectra from 300 to 1,500 m/z were recorded at 60,000 resolution with an automatic gain control (AGC) target of $3e^6$ and a maximum injection time of 50 ms. TOP10 fragment spectra of charges 2 to 7 were recorded at 15,000 resolution with an AGC target of $1e^5$, a maximum injection time of 50 ms, an isolation window of 1.6 m/z, a normalized collision energy of 27 and a dynamic exclusion of 30 seconds.

Generated raw files were analyzed using Progenesis QI for proteomics (version 4.1, Nonlinear Dynamics, part of Waters) for label-free quantification as described previously (Hauck et al., 2010; Merl et al., 2012). Features of charges 2-7 were used and all MSMS spectra were exported as mgf file. Peptide search was performed using Mascot search engine (version 2.6.2) against the Swissprot human protein database (20237 sequences, 11451954 residues). Search settings were: 10 ppm precursor tolerance, 0.02 Da fragment tolerance, one missed cleavage allowed. Carbamidomethyl on cysteine was set as fixed modification, deamidation of glutamine and asparagine allowed as variable modification, as well as oxidation of methionine. Applying the percolator algorithm (Brosch et al., 2009) resulted in a peptide false discovery rate of 0.73%. Search results were reimported in the Progenesis QI software. Proteins were quantified by summing up the abundances of all unique peptides per protein. Resulting normalized protein abundances were used for calculation of fold-changes and statistical values.

The $\log_2$ of the normalized protein abundance ratios MS4A15/GFP and $-\log_{10}$ of corresponding p-values of all quantified proteins were plotted in a volcano plot. A very specific pulldown in the MS4A15-PD samples and very low protein abundances in the GFP controls lead to the appearance of mainly only one “arm” of the volcano plot.

7.2.3 Metabolomics and proteomics

Procedures to measure metabolomics and proteomics were previously described (Kraft et al., 2019).

Cell pellets were lysed by vortexing and sonification in two freeze-thaw cycles using 200 µL 8 M urea in 0.1 M Tris/HCl pH 8.5. Equal total protein amounts (10 µg) of the resulting crude cell lysate were digested with a modified FASP procedure (Grosche et al., 2016; Wisniewski et al., 2009) using Lys-C and trypsin as proteases and Microcon centrifugal filters (Sartorius Vivacon 500 30kDa). Approximately 0.5 µg peptides per sample were measured in a randomized fashion on a Q-Exactive HF mass spectrometer online coupled to an Ultimate 3000 RSLC (Thermo Fisher Scientific) in data-independent acquisition mode as described previously (Lepper et al., 2018; Mattugini et al., 2018).

For data analysis, the recorded raw files were analyzed using the Spectronaut Pulsar software (Biognosys;(Bruderer et al., 2016)) with a peptide identification false discovery rate <1% , using an in-house mouse spectral library which was generated using Proteome Discoverer 2.1 and the Swissprot Mouse database (release 2016_02). Quantification was based on MS2 area levels of all unique peptides per protein and normalized protein quantifications were exported. Log_2 transformed abundance ratios to the median abundance per protein were used for heat map generation in cluster 3.0 (Eisen et al., 1998), with

clustering of proteins using the 'Euclidean distance' setting and the 'complete linkage' algorithm. The resulting tree and heat map were visualized with Java Treeview. The mass spectrometry proteomics data have been deposited to the ProteomeXchange Consortium via the PRIDE (Perez-Riverol et al., 2019) partner repository with the dataset identifier PXD014810.

7.2.4 Lipid extraction and global lipidomics

Procedures for lipid extraction and global lipidomics profiling using UPLC-MS were in detail described early (Witting and Schmitt-Kopplin, 2016). In short, we used a two-step MTBE extraction in a cooled Precellys (Bertin). The organic content was analyzed using data-dependent auto LC-MS/MS (maXis, Bruker Daltonics, Bremen, Germany, coupled to an UHPLC Acquity, Waters, Eschborn, Germany) using reverse phase chromatography (RP) columns in both positive and negative electrospray modes. The injection volume was set to 10 µL. RP was performed on a CORTECS UPLC C18 column (150 mm x 2.1 mm ID 1.6 µm, Waters Corporation) using 10 mM ammonium formate and 0.1% formic acid in 60% acetonitrile/water mixture (A) and B 10 mM ammonium formate and 0.1% formic acid in 90% isopropanol/acetonitrile mixture (B) as mobile phase. The gradient was set to 32% B for 1.5 min, followed by an increasing proportion of B to 97% at minute 21 and a plateau for the remaining 4 min. Column temperature was kept at 40 °C and flow rate was set to 0.25 ml/min. A quality control consisting of an aliquot of each samples as well as pure solvent blanks were included in the sample que and used for column equilibration. The MS analysis alternated between MS and data-dependent MSn scans using dynamic exclusion. Raw data were extracted, peak identified and quality control processed using Genedata software (Genedata Expressionist 13.5, Genedata). M/z features were annotated using MassTRIX web server with a maximal mass error of 0.005 Da. MSn information was annotated based on MoNA library using MSPepSearch, Metfrag and further validated by manual curation as the very helpful MSn software are still prone for false identification (Witting et al., 2017). Identification was done for PC based on head group fragment 184, 125, 105 and M-R1/M-R1-OH for PCs. Furthermore, the existence of the vinyl ether linkage was verified via acidic hydrolysis. For this an aliquot of 70 µl of the extract was used for acidic hydrolysis, 7 ml of 32% HCl was added and a reaction time of 30 min was given. Samples were evaporated and reconstituted in methanol prior MS analysis (Boncompain et al., 2014). Under the chosen conditions, only vinyl ether linkages in plasmenyl-compounds are cleaved. Ether and ester bindings are stay intact.

Statistical analysis

Statistical analysis was performed in R studio and simcaP. All data are presented as mean ±SEM. To identify metabolites that show significant change a Mann-Whitney U test for non-parametric variables was performed, and BH corrected for multiple testing. Missing values were imputed by randomly generated minimum values and the data was TIC normalized. Unit variance scaling and mean centering was applied before statistical testing. PLS-DA models were validated by performing 100 random permutations.

7.3 Cell culture

7.3.1 Cell lines and culture conditions

Cells were maintained in their preferable media.

Table 5 Cell lines and medium used in this work.

HT1080	DMEM
HCT116	DMEM
MCF7	DMEM
MDA-MB-231	DMEM
MF	DMEM
Hela	DMEM
Calu-1	RPMI

HEK 293T, MF (mouse fibroblast), HT1080 (human fibrosarcoma) cells were maintained in Dulbecco's Modified Eagle's medium containing 10% fetal bovine serum. HT1080 cells were culcured with additional 1% non-essential amino acids (NEAA). Calu-1 cells were maintained in Roswell Park Memorial Institute 1640 Medium with 15% FBS. All cells were grown in medium supplemented with 1% L-Glutamine and 1% Penicillin-Streptomycin at 37 °C in a humidified atmosphere of 5% CO2.

7.3.2 Generation of cell lines

To generate *Ms4a15* OE cell line, the respective guides were cloned into lenti-sgRNA (MS2)_Zeo (Addgene plasmid #61427) (Konermann et al., 2015) with the selection marker changed to neomycin resistance. Empty lentiviral vector was used for the corresponding control cell line. Viruses were made using third generation ecotropic packaging. Cell pool was selected for eight days with 1 mg/mL G418 Sulfate (Geneticin Selective Antibiotic,

Thermo Fisher Scientific). All lines were individually validated for survival against the three inducers from the screen and doxorubicin control as well as lipid and cytosolic ROS using BODIPY-C11 and DCF after 0.3 µM RSL3 induction for 2 h. (Kraft et al., 2019).

7.3.3 Transient transfection and viral infection

Human *MS4A15*-pCAG-IRES-Puro and *TMEM33*-pCAG-IRES-Puro expression constructs were linearized and transfected using Lipofectamine 2000 at a ratio of 1:3 (DNA:reagent) into parental Calu-1 cells. After 24h transfection, cells were used in viability assays against ferroptosis inducers. Transient, increased MSA15 and TMEM33 protein levels were verified by WB.

Third generation ecotropic lentiviruses were made using pRSV-Rev (Addgene plasmid # 12253) (Dull et al., 1998) and the respective transfer vectors. HEK293T cells were used for virus production. Cells were seeded the day before to reach 70% confluency and transfected with vector DNA mixed with XtremeGENE HP (Roche 6366244001) DNA transfection reagent in a ratio of 1:3 (DNA:reagent). Supernatant containing viral particles was collected after 72 h, filtered through a 0.45 µM syringe filter and added to recipient cells. After 48 h of infection, antibiotic selection was started to either generate pools or clones.

7.3.4 Cell viability assays

Unless indicated otherwise, $2x10^3$ MF cells or $4x10^3$ Calu-1 cells were seeded in 96-well plates and treated overnight with the respective compounds as indicated. Cell viability was assessed by the addition of Resazurin (MultiTarget Pharmaceuticals) to final concentration of 50µM and fluorescence was measured 6-8h later at 540nm excitation / 590nm emission in an Envision 2104 Multilabel plate reader (PerkinElmer). At least 3 wells per condition were averaged and all cell viability results are presented as percentage relative to the respective untreated control as mean±SD.

7.3.5 RNA-Seq and data analysis

RNA-Seq analysis was performed with independent replicates of MF *Ms4a15* OE cells and parental controls, non-strand specific, polyA-enriched RNA sequencing was performed as described earlier(Haack et al., 2013). Briefly, RNA was isolated from whole-cell lysates using InviTrap Spin Universal RNA Mini Kit (Stratec Molecular 1060100200) according to the manufacturer's instructions including a DNAse treatment step (Promega M6201).

For library preparation, 1 µg of RNA was poly(A) selected, fragmented, and reverse transcribed with the Elute, Prime, Fragment Mix (Illumina). End repair, A-tailing, adaptor ligation, and library enrichment were performed as described in the Low Throughput protocol

of the TruSeq RNA Sample Prep Guide (Illumina). RNA libraries were assessed for quality and quantity with the Agilent 2100 BioAnalyzer and the Quant-iT PicoGreen dsDNA Assay Kit (Life Technologies). RNA libraries were sequenced as 100 bp paired-end runs on an Illumina HiSeq4000 platform. The STAR aligner (Dobin et al., 2013) (v 2.4.2a) with modified parameter settings (--twopassMode=Basic) is used for split-read alignment against the human genome assembly mm9 (NCBI37) and UCSC knownGene annotation. To quantify the number of reads mapping to annotated genes, HTseq-count were used (Anders et al., 2015) (v0.6.0). FPKM (Fragments Per Kilobase of transcript per Million fragments mapped) values are calculated using custom scripts and differential gene expression analysis was performed with the R Bioconductor package DESeq2 (Love et al., 2014).

7.3.6 siRNA knockdown

$1.5x10^5$ MF cells in 2 mL medium were seeded in six well plates one day before. Before transfection, 10 nmol of siRNA and 30 µl Lipofectamine RNAiMAX Transfection Reagent was mixed and incubated at RT for 15 min, then added dropwise on top of the cells. After 48 h transfection, cells were harvested and re-seeded at a density of 2 $x10^3$ cells per well in 96-well plates for cell viability assay (see above).

Following siRNAs were used:

Table 6 siRNAs used in this work.

esiRNA	Source	Identifier
hTMEM33	Sigma	Ehu035611
mTmem33	Sigma	Emu078331
EGFP	Sigma	EHUEGFP

7.3.7 EGF signaling in cultured cells

Serum-starved MF cells were stimulated with 0-5 ng/ml EGF for 10min at 37 °C, respectively. After incubation, cells were washed with PBS and lysed in lysis buffer supplemented with protease inhibitor (as describe above) for 30 min. The lysates were stored at -20 °C for western blot.

7.3.8 High throughput screening

400 cells per well were seeded in 384-well plates in a total volume of 40 µL medium one day before. The next morning, 0.5 µL compounds were added on top of the cells. After 8h incubation with compounds, cells were treated with 10 µL RSL3 overnight resulting in the

final concentration 0.5 µM. Cell viability was measured after 16 h RSL3 treatment using 50 µM AquaBluer (See above).

For screening data analysis, row 23 (cells+RSL3+DMSO) was defined as positive control. Average of all wells of row23 was set to 100% activity. %-activity of compound was calculated: (value of compound well/average value of row23) x 100. Compounds that are marked as toxic (because of toxicity in several other screens) were excluded. Hit-threshold was calculated on plate level. Hit threshold was calculated as following: Median value of all compound-treated wells 3x Standard deviation of all compound-treated wells. A compound that has a %-activity below this value was defined as hit.

7.3.9 High-resolution high-speed time-lapse live cell imaging

For the high-throughput wound healing assay, the ibidi Culture-Inserts were used for creating the gap that two reservoirs for culturing cells were separated by a 500 µm thick wall. $8x10^3$ MF cells were seeded in each reservoir and cultured for 24 h until they attached and formed a monolayer.

The cells were imaged immediately at x20 magnification after the coverslips removed using an Operetta High-Content Screening System (PerkinElmer) equipped with digital phase contrast (DPC) for live-cell imaging. Image analysis was conducted with Harmony software (PerkinElmer). All images (8 images per well) were collected with the same instrument parameters and processed with the same settings to maximize the ability to compare results between conditions.

7.3.10 Different cell death induction

For testing the best concentration of cell death rate, HT1080 cells were treated with different drugs for 8 h and detected the viability with DAPI.

Cells were plated in 96-well plates for cell viability microscopy-based assays and the following day cells were treated with different drugs indicated below.

Table 7 Compounds for induction of cell deaths.

Compound	Source	Concentration
Cycloheximide (CHX)	Merck	50, 25, 12.5, 6.25, 3, 1.5, 0.75 µg/ml
Hydrogen Peroxide (H_2O_2)	Sigma	10%, 5%, 2.5%, 1.25%, 0.6%, 0.3%, 0.15%
Vinblastine	Sigma	10, 5, 2.5, 1.25, 0.6, 0.3, 0.15 mg/ml
6-Thioguanine (6-TG)	Sigma	10, 5, 2.5, 1.25, 0.6, 0.3, 0.15 mg/ml

Cisplatin	Sigma	250, 125, 62.5, 31.25, 15, 7.5, 3.75 mg/ml
Cytochalasin	Sigma	1, 0.5, 0.25, 0.125, 0.06, 0.03, 0.015 mg/ml
RSL3	Stockwell lab	20, 10,5, 2.5, 1.25, 0.625, 0.3 µM
IKE	Stockwell lab	20, 10,5, 2.5, 1.25, 0.625, 0.3 µM
Etoposide	J&K	100, 50, 25, 12.5, 6.25, 3, 1.5 mg/ml
Cyclophosphamide (CP)	J&K	1000, 500, 250, 125, 62.5, 31.25, 15 mg/ml
Cochicine	Serva	250, 125, 62.5, 31.25, 15, 7.5, 3.75 mg/ml

After 8 h treatment, 100 µl of 0.5 µM DAPI was added to each well and incubated for 10min at room temperature under light-shielded conditions. The plates were analyzed by high-content imaging system immediately using 350-nm excitation and 486 nm emission wavelengths for DAPI signal, digital phase contrast (DPC) was used for tracking all the cells. For further use, aspirated the DAPI solution and wash the cells two times with 100 µl PBS, after the final wash, removed the PBS and fixed the cells with 4% PFA for 10 min, added 100 µl PBS and stored in 4 °C.

The Harmony software in HCA system was utilized to measure and analyze cell viability by counting the number of both DAPI positive and negative cells. To determine cell viability, divide the number of DAPI positive by the total number of cells and multiply by 100. This value also represents overall cell death rate, choosing the drug concentrations of ~20% cell death for next experiment.

To detect the specificity of the biomarker candidates, HT1080 cells were plated the day before treatment at a density of 4000 cells/well on 96 well plates and maintained for 24 h in control conditions. Added 10 µl culture medium containing different concentrations of drugs on top of the cells to make the final concentrations below:

CHX (12.5 µg/ml), H2O2 (0.15%), Vinblastine (0.15 mg/ml), 6-TG (10 mg/ml), RSL3 (50 nM), IKE (50 nM), Etoposide (100 mg/ml), Cochicine (3.75 mg/ml), CP (31.25 mg/ml), and Cisplatin (62.5 mg/ml).

After 8 h treatment, cells were fixed with 4% PFA and used for immunofluorescence assay with high-content microscopy.

7.3.11 High-Content immunofluorescence staining

The cells were seeded on 96-well plates one day before to reach a confluency of 70%. The cells were treated with compounds indicated in the figure legends, and fixed with 4%PFA for

10 min. Washed with PBS 2 X 5 min, the cells were blocked with staining buffer at RT for 1 h, and subsequently incubated with primary antibody at 4 °C overnight.

Staining Buffer	BSA Fraction V 2,5 g
	FBS 5 ml
	Triton-X 150 µl
	1xPBS Add to 50 ml
PBS	1x
PFA in PBS	4%
DAPI/PBS	0,5 µg/ml

The next day, the cells were washed with PBS 3 X 5 min, incubated with secondary antibody for 1 h at RT. Washed with PBS; cells were stained with DAPI/PBS for high-content microscopy.

Following antibodies were used:

Primary antibodies:

Table 8 Antibodies used in immunofluorescence staining

Antibodies	**Source**	**Dilution**
Rabbit polyclonal anti-CTSV	Elabscience	1:500 in staining buffer
Rabbit polyclonal anti-CALML5	Biozol	1:500 in staining buffer
Rabbit polyclonal anti-FABP5	Cusabio	1:500 in staining buffer
Rabbit polyclonal anti-S100A14	Biozol	1:250 in staining buffer
Mouse monoclonal anti-LGALS7	R&D Systems	1:500 in staining buffer
Rabbit polyclonal WASP	Biozol	1:500 in staining buffer
Rabbit polyclonal FAK	Elabscience	1:200 in staining buffer
Rabbit polyclonal FUK	Biomol	1:200 in staining buffer
Rabbit polyclonal Cortactin	Biozol	1:500 in staining buffer
Rabbit polyclonal Phospho-FAK (Try397)	Biomol	1:200 in staining buffer

Rabbit polyclonal Phospho-CTTN (Tyr421)	Elabscience	1:300 in staining buffer
Rabbit polyclonal CLTC	Elabscience	1:500 in staining buffer
Rabbit polyclonal Phospho-WAS	Cusabio	1:500 in staining buffer

Secondary antibodies:

Antibodies	**Source**	**Dilution**
goat anti mouse Cy3	Jackson Immuno 115-165-003	1:500 in staining buffer
donkey anti goat Cy3	Jackson Immuno 705-165-147	1:500 in staining buffer
goat anti rabbit Cy3	Jackson Immuno 111-165-003	1:500 in staining buffer

7.3.12 Confocal microscopy and immunofluorescence

Calu-1 and MF cells were plated at a density of 4000 cells/well, on a glass-bottom 96-well plate (Perkin Elmer Cell Carrier Ultra Viewer). Cells were transfected 24 h before imaging using a laser scanning confocal microscope (Olympus FluoView 1200; Olympus Corporation) with a 60X 1.35 solid immersion lens oil immersion objective. Nuclei were labeled with DAPI staining (blue).

MS4A15 were visualized with Anti-Flag antibody (Sigma F7425; 1/500) and a secondary goat anti rabbit antibody (Cy3 Jackson Immuno 111-165-003; 1/500). TMEM33 were visualized with Anti-Myc tag antibody (Abcam 9E10; 1/200) and a secondary donkey anti-mouse antibody (Alexa 647 Invitrogen A-32733; 1/500). IP_3R1 were visualized with anti-IP_3R1 antibody (Biozol BLD-817701; 1/500) and a secondary donkey anti-mouse antibody (Alexa 647 Invitrogen A-32733; 1/500). ER was tracked with ER marker Concanavalin A / Alexa fluor 488 conjugate (invitrogen C11252; 100 µg / ml). Peroxisome was marked with Anti-Catalase (Abcam 89529; 1/200) and a secondary goat anti rabbit (Cy2 Jackson Immuno 111-225-003; 1/500).

7.3.12 Lipid peroxidation analysis by imaging and flow cytometry

For imaging, MF cells were plated at 4000 cells per well in a 96-well (PerkinElmer Cell Carrier Ultra Viewer) in DMEM one day before. Cells were incubated with 2 µM BODIPY-581/591 C11 (Thermo Fisher Scientific) for 1 h and the media was changed to DMEM

containing 0.5 µM RSL3 for live-cell imaging. Cells were imaged at x40 magnification using an Operetta High-Content imaging platform (PerkinElmer) equipped with Digital Phase Contrast, 488 nm and 647 nm lasers. Image analysis was conducted with Harmony software (PerkinElmer) and Fiji (Image J). All images (19 images per well) were collected with the same instrument parameters and processed with the same settings to maximize the ability to compare results between conditions.

For flow cytometry analysis, 5,000 cells per well were seeded in 96-well plates in triplicate per condition. The next day, medium was replaced with 100 µL medium containing RSL3, cells were induced with 0.3 µM RSL3 for 2 h. Subsequently, fluorescence dye to a final concentration of 2 µM BODIPY 581/591 C11 (BODIPY-C11, Thermo Fisher Scientific D3861) for lipid ROS were added on top and cells were incubated for another 30 min. After removal of the medium, wells were rinsed with 30 µL PBS before adding 30 µL Accutase (Sigma A6964) to each well. Detached cells were resuspended in 170 µL PBS per well followed by analysis on an Attune acoustic flow cytometer (Applied Biosystems). A minimum of 10,000 events per well were collected from the BL-1 channel (excited by 488 nm laser). The median fluorescence intensity of each well was determined and normalized to DMSO treated control cells using FlowJo 10 software. Each experiment was independently performed at least twice and representative experimental results are shown.

7.3.13 Intracellular calcium measurements

Cells were seeded the day before to a 10cm dish/analysis to reach 70%-80% confluency. The next day, cells were harvested and treated with indicated compounds for flow cytometry analysis. All buffers contained 125 mmol/L NaCl, 5 mmol/L KCl, 1 mmol/L MgCl2, 20 mmol/L HEPES, and the pH was adjusted to 7.4 with NaOH.

7.4 Bioinformatics

7.4.1 KEGG Calcium clustering

CTRP2.0 data were downloaded from CTD2 data-portal (Basu et al., 2013). Top 100 RSL3 resistant/sensitive cell lines are AUC v20.data.curves_post_qc.txt values.

CCLE expression data were downloaded from

https://depmap.org/portal/download/all/?release=DepMap+Public+20Q1&file=CCLE_expression_full.csv.

KEGG Calcium signaling pathway genes were downloaded from

https://www.genome.jp/dbget-bin/get_linkdb?-t+orthology+path:ko04020.

After normalization, Gene Cluster 3.0 with hierarchical clustering for cell lines was used according to Euclidean distance with complete linkage; clustering for genes used City Block clustering. Data were visualized using Java TreeView.

7.4.2 Principal component analysis

Gene expression data consists of 204 human cell lines (observations) from two different known groups (Resistant group (R) and Sensitive group (S)) described by 193 genes (variables).

Principal component analysis (PCA) were performed in R software (version 3.6.3) to visualize the clustering of the gene expression data using log-fold transcript abundance of gene arrays in each group. Variables were pretreated to eliminate redundant columns with more than 40 zero values by applying the function implemented in R/colSums(RS ==0). The following analysis was performed by variables with the highest 100 median absolute deviations (MAD). Multivariate biplot was performed to characterize the variability of the data in each group using “ggplot2” (Wickham, 2016), “factoextra” (Kassambara and Mundt, 2017), and “ade4” (Dray and Dufour, 2007) packages. Arrows show dominant clustering of variable s by groups. The distance between points approximates gene expression pattern differences among groupings. Arrows indicate top 20 genes that have greater biplot scores that drive the differences between groups. Arrowheads close to a particular group indicate genes are expressed at a greater relative abundance differences in those samples.

7.4.3 ssGSEA implementation

TCGA Lung Adenocarcinoma (LUAD) transcriptome data and clinical information were downloaded via the TCGA website. R software (version: 3.5.3) was used for all the analyses in the manuscript. The enrichment scores of the terms (GO or KEGG) were evaluated using single-sample gene set enrichment analysis (ssGSEA) (R package “GSVA” (Hänzelmann et al., 2013)).

GO_CALCIUM_ION_TRANSMEMBRANE_TRANSPORT and KEGG_CALCIUM_SIGNALING_PATHWAY term lists were derived from GSEA. The correlation between each term and gene expression level was calculated by Pearson’s test. The plots were plotted by package “ggplot2” (Wickham, 2016). Briefly, all tumor samples were centered into 40 values by their expression level of MS4A15. Each dot in the plot represents the average MS4A15 expression level of 40 tumor samples. The most significant correlation between each GO terms and MS4A15 expression was identified and plotted with R package “ggplot2” (Wickham, 2016).

The correlations between gene expression levels were calculated by Pearson's test. The 50 genes with the most significant correlation coefficients were identified from whole transcriptome. The heat map was plotted with R package "pheatmap" (Kolde and Kolde, 2015).

7.5 Statistics

Generally, statistical analyses were performed in GraphPad Prism 8.0. Individual experiments were repeated independently at least three times on different days with similar results and a representative experiment is shown. All of the statistical details of experiments can be found in the figures, figure legends and results, including the statistical tests used (* $p < 0.05$; ** $p < 0.01$; *** $p < 0.001$; ns = not significant).

8. References

Abzhanov, A., Kuo, W.P., Hartmann, C., Grant, B.R., Grant, P.R., and Tabin, C.J. (2006). The calmodulin pathway and evolution of elongated beak morphology in Darwin's finches. Nature *442*, 563-567.

Agmon, E., Solon, J., Bassereau, P., and Stockwell, B.R. (2018). Modeling the effects of lipid peroxidation during ferroptosis on membrane properties. Scientific reports *8*, 1-11.

Al-Momany, A., Li, L., Alexander, R.T., and Ballermann, B.J. (2014). Clustered PI(4,5)P₂ accumulation and ezrin phosphorylation in response to CLIC5A. *127*, 5164-5178.

Anders, S., Pyl, P.T., and Huber, W. (2015). HTSeq—a Python framework to work with high-throughput sequencing data. Bioinformatics *31*, 166-169.

Anderson, K.S., and LaBaer, J. (2005). The sentinel within: exploiting the immune system for cancer biomarkers. Journal of proteome research *4*, 1123-1133.

Arhatte, M., Gunaratne, G.S., El Boustany, C., Kuo, I.Y., Moro, C., Duprat, F., Plaisant, M., Duval, H., Li, D., Picard, N.*, et al.* (2019). TMEM33 regulates intracellular calcium homeostasis in renal tubular epithelial cells. Nat Commun *10*, 2024.

Babu, K.R., and Muckenthaler, M.U. (2016). miR-20a regulates expression of the iron exporter ferroportin in lung cancer. Journal of molecular medicine *94*, 347-359.

Basu, A., Bodycombe, N.E., Cheah, J.H., Price, E.V., Liu, K., Schaefer, G.I., Ebright, R.Y., Stewart, M.L., Ito, D., and Wang, S. (2013). An interactive resource to identify cancer genetic and lineage dependencies targeted by small molecules. Cell *154*, 1151-1161.

Basuli, D., Tesfay, L., Deng, Z., Paul, B., Yamamoto, Y., Ning, G., Xian, W., McKeon, F., Lynch, M., and Crum, C.P. (2017). Iron addiction: a novel therapeutic target in ovarian cancer. Oncogene *36*, 4089-4099.

Beers, S.A., Chan, C.H., French, R.R., Cragg, M.S., and Glennie, M.J. (2010). CD20 as a target for therapeutic type I and II monoclonal antibodies. Paper presented at: Seminars in hematology (Elsevier).

Berridge, M.J. (1995). Calcium signalling and cell proliferation. Bioessays *17*, 491-500.

Berridge, M.J., Bootman, M.D., and Roderick, H.L. (2003). Calcium signalling: dynamics, homeostasis and remodelling. Nature reviews Molecular cell biology *4*, 517-529.

Berridge, M.J., Lipp, P., and Bootman, M.D. (2000). The versatility and universality of calcium signalling. Nature reviews Molecular cell biology *1*, 11.

Biermann, J., Just, W.W., Wanders, R.J., and van den Bosch, H. (1999). Alkyl-dihydroxyacetone phosphate synthase and dihydroxyacetone phosphate acyltransferase form a protein complex in peroxisomes. European journal of biochemistry *261*, 492-499.

Bogdan, A.R., Miyazawa, M., Hashimoto, K., and Tsuji, Y. (2016). Regulators of iron homeostasis: new players in metabolism, cell death, and disease. Trends in biochemical sciences *41*, 274-286.

Braverman, N.E., and Moser, A.B. (2012). Functions of plasmalogen lipids in health and disease. Biochimica et Biophysica Acta (BBA)-Molecular Basis of Disease *1822*, 1442-1452.

Brites, P., Waterham, H.R., and Wanders, R.J. (2004). Functions and biosynthesis of plasmalogens in health and disease. Biochimica et Biophysica Acta (BBA)-Molecular and Cell Biology of Lipids *1636*, 219-231.

Brown, A.J., and Snyder, F. (1982). Alkyldihydroxyacetone-P synthase. Solubilization, partial purification, new assay method, and evidence for a ping-pong mechanism. Journal of Biological Chemistry *257*, 8835-8839.

Bruderer, R., Bernhardt, O.M., Gandhi, T., and Reiter, L. (2016). High-precision iRT prediction in the targeted analysis of data-independent acquisition and its impact on identification and quantitation. Proteomics *16*, 2246-2256.

Chavez, A., Scheiman, J., Vora, S., Pruitt, B.W., Tuttle, M., Iyer, E.P., Lin, S., Kiani, S., Guzman, C.D., and Wiegand, D.J. (2015). Highly efficient Cas9-mediated transcriptional programming. Nature methods *12*, 326-328.

Chilton, F.H., and Murphy, R.d. (1986). Remodeling of arachidonate-containing phosphoglycerides within the human neutrophil. Journal of Biological Chemistry *261*, 7771-7777.

Clapham, D.E. (2007). Calcium signaling. Cell *131*, 1047-1058.

Codenotti, S., Poli, M., Asperti, M., Zizioli, D., Marampon, F., and Fanzani, A. (2018). Cell growth potential drives ferroptosis susceptibility in rhabdomyosarcoma and myoblast cell lines. Journal of cancer research and clinical oncology *144*, 1717-1730.

Cruse, G., Kaur, D., Leyland, M., and Bradding, P. (2010). A novel FcεRIβ-chain truncation regulates human mast cell proliferation and survival. The FASEB Journal *24*, 4047-4057.

Czeredys, M., Gruszczyńska-Biegała, J., Schacht, T., Methner, A., and Kuznicki, J. (2013). Expression of genes encoding the calcium signalosome in cellular and transgenic models of Huntington's disease. Frontiers in molecular neuroscience *6*, 42.

Davis, F.M., Azimi, I., Faville, R.A., Peters, A.A., Jalink, K., Putney Jr, J.W., Goodhill, G.J., Thompson, E.W., Roberts-Thomson, S.J., and Monteith, G.R. (2014). Induction of epithelial–mesenchymal transition (EMT) in breast cancer cells is calcium signal dependent. Oncogene *33*, 2307.

Deans, J.P., Li, H., and Polyak, M.J. (2002). CD20-mediated apoptosis: signalling through lipid rafts. Immunology *107*, 176-182.

Demers, M., Rose, A.A., Grosset, A.-A., Biron-Pain, K., Gaboury, L., Siegel, P.M., and St-Pierre, Y. (2010). Overexpression of galectin-7, a myoepithelial cell marker, enhances spontaneous metastasis of breast cancer cells. The American journal of pathology *176*, 3023-3031.

Di Fonzo, A., Ronchi, D., Gallia, F., Cribiù, F.M., Trezzi, I., Vetro, A., Della Mina, E., Limongelli, I., Bellazzi, R., and Ricca, I. (2014). Lower motor neuron disease with respiratory failure caused by a novel MAPT mutation. Neurology *82*, 1990-1998.

Dixon, S.J., Lemberg, K.M., Lamprecht, M.R., Skouta, R., Zaitsev, E.M., Gleason, C.E., Patel, D.N., Bauer, A.J., Cantley, A.M., Yang, W.S.*, et al.* (2012). Ferroptosis: an iron-dependent form of nonapoptotic cell death. Cell *149*, 1060-1072.

Dixon, S.J., Winter, G.E., Musavi, L.S., Lee, E.D., Snijder, B., Rebsamen, M., Superti-Furga, G., and Stockwell, B.R. (2015). Human haploid cell genetics reveals roles for lipid metabolism genes in nonapoptotic cell death. ACS chemical biology *10*, 1604-1609.

Do Van, B., Gouel, F., Jonneaux, A., Timmerman, K., Gele, P., Petrault, M., Bastide, M., Laloux, C., Moreau, C., and Bordet, R. (2016). Ferroptosis, a newly characterized form of cell death in Parkinson's disease that is regulated by PKC. Neurobiology of disease *94*, 169-178.

Dobin, A., Davis, C.A., Schlesinger, F., Drenkow, J., Zaleski, C., Jha, S., Batut, P., Chaisson, M., and Gingeras, T.R. (2013). STAR: ultrafast universal RNA-seq aligner. Bioinformatics *29*, 15-21.

Doll, S., Proneth, B., Tyurina, Y.Y., Panzilius, E., Kobayashi, S., Ingold, I., Irmler, M., Beckers, J., Aichler, M., and Walch, A. (2017). ACSL4 dictates ferroptosis sensitivity by shaping cellular lipid composition. Nature chemical biology *13*, 91.

Donnadieu, E., Jouvin, M.-H., Rana, S., Moffatt, M.F., Mockford, E.H., Cookson, W.O., and Kinet, J.-P. (2003). Competing functions encoded in the allergy-associated FcεRIβ gene. Immunity *18*, 665-674.

Dray, S., and Dufour, A.-B. (2007). The ade4 package: implementing the duality diagram for ecologists. Journal of statistical software *22*, 1-20.

Dyall, S., and Michael-Titus, A. (2008). Neurological benefits of omega-3 fatty acids. Neuromolecular medicine *10*, 219-235.

Ehmsen, S., Hansen, L.T., Bak, M., Brasch-Andersen, C., Ditzel, H.J., and Leth-Larsen, R. (2015). S 100A14 is a novel independent prognostic biomarker in the triple-negative breast cancer subtype. International journal of cancer *137*, 2093-2103.

Eisen, M.B., Spellman, P.T., Brown, P.O., and Botstein, D. (1998). Cluster analysis and display of genome-wide expression patterns. Proceedings of the National Academy of Sciences *95*, 14863-14868.

Eon Kuek, L., Leffler, M., Mackay, G.A., and Hulett, M.D. (2016). The MS4A family: counting past 1, 2 and 3. Immunology and cell biology *94*, 11-23.

Fawcett, J., and Pawson, T. (2000). N-WASP Regulation--the Sting in the Tail. Science *290*, 725-726.

Feldner, J.C., and Brandt, B.H. (2002). Cancer cell motility--on the road from c-erbB-2 receptor steered signaling to actin reorganization. Experimental cell research *272*, 93-108.

Frazer, D.M., and Anderson, G.J. (2014). The regulation of iron transport. Biofactors *40*, 206-214.

Fuchs, Y., and Steller, H. (2011). Programmed cell death in animal development and disease. Cell *147*, 742-758.

Fujita, K., Kume, H., Matsuzaki, K., Kawashima, A., Ujike, T., Nagahara, A., Uemura, M., Miyagawa, Y., Tomonaga, T., and Nonomura, N. (2017). FABP5 in urinary extracellular vesicles is a potential biomarker of high Gleason score prostate cancer (AACR).

Furuhashi, M., Ogura, M., Matsumoto, M., Yuda, S., Muranaka, A., Kawamukai, M., Omori, A., Tanaka, M., Moniwa, N., and Ohnishi, H. (2017). Serum FABP5 concentration is a potential biomarker for residual risk of atherosclerosis in relation to cholesterol efflux from macrophages. Scientific reports *7*, 1-10.

Galluzzi, L., Vitale, I., Abrams, J., Alnemri, E., Baehrecke, E., Blagosklonny, M., Dawson, T.M., Dawson, V., El-Deiry, W., and Fulda, S. (2012). Molecular definitions of cell death subroutines: recommendations of the Nomenclature Committee on Cell Death 2012. Cell death and differentiation *19*, 107.

Gao, M., Monian, P., Quadri, N., Ramasamy, R., and Jiang, X. (2015). Glutaminolysis and transferrin regulate ferroptosis. Molecular cell *59*, 298-308.

Gaschler, M.M., Andia, A.A., Liu, H., Csuka, J.M., Hurlocker, B., Vaiana, C.A., Heindel, D.W., Zuckerman, D.S., Bos, P.H., and Reznik, E. (2018). FINO 2 initiates ferroptosis through GPX4 inactivation and iron oxidation. Nature chemical biology *14*, 507-515.

Gaschler, M.M., and Stockwell, B.R. (2017). Lipid peroxidation in cell death. Biochemical and biophysical research communications *482*, 419-425.

Ghosh, D., Levault, K.R., and Brewer, G.J. (2014). Relative importance of redox buffers GSH and NAD (P) H in age-related neurodegeneration and Alzheimer disease-like mouse neurons. Aging cell *13*, 631-640.

Greer, P.L., Bear, D.M., Lassance, J.-M., Bloom, M.L., Tsukahara, T., Pashkovski, S.L., Masuda, F.K., Nowlan, A.C., Kirchner, R., and Hoekstra, H.E. (2016). A family of non-GPCR chemosensors defines an alternative logic for mammalian olfaction. Cell *165*, 1734-1748.

Guo, L., Nakamura, K., Lynch, J., Opas, M., Olson, E.N., Agellon, L.B., and Michalak, M. (2002). Cardiac-specific expression of calcineurin reverses embryonic lethality in calreticulin-deficient mouse. The Journal of biological chemistry *277*, 50776-50779.

Haack, T.B., Kopajtich, R., Freisinger, P., Wieland, T., Rorbach, J., Nicholls, T.J., Baruffini, E., Walther, A., Danhauser, K., and Zimmermann, F.A. (2013). ELAC2 mutations cause a mitochondrial RNA processing defect associated with hypertrophic cardiomyopathy. The American Journal of Human Genetics *93*, 211-223.

Hänzelmann, S., Castelo, R., and Guinney, J. (2013). GSVA: gene set variation analysis for microarray and RNA-seq data. BMC bioinformatics *14*, 7.

Hartmann, A., and Hirsch, E.C. (2001). Parkinson's disease. The apoptosis hypothesis revisited. Advances in neurology *86*, 143-153.

Hayano, M., Yang, W., Corn, C., Pagano, N., and Stockwell, B. (2016). Loss of cysteinyl-tRNA synthetase (CARS) induces the transsulfuration pathway and inhibits ferroptosis induced by cystine deprivation. Cell Death & Differentiation *23*, 270-278.

Henke, N., Albrecht, P., Bouchachia, I., Ryazantseva, M., Knoll, K., Lewerenz, J., Kaznacheyeva, E., Maher, P., and Methner, A. (2013). The plasma membrane channel ORAI1 mediates detrimental calcium influx caused by endogenous oxidative stress. Cell death & disease *4*, e470-e470.

Henke, N., Albrecht, P., Pfeiffer, A., Toutzaris, D., Zanger, K., and Methner, A. (2012). Stromal interaction molecule 1 (STIM1) is involved in the regulation of mitochondrial shape and bioenergetics and plays a role in oxidative stress. Journal of Biological Chemistry *287*, 42042-42052.

Hermetter, A., Rainer, B., Ivessa, E., Kalb, E., Loidl, J., Roscher, A., and Paltauf, F. (1989). Influence of plasmalogen deficiency on membrane fluidity of human skin fibroblasts: a fluorescence anisotropy study. Biochimica et Biophysica Acta (BBA)-Biomembranes *978*, 151-157.

Higgins, E.R., Cannell, M.B., and Sneyd, J. (2006). A buffering SERCA pump in models of calcium dynamics. Biophysical journal *91*, 151-163.

Honsho, M., Asaoku, S., and Fujiki, Y. (2010). Posttranslational regulation of fatty acyl-CoA reductase 1, Far1, controls ether glycerophospholipid synthesis. Journal of Biological Chemistry *285*, 8537-8542.

Hopkins, A.L., and Groom, C.R. (2002). The druggable genome. Nature reviews Drug discovery *1*, 727-730.

Hoth, M., and Penner, R. (1992). Depletion of intracellular calcium stores activates a calcium current in mast cells. Nature *355*, 353-356.

Hwang, J., Kalinin, A., Hwang, M., Anderson, D.E., Kim, M.J., Stojadinovic, O., Tomic-Canic, M., Lee, S.H., and Morasso, M.I. (2007). Role of Scarf and its binding target proteins in epidermal calcium homeostasis. Journal of Biological Chemistry *282*, 18645-18653.

Jain, M., Nilsson, R., Sharma, S., Madhusudhan, N., Kitami, T., Souza, A.L., Kafri, R., Kirschner, M.W., Clish, C.B., and Mootha, V.K. (2012). Metabolite profiling identifies a key role for glycine in rapid cancer cell proliferation. Science *336*, 1040-1044.

Kagan, V.E., Mao, G., Qu, F., Angeli, J.P.F., Doll, S., St Croix, C., Dar, H.H., Liu, B., Tyurin, V.A., and Ritov, V.B. (2017). Oxidized arachidonic and adrenic PEs navigate cells to ferroptosis. Nature chemical biology *13*, 81.

Kang, Y., Tiziani, S., Park, G., Kaul, M., and Paternostro, G. (2014a). Cellular protection using Flt3 and PI3Kalpha inhibitors demonstrates multiple mechanisms of oxidative glutamate toxicity. Nat Commun *5*, 3672.

Kang, Y., Tiziani, S., Park, G., Kaul, M., and Paternostro, G. (2014b). Cellular protection using Flt3 and PI3Kα inhibitors demonstrates multiple mechanisms of oxidative glutamate toxicity. Nature communications *5*, 1-12.

Kassambara, A., and Mundt, F. (2017). Package 'factoextra'. Extract and visualize the results of multivariate data analyses *76*.

Kim, E.K., Ha, J.M., Kim, Y.W., Jin, S.Y., Ha, H.K., and Bae, S.S. (2014). Inhibitory role of polyunsaturated fatty acids on lysophosphatidic acid-induced cancer cell migration and adhesion. FEBS letters *588*, 2971-2977.

Kindrat, I., Tryndyak, V., de Conti, A., Shpyleva, S., Mudalige, T.K., Kobets, T., Erstenyuk, A.M., Beland, F.A., and Pogribny, I.P. (2016). MicroRNA-152-mediated dysregulation of hepatic transferrin receptor 1 in liver carcinogenesis. Oncotarget *7*, 1276.

Kohn, E.C., Reed, E., Sarosy, G., Christian, M., Link, C.J., Cole, K., Figg, W.D., Davis, P.A., Jacob, J., and Goldspiel, B. (1996). Clinical investigation of a cytostatic calcium influx inhibitor in patients with refractory cancers. Cancer research *56*, 569-573.

Kolde, R., and Kolde, M.R. (2015). Package 'pheatmap'. R Package *1*.

Konermann, S., Brigham, M.D., Trevino, A.E., Joung, J., Abudayyeh, O.O., Barcena, C., Hsu, P.D., Habib, N., Gootenberg, J.S., and Nishimasu, H. (2015). Genome-scale transcriptional activation by an engineered CRISPR-Cas9 complex. Nature *517*, 583.

Koslowski, M., Sahin, U., Dhaene, K., Huber, C., and Tureci, O. (2008). MS4A12 is a colon-selective store-operated calcium channel promoting malignant cell processes. Cancer research *68*, 3458-3466.

Kraft, V.A., Bezjian, C.T., Pfeiffer, S., Ringelstetter, L., Müller, C., Zandkarimi, F., Merl-Pham, J., Bao, X., Anastasov, N., and Kössl, J. (2019). GTP Cyclohydrolase 1/Tetrahydrobiopterin Counteract Ferroptosis through Lipid Remodeling. ACS Central Science.

Kroemer, G., El-Deiry, W., Golstein, P., Peter, M., Vaux, D., Vandenabeele, P., Zhivotovsky, B., Blagosklonny, M., Malorni, W., and Knight, R. (2005). Classification of cell death: recommendations of the Nomenclature Committee on Cell Death. Cell death and differentiation *12*, 1463-1467.

Kryukov, G.V., Castellano, S., Novoselov, S.V., Lobanov, A.V., Zehtab, O., Guigó, R., and Gladyshev, V.N. (2003). Characterization of mammalian selenoproteomes. Science *300*, 1439-1443.

Kuchay, S., Giorgi, C., Simoneschi, D., Pagan, J., Missiroli, S., Saraf, A., Florens, L., Washburn, M.P., Collazo-Lorduy, A., Castillo-Martin, M.*, et al.* (2017). PTEN counteracts FBXL2 to promote IP3R3- and Ca(2+)-mediated apoptosis limiting tumour growth. Nature *546*, 554-558.

Kunzelmann, K., and Mehta, A. (2013). CFTR: a hub for kinases and crosstalk of cAMP and Ca2+. The FEBS journal *280*, 4417-4429.

Kutok, J.L., Yang, X., Folkerth, R., and Adra, C.N. (2011). Characterization of the expression of HTm4 (MS4A3), a cell cycle regulator, in human peripheral blood cells and normal and malignant tissues. Journal of cellular and molecular medicine *15*, 86-93.

Kwan, J.Y., Jeong, S.Y., Van Gelderen, P., Deng, H.-X., Quezado, M.M., Danielian, L.E., Butman, J.A., Chen, L., Bayat, E., and Russell, J. (2012). Iron accumulation in deep cortical layers accounts for MRI signal abnormalities in ALS: correlating 7 tesla MRI and pathology. PloS one *7*, e35241.

Kwon, M.-Y., Park, E., Lee, S.-J., and Chung, S.W. (2015). Heme oxygenase-1 accelerates erastin-induced ferroptotic cell death. Oncotarget *6*, 24393.

Landshamer, S., Hoehn, M., Barth, N., Duvezin-Caubet, S., Schwake, G., Tobaben, S., Kazhdan, I., Becattini, B., Zahler, S., and Vollmar, A. (2008). Bid-induced release of AIF from mitochondria causes immediate neuronal cell death. Cell Death & Differentiation *15*, 1553-1563.

Lassmann, H., Bancher, C., Breitschopf, H., Wegiel, J., Bobinski, M., Jellinger, K., and Wisniewski, H.M. (1995). Cell death in Alzheimer's disease evaluated by DNA fragmentation in situ. Acta neuropathologica *89*, 35-41.

Lewerenz, J., Ates, G., Methner, A., Conrad, M., and Maher, P. (2018). Oxytosis/Ferroptosis-(Re-) Emerging Roles for Oxidative Stress-Dependent Non-apoptotic Cell Death in Diseases of the Central Nervous System. Frontiers in neuroscience *12*, 214.

Lewerenz, J., Hewett, S.J., Huang, Y., Lambros, M., Gout, P.W., Kalivas, P.W., Massie, A., Smolders, I., Methner, A., and Pergande, M. (2013). The cystine/glutamate antiporter system xc– in health and disease: from molecular mechanisms to novel therapeutic opportunities. Antioxidants & redox signaling *18*, 522-555.

Li, J., Cao, F., Yin, H.-l., Huang, Z.-j., Lin, Z.-t., Mao, N., Sun, B., and Wang, G. (2020). Ferroptosis: past, present and future. Cell Death & Disease *11*, 1-13.

Li, J., Su, J., Li, W., Liu, W., Altura, B.T., and Altura, B.M. (2003). Peroxynitrite induces apoptosis in canine cerebral vascular muscle cells: possible relation to neurodegenerative diseases and strokes. Neuroscience letters *350*, 173-177.

Li, Y., Maher, P., and Schubert, D. (1997). A role for 12-lipoxygenase in nerve cell death caused by glutathione depletion. Neuron *19*, 453-463.

Liu, Y., and Schubert, D.R. (2009). The specificity of neuroprotection by antioxidants. Journal of biomedical science *16*, 98.

Love, M.I., Huber, W., and Anders, S. (2014). Moderated estimation of fold change and dispersion for RNA-seq data with DESeq2. Genome biology *15*, 550.

Luo, Y., and DeFranco, D.B. (2006). Opposing Roles for ERK1/2 in Neuronal Oxidative Toxicity DISTINCT MECHANISMS OF ERK1/2 ACTION AT EARLY VERSUS LATE PHASES OF OXIDATIVE STRESS. Journal of Biological Chemistry *281*, 16436-16442.

Lv, Q., Wang, G., Zhang, Y., Han, X., Li, H., Le, W., Zhang, M., Ma, C., Wang, P., and Ding, Q. (2019). FABP5 regulates the proliferation of clear cell renal cell carcinoma cells via the PI3K/AKT signaling pathway. International journal of oncology *54*, 1221-1232.

Maeder, M.L., Linder, S.J., Cascio, V.M., Fu, Y., Ho, Q.H., and Joung, J.K. (2013). CRISPR RNA–guided activation of endogenous human genes. Nature methods *10*, 977-979.

Magtanong, L., Ko, P.-J., To, M., Cao, J.Y., Forcina, G.C., Tarangelo, A., Ward, C.C., Cho, K., Patti, G.J., and Nomura, D.K.J.C.c.b. (2019). Exogenous monounsaturated fatty acids promote a ferroptosis-resistant cell state. *26*, 420-432. e429.

Magtanong, L., Ko, P., and Dixon, S. (2016). Emerging roles for lipids in non-apoptotic cell death. Cell Death & Differentiation *23*, 1099-1109.

Maher, P., and Kontoghiorghes, G.J. (2015). Characterization of the neuroprotective potential of derivatives of the iron chelating drug deferiprone. Neurochemical research *40*, 609-620.

Maher, P., van Leyen, K., Dey, P.N., Honrath, B., Dolga, A., and Methner, A. (2018a). The role of Ca2+ in cell death caused by oxidative glutamate toxicity and ferroptosis. Cell Calcium *70*, 47-55.

Maher, P., van Leyen, K., Dey, P.N., Honrath, B., Dolga, A., and Methner, A. (2018b). The role of Ca(2+) in cell death caused by oxidative glutamate toxicity and ferroptosis. Cell calcium *70*, 47-55.

Mak, I.T., Boehme, P., and Weglicki, W.B. (1992). Antioxidant effects of calcium channel blockers against free radical injury in endothelial cells. Correlation of protection with preservation of glutathione levels. Circulation research *70*, 1099-1103.

Mali, P., Aach, J., Stranges, P.B., Esvelt, K.M., Moosburner, M., Kosuri, S., Yang, L., and Church, G.M. (2013). CAS9 transcriptional activators for target specificity screening and paired nickases for cooperative genome engineering. Nature biotechnology *31*, 833.

Mason, R.P., Mak, I.T., Trumbore, M.W., and Mason, P.E. (1999a). Antioxidant properties of calcium antagonists related to membrane biophysical interactions. The American journal of cardiology *84*, 16-22.

Mason, R.P., Walter, M.F., Trumbore, M.W., Olmstead Jr, E.G., and Mason, P.E. (1999b). Membrane antioxidant effects of the charged dihydropyridine calcium antagonist amlodipine. Journal of molecular and cellular cardiology *31*, 275-281.

McBean, G.J. (2012). The transsulfuration pathway: a source of cysteine for glutathione in astrocytes. Amino acids *42*, 199-205.

Méhul, B., Bernard, D., Brouard, M., Delattre, C., and Schmidt, R. (2006). Influence of calcium on the proteolytic degradation of the calmodulin-like skin protein (calmodulin-like protein 5) in psoriatic epidermis. Experimental dermatology *15*, 469-477.

Michell, R.H., Kirk, C., Jones, L.M., Downes, C., and Creba, J.A. (1981). The stimulation of inositol lipid metabolism that accompanies calcium mobilization in stimulated cells: defined characteristics and unanswered questions. Philosophical Transactions of the Royal Society of London B, Biological Sciences *296*, 123-138.

Mohamed, B.F., Serag, W.M., Abdelal, R.M., and Elsergany, H.F. (2019). S100A14 protein as diagnostic and prognostic marker in hepatocellular carcinoma. Egyptian Liver Journal *9*, 1-6.

Murphy, T.H., Miyamoto, M., Sastre, A., Schnaar, R.L., and Coyle, J.T. (1989). Glutamate toxicity in a neuronal cell line involves inhibition of cystine transport leading to oxidative stress. Neuron *2*, 1547-1558.

Nakagawa, Y., and Waku, K. (1989). The metabolism of glycerophospholipid and its regulation in monocytes and macrophages. Progress in lipid research *28*, 205-243.

Noda, S., Asano, Y., Takahashi, T., Akamata, K., Aozasa, N., Taniguchi, T., Ichimura, Y., Toyama, T., Sumida, H., and Kuwano, Y. (2013). Decreased cathepsin V expression due to Fli1 deficiency contributes to the development of dermal fibrosis and proliferative vasculopathy in systemic sclerosis. Rheumatology *52*, 790-799.

Ou, Y., Wang, S.-J., Li, D., Chu, B., and Gu, W. (2016). Activation of SAT1 engages polyamine metabolism with p53-mediated ferroptotic responses. Proceedings of the National Academy of Sciences *113*, E6806-E6812.

Overington, J.P., Al-Lazikani, B., and Hopkins, A.L. (2006). How many drug targets are there? Nature reviews Drug discovery *5*, 993-996.

Parkash, J., and Asotra, K. (2010). Calcium wave signaling in cancer cells. Life sciences *87*, 587-595.

Pearce, M.M., Wormer, D.B., Wilkens, S., and Wojcikiewicz, R.J. (2009). An endoplasmic reticulum (ER) membrane complex composed of SPFH1 and SPFH2 mediates the ER-associated degradation of inositol 1,4,5-trisphosphate receptors. The Journal of biological chemistry *284*, 10433-10445.

Perez-Riverol, Y., Csordas, A., Bai, J., Bernal-Llinares, M., Hewapathirana, S., Kundu, D.J., Inuganti, A., Griss, J., Mayer, G., and Eisenacher, M. (2019). The PRIDE database and related tools and resources in 2019: improving support for quantification data. Nucleic acids research *47*, D442-D450.

Poursaitidis, I., Wang, X., Crighton, T., Labuschagne, C., Mason, D., Cramer, S.L., Triplett, K., Roy, R., Pardo, O.E., and Seckl, M.J. (2017). Oncogene-selective sensitivity to synchronous cell death following modulation of the amino acid nutrient cystine. Cell reports *18*, 2547-2556.

Ravid, A., and Koren, R. (2003). The role of reactive oxygen species in the anticancer activity of vitamin D. In Vitamin D Analogs in Cancer Prevention and Therapy (Springer), pp. 357-367.

Ron, D., and Walter, P. (2007). Signal integration in the endoplasmic reticulum unfolded protein response. Nature reviews Molecular cell biology *8*, 519-529.

Sangokoya, C., Doss, J.F., and Chi, J.-T. (2013). Iron-responsive miR-485-3p regulates cellular iron homeostasis by targeting ferroportin. PLoS genetics *9*.

Savage, A.M., Kurusamy, S., Chen, Y., Jiang, Z., Chhabria, K., MacDonald, R.B., Kim, H.R., Wilson, H.L., van Eeden, F.J., and Armesilla, A.L. (2019). tmem33 is essential for VEGF-mediated endothelial calcium oscillations and angiogenesis. Nature communications *10*, 732.

Schöndorf, D.C., Aureli, M., McAllister, F.E., Hindley, C.J., Mayer, F., Schmid, B., Sardi, S.P., Valsecchi, M., Hoffmann, S., and Schwarz, L.K. (2014). iPSC-derived neurons from GBA1-associated Parkinson's disease patients show autophagic defects and impaired calcium homeostasis. Nature communications *5*, 4028.

Seiler, A., Schneider, M., Förster, H., Roth, S., Wirth, E.K., Culmsee, C., Plesnila, N., Kremmer, E., Rådmark, O., and Wurst, W. (2008). Glutathione peroxidase 4 senses and translates oxidative stress into 12/15-lipoxygenase dependent-and AIF-mediated cell death. Cell metabolism *8*, 237-248.

Sergeev, I.N. (2005). Calcium signaling in cancer and vitamin D. The Journal of steroid biochemistry and molecular biology *97*, 145-151.

Shan, D., Ledbetter, J.A., and Press, O.W. (2000). Signaling events involved in anti-CD20-induced apoptosis of malignant human B cells. Cancer immunology, immunotherapy *48*, 673-683.

Shang, J., Song, Q., Yang, Z., Li, D., Chen, W., Luo, L., Wang, Y., Yang, J., and Li, S. (2017). Identification of lung adenocarcinoma specific dysregulated genes with diagnostic and prognostic value across 27 TCGA cancer types. Oncotarget *8*, 87292.

Shen, Y., Meunier, L., and Hendershot, L.M. (2002). Identification and characterization of a novel endoplasmic reticulum (ER) DnaJ homologue, which stimulates ATPase activity of BiP in vitro and is induced by ER stress. Journal of Biological Chemistry *277*, 15947-15956.

Shimada, K., Skouta, R., Kaplan, A., Yang, W.S., Hayano, M., Dixon, S.J., Brown, L.M., Valenzuela, C.A., Wolpaw, A.J., and Stockwell, B.R. (2016). Global survey of cell death mechanisms reveals metabolic regulation of ferroptosis. Nat Chem Biol *12*, 497-503.

Simpson, K.L., Cawthorne, C., Zhou, C., Hodgkinson, C.L., Walker, M.J., Trapani, F., Kadirvel, M., Brown, G., Dawson, M., and MacFarlane, M. (2013). A caspase-3 'death-switch'in colorectal cancer cells for induced and synchronous tumor apoptosis in vitro and in vivo facilitates the development of minimally invasive cell death biomarkers. Cell death & disease *4*, e613-e613.

Singh, K.P., Jaffe, A.S., and Liang, B.T. (2011). The clinical impact of circulating caspase-3 p17 level: a potential new biomarker for myocardial injury and cardiovascular disease. Future cardiology *7*, 443-445.

Skonieczna, M., Cieslar-Pobuda, A., Saenko, Y., Foksinski, M., Olinski, R., Rzeszowska-Wolny, J., and Wiechec, E. (2017). The impact of DIDS-induced inhibition of voltage-dependent anion channels (VDAC) on cellular response of lymphoblastoid cells to ionizing radiation. Medicinal Chemistry *13*, 477-483.

Skouta, R., Dixon, S.J., Wang, J., Dunn, D.E., Orman, M., Shimada, K., Rosenberg, P.A., Lo, D.C., Weinberg, J.M., and Linkermann, A. (2014). Ferrostatins inhibit oxidative lipid damage and cell death in diverse disease models. Journal of the American Chemical Society *136*, 4551-4556.

Small, D.H. (2009). Dysregulation of calcium homeostasis in Alzheimer's disease. Neurochemical research *34*, 1824-1829.

Stewart, T.A., Yapa, K.T., and Monteith, G.R. (2015). Altered calcium signaling in cancer cells. Biochimica et Biophysica Acta (BBA)-Biomembranes *1848*, 2502-2511.

Stockwell, B.R., Angeli, J.P.F., Bayir, H., Bush, A.I., Conrad, M., Dixon, S.J., Fulda, S., Gascón, S., Hatzios, S.K., and Kagan, V.E. (2017). Ferroptosis: a regulated cell death nexus linking metabolism, redox biology, and disease. Cell *171*, 273-285.

Su, L., Jiang, X., Yang, C., Zhang, J., Chen, B., Li, Y., Yao, S., Xie, Q., Gomez, H., and Murugan, R. (2019). Pannexin 1 mediates ferroptosis that contributes to renal ischemia/reperfusion injury. Journal of Biological Chemistry *294*, 19395-19404.

Sun, B.K., Boxer, L.D., Ransohoff, J.D., Siprashvili, Z., Qu, K., Lopez-Pajares, V., Hollmig, S.T., and Khavari, P.A. (2015a). CALML5 is a ZNF750-and TINCR-induced protein that binds stratifin to regulate epidermal differentiation. Genes & development *29*, 2225-2230.

Sun, X., Ou, Z., Xie, M., Kang, R., Fan, Y., Niu, X., Wang, H., Cao, L., and Tang, D. (2015b). HSPB1 as a novel regulator of ferroptotic cancer cell death. Oncogene *34*, 5617-5625.

Tan, S., Sagara, Y., Liu, Y., Maher, P., and Schubert, D. (1998). The regulation of reactive oxygen species production during programmed cell death. The Journal of cell biology *141*, 1423-1432.

Tan, S., Schubert, D., and Maher, P. (2001). Oxytosis: a novel form of programmed cell death. Current topics in medicinal chemistry *1*, 497-506.

Tarangelo, A., Magtanong, L., Bieging-Rolett, K.T., Li, Y., Ye, J., Attardi, L.D., and Dixon, S.J. (2018). p53 suppresses metabolic stress-induced ferroptosis in cancer cells. Cell reports *22*, 569-575.

TCGA The results shown here are in whole or part based upon data generated by the TCGA Research Network

Tonutti, L., Manzi, L., Tacconi, M.T., and Bazzoni, G. (2010). Eicosapentaenoic acid inhibits endothelial cell migration in vitro. Journal of angiogenesis research *2*, 12.

Tuo, Q., Lei, P., Jackman, K., Li, X., Xiong, H., Liuyang, Z., Roisman, L., Zhang, S., Ayton, S., and Wang, Q. (2017). Tau-mediated iron export prevents ferroptotic damage after ischemic stroke. Molecular psychiatry *22*, 1520.

Turmaine, M., Raza, A., Mahal, A., Mangiarini, L., Bates, G.P., and Davies, S.W. (2000). Nonapoptotic neurodegeneration in a transgenic mouse model of Huntington's disease. Proceedings of the National Academy of Sciences *97*, 8093-8097.

Uhlen, M., Zhang, C., Lee, S., Sjostedt, E., Fagerberg, L., Bidkhori, G., Benfeitas, R., Arif, M., Liu, Z., Edfors, F.*, et al.* (2017). A pathology atlas of the human cancer transcriptome. Science *357*.

Viswanathan, V.S., Ryan, M.J., Dhruv, H.D., Gill, S., Eichhoff, O.M., Seashore-Ludlow, B., Kaffenberger, S.D., Eaton, J.K., Shimada, K., and Aguirre, A.J. (2017). Dependency of a therapy-resistant state of cancer cells on a lipid peroxidase pathway. Nature *547*, 453-457.

Wang, W., Chu, H.-j., Liang, Y.-c., Huang, J.-m., Shang, C.-l., Tan, H., Liu, D., Zhao, Y.-h., Liu, T.-y., and Yao, S.-z. (2016). FABP5 correlates with poor prognosis and promotes tumor cell growth and metastasis in cervical cancer. Tumor Biology *37*, 14873-14883.

Warner, G.J., Berry, M.J., Moustafa, M.E., Carlson, B.A., Hatfield, D.L., and Faust, J.R. (2000). Inhibition of selenoprotein synthesis by selenocysteine tRNA [Ser] Sec lacking isopentenyladenosine. Journal of Biological Chemistry *275*, 28110-28119.

Weitsman, G.E., Koren, R., Zuck, E., Rotem, C., Liberman, U.A., and Ravid, A. (2005). Vitamin D sensitizes breast cancer cells to the action of H2O2: mitochondria as a convergence point in the death pathway. Free Radical Biology and Medicine *39*, 266-278.

Wenzel, S.E., Tyurina, Y.Y., Zhao, J., Croix, C.M.S., Dar, H.H., Mao, G., Tyurin, V.A., Anthonymuthu, T.S., Kapralov, A.A., and Amoscato, A.A. (2017). PEBP1 wardens ferroptosis by enabling lipoxygenase generation of lipid death signals. Cell *171*, 628-641. e626.

Wickham, H. (2016). ggplot2: elegant graphics for data analysis (Springer).

Wright, F., and Wojcikiewicz, R. (2016). Inositol 1, 4, 5-trisphosphate receptor ubiquitination. In Progress in molecular biology and translational science (Elsevier), pp. 141-159.

Wright, F.A., Bonzerato, C.G., Sliter, D.A., and Wojcikiewicz, R.J. (2018). The erlin2 T65I mutation inhibits erlin1/2 complex–mediated inositol 1, 4, 5-trisphosphate receptor ubiquitination and phosphatidylinositol 3-phosphate binding. Journal of Biological Chemistry *293*, 15706-15714.

Wu, J., Minikes, A.M., Gao, M., Bian, H., Li, Y., Stockwell, B.R., Chen, Z.-N., and Jiang, X. (2019). Intercellular interaction dictates cancer cell ferroptosis via NF2–YAP signalling. Nature *572*, 402-406.

Xie, Y., Hou, W., Song, X., Yu, Y., Huang, J., Sun, X., Kang, R., and Tang, D. (2016). Ferroptosis: process and function. Cell death and differentiation *23*, 369.

Xie, Y., Zhu, S., Song, X., Sun, X., Fan, Y., Liu, J., Zhong, M., Yuan, H., Zhang, L., and Billiar, T.R. (2017). The tumor suppressor p53 limits ferroptosis by blocking DPP4 activity. Cell reports *20*, 1692-1704.

Yagoda, N., Von Rechenberg, M., Zaganjor, E., Bauer, A.J., Yang, W.S., Fridman, D.J., Wolpaw, A.J., Smukste, I., Peltier, J.M., and Boniface, J.J. (2007). RAS–RAF–MEK-dependent oxidative cell death involving voltage-dependent anion channels. Nature *447*, 865-869.

Yamashita, A., Hayashi, Y., Matsumoto, N., Nemoto-Sasaki, Y., Koizumi, T., Inagaki, Y., Oka, S., Tanikawa, T., and Sugiura, T. (2017). Coenzyme-A-independent transacylation system; possible involvement of phospholipase A2 in transacylation. Biology *6*, 23.

Yang, W.S., Kim, K.J., Gaschler, M.M., Patel, M., Shchepinov, M.S., and Stockwell, B.R. (2016). Peroxidation of polyunsaturated fatty acids by lipoxygenases drives ferroptosis. Proceedings of the National Academy of Sciences *113*, E4966-E4975.

Yang, W.S., SriRamaratnam, R., Welsch, M.E., Shimada, K., Skouta, R., Viswanathan, V.S., Cheah, J.H., Clemons, P.A., Shamji, A.F., and Clish, C.B. (2014a). Regulation of ferroptotic cancer cell death by GPX4. Cell *156*, 317-331.

Yang, W.S., SriRamaratnam, R., Welsch, M.E., Shimada, K., Skouta, R., Viswanathan, V.S., Cheah, J.H., Clemons, P.A., Shamji, A.F., Clish, C.B.*, et al.* (2014b). Regulation of ferroptotic cancer cell death by GPX4. Cell *156*, 317-331.

Yang, W.S., and Stockwell, B.R. (2008). Synthetic lethal screening identifies compounds activating iron-dependent, nonapoptotic cell death in oncogenic-RAS-harboring cancer cells. Chemistry & biology *15*, 234-245.

Yoshioka, Y., Kosaka, N., Ochiya, T., and Kato, T. (2012). Micromanaging iron homeostasis hypoxia-inducible micro-rna-210 suppresses iron homeostasis-related proteins. Journal of Biological Chemistry *287*, 34110-34119.

Yu, Y., Xie, Y., Cao, L., Yang, L., Yang, M., Lotze, M.T., Zeh, H.J., Kang, R., and Tang, D. (2015). The ferroptosis inducer erastin enhances sensitivity of acute myeloid leukemia cells to chemotherapeutic agents. Molecular & cellular oncology *2*, e1054549.

Zhang, H., Zhou, L., Shi, W., Song, N., Yu, K., and Gu, Y. (2012). A mechanism underlying the effects of polyunsaturated fatty acids on breast cancer. International journal of molecular medicine *30*, 487-494.

Zhang, S., Zeng, N., Alowayed, N., Singh, Y., Cheng, A., Lang, F., and Salker, M.S. (2017). Downregulation of endometrial mesenchymal marker SUSD2 causes cell senescence and cell death in endometrial carcinoma cells. PLoS One *12*, e0183681.

Zhang, Y.-H., Wang, D.-W., Xu, S.-F., Zhang, S., Fan, Y.-G., Yang, Y.-Y., Guo, S.-Q., Wang, S., Guo, T., and Wang, Z.-Y. (2018). α-Lipoic acid improves abnormal behavior by mitigation of oxidative stress, inflammation, ferroptosis, and tauopathy in P301S Tau transgenic mice. Redox biology *14*, 535-548.

Zhou, Y., Nwokonko, R.M., Cai, X., Loktionova, N.A., Abdulqadir, R., Xin, P., Niemeyer, B.A., Wang, Y., Trebak, M., and Gill, D.L. (2018). Cross-linking of Orai1 channels by STIM proteins. Proceedings of the National Academy of Sciences *115*, E3398-E3407.

Zille, M., Karuppagounder, S.S., Chen, Y., Gough, P.J., Bertin, J., Finger, J., Milner, T.A., Jonas, E.A., and Ratan, R.R. (2017). Neuronal death after hemorrhagic stroke in vitro and in vivo shares features of ferroptosis and necroptosis. Stroke *48*, 1033-1043.

Zündorf, G., and Reiser, G. (2011). Calcium dysregulation and homeostasis of neural calcium in the molecular mechanisms of neurodegenerative diseases provide multiple targets for neuroprotection. Antioxidants & redox signaling *14*, 1275-1288.

Zweifach, A., and Lewis, R.S. (1993). Mitogen-regulated Ca2+ current of T lymphocytes is activated by depletion of intracellular Ca2+ stores. Proceedings of the National Academy of Sciences *90*, 6295-6299.

9. Appendix

Table 9 Reagents and sources used in this study.

Compounds	Source	Identifier
Imidazole ketone erastin (IKE)	Stockwell lab	N/A
(1S,3R)-RSL3	Stockwell lab	N/A
TNF Recombinant Mouse Protein (TNFα)	Thermo Fisher Scientific	PMC3014
BODIPY 581/591 C11	Thermo Fisher Scientific	D3861
DMEM, high glucose, pyruvate, no glutamine	Thermo Fisher Scientific	21969035
Geneticin Selective Antibiotic (G418 Sulfate)	Thermo Fisher Scientific	10131027
L-Glutamine (200mM)	Thermo Fisher Scientific	25030024
Penicillin-Streptomycin (10,000 U/mL)	Thermo Fisher Scientific	15140122
Power SYBR Green PCR Master Mix	Thermo Fisher Scientific	4367659
RPMI 1640 Medium	Thermo Fisher Scientific	21875034
Trypsin-EDTA	Thermo Fisher Scientific	25300054
Lipofectamine RNAiMAX Transfection Reagent	Thermo Fisher Scientific	13778030
Lipofectamine 2000 Transfection Reagent	Thermo Fisher Scientific	11668027
Skim Milk Powder	Sigma	70166-500G
X-tremeGENE HP DNA Transfection Reagent	Sigma	6366244001
Accutase solution	Sigma	A6964
(Z)-4-Hydroxytamoxifen	Sigma	H7904-5mg
α-Tocopherol (αToc)	Sigma	T3251
Puromycin dihydrochloride	Sigma	P9620
Blasticidine S hydrochloride	Sigma	15205-25MG
Hygromycin B solution from Streptomyces hygroscopicus	Sigma	H0654-1G
Lipofectamine RNAiMAX Transfection Reagent	LifeTechnologies	13778100
Zeocin Selection Reagent	LifeTechnologies	R25001

AquaBluer	MultiTarget Pharmaceuticals	6015
Standardized Fetal Bovine Serum (FBS)	Biochrom	s0615
RNase Inhibitor, Human Placenta	NEB	M0307S
Z-VAD-FMK (zVAD)	BioCat	T6013-5mg
Eicosapentaenoic Acid	Biomol	Cay-90110.1
Docosahexaenoic Acid	Biomol	Cay90310-50
Docosapentaenoic Acid	Biomol	Cay90165-1
C18(PLASM)-18:1 PC	Sigma	852467C-5MG
C18(PLASM)-22:6 PE	Sigma	852806C-5MG
C18 (Plasm) -20: 4 PE	Sigma	852804C-5MG
Calcium Ionophore A23187	Sigma	C7522
BRADYKININ ACETATE	Sigma	B3259-1MG
Thapsigargin	Santa Cruz	SC-24017
U-73122	Fisher Scientific	15465189
m-3M3FBS	Biomol	Cay16867-5
Phorbol 12,13-dibutyrate (PdBu)	R&D	4153/1
Gö6983	Biomol	Cay13311-1
(S)-Bromoenol lactone	Biomol	Cay10006801
Methyl Arachidonyl Fluorophosphonate	Biomol	Cay70660-1
FIPI	Biomol	Cay13563-1
Cycloheximide	Merck	239764
Hydrogen Peroxide	Sigma	31642
6-Thioguanine	Sigma	A4882
Vinblastine	Sigma	V1377
Cisplatin	Sigma	P4394
Cytochalasin	Sigma	C6762
Etoposide	J&K	320523
Cyclophosphamide	J&K	419656
Cochicine	Serva	77120

Table 10 Reagents that modulate ferroptosis sensitivity (Li et al., 2020).

	Reagent	Target/function	Impact on ferroptosis
Inducers/ Sensitizers	Erastin, PE, IKE, other erastin analogs	System X_c^-	Prevent cystine import, cause GSH depletion
	Sulfasalazine, Glutamate, Sorafenib		
	(1S,3R)-RSL3	GPX4	Covalent inhibitor of GPX4 that causes accumulation of lipid hydroperoxides
	ML162, DPI compounds 7,10, 12, 13, 17, 18, 19		
	BSO, DPI2, cisplatin	GSH	Deplete GSH
	FIN56	SQS and GPX4	Depletes CoQ10 via SQS-mevalonate pathway, and decreases GPX4 abundance
	FINO2	Trigger lipid peroxidation	Induces loss of GPX4 activity and lipid peroxidation
	Statins (e.g., cerivastatin, simvastatin)	HMGCR	Block CoQ10 biosynthesis via mevalonate pathway
	Cysteinase	Cysteine	Depletes cysteine, resulting in GSH depletion
	Silica-based nanoparticles	GSH, iron	Deliver iron into cells and reduce GSH abundance
	Ferric ammonium citrate	Iron	Increased iron abundance
	Trigonelline, brusatol	NRF2	Blocks NRF2
Inhibitors	alpha-tocopherol, Trolox, tocotrienols	Block lipid peroxidation	may inhibit lipoxygenases
	Deuterated PUFAs		Blocks initation and propagation of lipid peroxidation
	Butylated hydroxytoluene, butylated hydroxyanisole		

	Ferrostatins, liproxstatins		
	CoQ10, Idebenone		
	XJB-5-131		Nitroxide antioxidant
	Deferoxamine, cyclipirox, deferiprone	Iron	Depletes iron and prevents iron-dependent lipid peroxidation
	Glutamine deprivation, Glutaminolysis inhibitor	Glutaminolysis	Unknown
	CDC, Baicalein, PD-146176, AA-861, Zileuton	Lipoxygenases	Block lipoxygenase-induced lipid peroxidation
	Cycloheximide	Protein synthesis	Suppresses ferroptosis induced by system $\mathbf{X_c^-}$ inhibitors
	beta-mercaptoethanol	Reducing agent	
	Dopamine	Neurotransmitter	Blocks GPX4 degradation
	Selenium	Selenoproteins	Increases selenoproteins
	Vildagliptin, alogliptin and linagliptin	DPP4	Blocks DPP4-mediated lipid peroxidation

10. Acknowledgements

First of all, I would like to thank my supervisor Dr. Joel Schick for his excellent guidance and support within the last two and a half years. He has been optimistic and patient with my work, and his encouragement, advices and constructive criticism helped me all the time to solve the confusions and break the difficulties. Joel has been passionate about science, his broad knowledge, scientific enthusiasm and stringency have deeply influenced me and set an example for my future work.

I would like to especially thank my doctor father Prof. Dr. Klaus Förstemann and Dr. Michelle Vincendeau for their comments and advices to improve my projects during HELENA thesis committee meetings. I am also indebted to the members of the examination committee for the time and effort they offered in reviewing my thesis: PD. Dr. Dietmar Martin, Prof. Dr. Konstantin Karaghiosoff, Prof. Dr. Lucas Jae, Prof. Dr. Julian Stingele and Prof. Dr. Olivia Merkel.

I am very much thankful to all collaborators of two projects during my PhD study. I would like to give my sincere thanks to Dr. Constanze Müller from the Research Unit Analytical BioGeoChemistry, Helmholtz Center Munich for her brilliant ideas and overall insights of the lipidomics analysis. I also want to thank PD. Dr. Stefan Momma from Frankfurt University for his support in the biomarker project.

I would like to express my gratitude to the most awesome colleagues of the Schick lab and other groups in the Institute for Molecular Toxicology and Pharmacology for their precious help and their companionship. Special thanks to Susanne Pfeiffer for her help and support in work and life.

Finally, I am deeply grateful to my family and friends for their love and encouragement. I want to especially thank Zhe for his understanding, encouragement and support.